E 594

OBSERVATION OF THE INVERSE MUON DECAY IN A DICHROMATIC NEUTRINO BEAM

by

Richard Alan Magahiz

B. A., Northwestern University
(1980)

SUBMITTED IN PARTIAL FULFILLMENT
OF THE REQUIREMENTS FOR THE
DEGREE OF

DOCTOR OF PHILOSOPHY

at the

MASSACHUSETTS INSTITUTE OF TECHNOLOGY

May 1985

Signature of Author . . . . . .
Department of Physics, May 1985

Certified by . . . . . .
Thesis Supervisor

Accepted by . . . . . .
Chairman, Department Committee on Theses

OBSERVATION OF THE INVERSE MUON DECAY IN A DICHROMATIC NEUTRINO BEAM

by

Richard Alan Magahiz

Submitted to the Department of Physics
on May 1985, in partial fulfillment of the requirements
for the degree of Doctor of Philosophy.

ABSTRACT

We have performed an experiment at Fermi National Accelerator Laboratory to search for the inverse muon decay reaction $\nu_\mu + e^- \rightarrow \mu^- + \nu_e$ in a dichromatic neutrino beam. Events were taken at secondary particle momenta and charges of +165, +200, +250, and −165 GeV/c corresponding to a mean π-band neutrino energy of approximately 50 GeV. A signal is found using two independent methods to be consistent with the standard V−A model of charged current interactions and with previous searches for this reaction in wide band exposures.

Thesis Supervisor: Henry W. Kendall

Title: Professor of Physics

To Pamela,
whose prayers and love were my constant nourishment

TABLE OF CONTENTS

Page

TABLE OF CONTENTS

TABLE OF CONTENTS

LIST OF FIGURES

LIST OF FIGURES

LIST OF TABLES

Chapter I. INTRODUCTION AND OVERVIEW.

The history of the attempts to understand the weak interaction is a long one, and has engaged quite a few of the greatest physicists of this century. The properties of the weak interaction are peculiar to it alone among the four fundamental interactions known in nature; such phenomena as parity and CP violation are powerful limiting factors on the form a truly unified theory of the physical world is allowed to take. In recent years, great advances toward understanding the basic interactions have been made with the advent of unified and grand unified gauge theories, and it is the task of experimental and theoretical physicists alike to test these theories against observations.

In the particular case of neutrino interactions, it has been clear since 1933 that spin degrees of freedom were important, when Pauli postulated an unseen spin-$\frac{1}{2}$ particle to ensure energy and angular momentum conservation in nuclear beta decay.[1] The next year, Fermi developed a theory of beta decay based on a point-like interaction of four spin-$\frac{1}{2}$ particles.[2] This was soon generalized to encompass all weak interactions. In 1956, Yang and Lee observed that there was no compelling theoretical reason for parity to be conserved in the weak interactions,[3] a conjecture that was subsequently borne out by the experiments of Wu and others in 1957. To the present time, the data have been consistent with a purely left-handed interaction among leptons that is mediated by massive gauge bosons.

Theories that seek to explain the strong, the weak, and the electro-

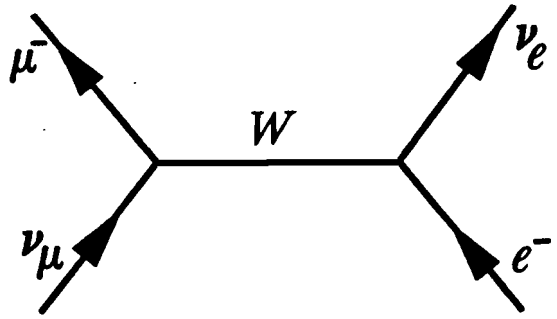

Figure 1–1. Feynman diagram, inverse muon decay.

magnetic interactions as manifestations of a grand unified gauge symmetry explain this parity-violating behavior by providing the left-handed isodoublet representation

$$\binom{u}{d}, \binom{c}{s}, \binom{t}{b}, \ldots \binom{\nu_e}{e^-}, \binom{\nu_\mu}{\mu^-}, \binom{\nu_\tau}{\tau^-}, \ldots$$

and right-handed isosinglet representation $e_R, \mu_R, \tau_R, \ldots$. of the unbroken symmetry group $SU(2)_L$. Some theories seek to achieve more symmetry at high energies by including the unbroken group $SU(2)_R$ and by introducing a new set of gauge bosons for this group, others by adding additional spin-$\frac{1}{2}$ particle representations of $SU(2)_L$ such as the right-handed isodoublet. These symmetries can lead to observable modifications of the phenomenology of weak interactions at attainable energies. The goal of this thesis was to investigate whether one can observe the effects of such departures from the standard model for weak interactions in the inverse muon decay reaction $\nu_\mu + e^- \rightarrow \mu^- + \nu_e$. (Figure 1–1).

The advantages to looking for such discrepancies between the standard left-handed theory and observations in this reaction are two. First, up to the highest energies that modern accelerators have made available to experimenters, all of the particles involved in this reaction are point-like; one

need not worry about corrections that come from the less well understood theory of strong interactions (to an excellent approximation). Second, experimental observation of the reaction is contaminated by only one significant background, namely, the quasielastic scattering of neutrinos off of nucleons $\nu_\mu + N \rightarrow \mu^- + N'$. (Figure 1–2). This can be distinguished from the signal by comparing the data derived from a neutrino exposure, which contains both signal and background, with those derived from an antineutrino exposure, which lacks the signal in the case of pure V−A. Also, among the neutrino events, the presence of hadrons recoiling at the vertex disqualifies an event from being an inverse muon decay. The main disadvantage to using the inverse muon decay reaction is the same one that most neutrino experiments share—it is difficult to amass a large body of data on account of the low cross-section.

We have performed a high-energy experiment in a narrow-band neutrino beam at Fermilab with a massive, fine-grained, calorimetric detector. In this thesis, we shall try to extract as much information as possible about the chiral structure of the weak charged current using the data we have gathered on the inverse muon decay reaction. To motivate this study, the essential theoretical underpinnings will be surveyed in Chapter II. The present state of knowledge on the chiral structure of the weak interaction will be presented in Chapter III, including results obtained by previous searches for inverse muon decay in wide-band neutrino beams. A description of the E594 experiment at Fermilab will follow in Chapter IV, starting with a presentation of the properties of the detector. This chapter will also contains a discussion of the way the raw data from the experiment were analyzed by means of a computer to give us the fundamental measurable quantities needed. In Chapter V

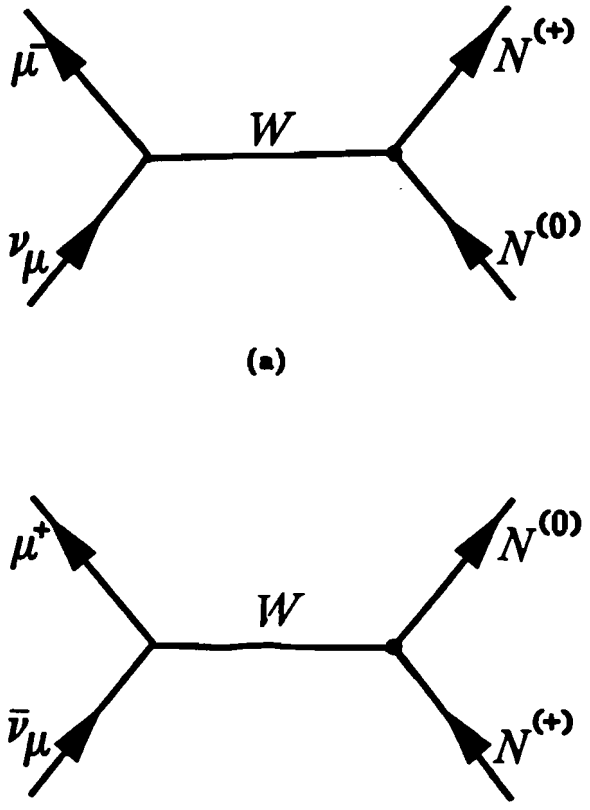

Figure 1–2. Feynman diagrams, (a) Quasielastic neutrino-nucleon scattering, (b) Quasielastic antineutrino-nucleon scattering.

the analysis of the data will be treated in detail and the two tests of the standard V−A theory will be presented, along with their results. Finally, the significance of these results will be discussed in Chapter VI, with a brief apologia of the experimental procedure.

CHAPTER II. THEORY

2A. The weak interaction.

The original formulation of the weak interaction was constructed in analogy with that of quantum electrodynamics. The Hamiltonian for the nuclear beta decay process lacked the propagator factor of $1/q^2$, however, which implied that the four fermions which participated in a reaction interacted at a single point in space-time. In accordance with Lorentz invariance, the most general transition matrix term could contain bilinear combinations $(\bar{\psi}_1 O_i \psi_2)(\bar{\psi}_3 O_i (C_i + C_i' \gamma^5)\psi_4)$ where O_i is one of the five operators

O_i	i
$\mathbf{1}$,	(Scalar)
$\gamma^5 = i\gamma^0\gamma^1\gamma^2\gamma^3$,	(Pseudoscalar)
γ^μ,	(Vector)
$\gamma^5\gamma^\mu$,	(Axial vector)
$\sigma^{\mu\nu} = \frac{i}{2}[\gamma^\mu, \gamma^\nu]$,	(Tensor)

ψ is the four component spinor representation of the fermion, and the γ matrices are 4×4 complex matrices from the Dirac theory. If time reversal invariance is not assumed, each of the 10 coefficients C_i, C_i' may be complex, giving a total of 19 real undetermined constants (allowing for an overall phase).[1]

In order to explain the nuclear beta decay reactions in which the nucleus undergoes a spin-flip, the so-called Gamow-Teller transitions, purely vector

coupling is not sufficient in the weak matrix elements. Experiments that measured the polarization of the outgoing leptons[2,3] showed that the scalar and axial vector terms would produce the wrong helicities if they predominated. The pseudoscalar term would produce a very slight correction to the matrix element and was neglected. In the end, a matrix element composed of only vector and axial vector (V and A) terms was favored. Experiments[4] showed that leptons were predominately left-handed (negative helicity) and antileptons right-handed (positive helicity) and that the weak interactions tended to violate parity maximally. These dictated a predominately "V−A" form for the interaction:

$$\bar{\psi}\gamma_\mu \frac{(1-\gamma_5)}{2}\psi$$

in which the matrix operator $(1-\gamma_5)/2$ is the left-handed projection operator. This form was applied to other weak interactions as well; one early success was the prediction of branching ratios in the decay of pseudoscalar mesons. This test of the V−A interaction and the others which have been applied over the years will be discussed in Chapter III.

The theory was made renormalizable when, in the early 1970's, Glashow, Weinberg, 't Hooft and many others elucidated the non-Abelian gauge structure of the electromagnetic and weak interactions combined. In this theory, the V−A structure appears in the weak isospin group $SU(2)_L$, where the "L" stands for "left-handed". The weak interactions are mediated by spin-1 gauge particles, the $W^{\pm}$ and Z^0 bosons, which acquire a mass of about 100 GeV/c^2 by the Higgs mechanism. In the present experiment, the effects of the propagator masses are entirely negligible on account of the relatively low energy in the center of momentum frame ($E^* \approx 0.1$ GeV). It is expected, however, that the theoretical analysis would still be valid once the propagator masses

are taken into account.

2B. Inverse muon decay.

The inverse muon decay reaction is a particularly convenient one to calculate because of the pointlike structure of all the particles involved. It is a cross channel of direct muon decay, which was characterized in the 1950's in terms of the Michel parameters. It has the experimental advantage that three out of the four leptons have known four-momenta. Furthermore, the corresponding reaction for antineutrinos $\bar{\nu}_\mu + e^- \rightarrow \mu^+ + \nu_e$ would be strictly forbidden if lepton numbers are conserved in an additive fashion.[5] This supplied a "clean" sample of background quasielastic scattering events which could be subtracted from the neutrino data (in the differential cross section tests, sections 5B and 5C) or which could be subjected to the same analysis as the neutrino data to help distinguish the effects of actual signal from artifacts of detector acceptance, background, and resolution. A detailed derivation of the differential cross-section is too long to include here; the interested reader is referred to Appendix A. The result of this derivation, allowing arbitrary V and A couplings only, is:

$$\frac{d\sigma}{dy} = \frac{G_F^2}{4\pi}(s - m_\mu^2)\left[(1+P)(1-\lambda)y\frac{m_\mu^2 + sy}{s - m_\mu^2} + (1-P)(1+\lambda)\right] \qquad (2.1)$$

where P is the polarization of the incident neutrino beam, λ gives the handedness of the coupling, y is the Lorentz invariant inelasticity $(E_\nu - E_\mu)/E_\nu$, and s is the square of the energy in the center of momentum frame. In the standard picture of left-handed two-component neutrinos and V−A coupling, the parameters P and λ take the values -1 and 1 respectively and there is no y dependence in the cross section. This combination of parameters gives the maximum value for the cross section integrated over y; if we set $\lambda = -1$,

$P = 1$, (V+A with right-handed neutrinos) we obtain an integrated cross section only about one-third as large. This allows an experiment that cannot measure y directly (in a broad-band beam) to place limits on these parameters.

An experiment that measures the integrated cross section sets simultaneous limits on P and λ with one equation of constraint. Alternatively, one may attempt to determine the handedness of the weak interaction (λ) absolutely, by estimating the amount of right-handed neutrino flux composing the incident beam ($P \equiv \frac{N(\nu_R) - N(\nu_L)}{N(\nu_R) + N(\nu_L)}$). If neutrinos have masses they will have finite velocities $\beta < 1$ and helicities equal to $-\beta$, and will appear in both polarization states. These masses may be inserted as extensions to the Glashow-Weinberg-Salam theory by adding terms to the Lagrangian of the form

$$\bar{\ell}_L m_U \ell_R \tag{2.2}$$

where m_U is a unitary mass mixing matrix and ℓ, ℓ' are lepton spinors. If $\ell = \ell'$ then this is a Majorana mass term, otherwise it is a Dirac mass term. A possible theoretical motivation for including this type of mass term arises in the context of certain grand unified theories such as SO(10) which possess left-right symmetry.[6] The helicity of the final state nuclei in spin-0 nuclear beta decay Fermi transitions has been measured[7] (and hence, by angular momentum conservation, the helicity of the neutrinos) and the data are consistent with purely left-handed two-component neutrinos.

In broad-band experiments, it is necessary also to average over s in integrating the cross section, since this quantity cannot be measured directly. One resorts to modelling the beam energy distribution on computers. In contrast, experiments in a narrow-band neutrino beam can measure the in-

coming neutrino energy E_ν and apply

$$s = m_e^2 + 2m_e E_\nu \tag{2.3}$$

to reduce the uncertainties introduced in such an approach. In principle, the parameters P and λ can be separated because one can measure y and fit to the form of the differential cross section, achieving one more equation of constraint. In practice, problems with low statistics and with experimental resolution limit the applicability of this method severely.

One of the unattained goals in the verification of the Glashow-Weinberg-Salam model is to find the Higgs particles. If charged Higgs particles can couple to leptons, such as in certain extensions of the standard model,[8] scalar or pseudoscalar currents may be observed in inverse muon decay. The integrated cross section for various combinations of arbitrary S, P, V, A, and T couplings has been calculated for this reaction[9] and is given in detail in Appendix B. To obtain constraints on the parameters, data from the inverse muon decay as measured by the CHARM collaboration were combined with data from experiments measuring direct muon decay, pseudoscalar meson decay, polarization of positive muons produced in inclusive antineutrino reactions, and electron polarization in Gamow-Teller transitions. A total of nine different models were investigated with different assumptions concerning universality and which couplings to include. Each of these models used the integrated cross section of the inverse muon decay to constrain the coupling constants, although not all of the other data were used in each case. The authors of this study found that quite substantial departures from pure V−A were consistent with experiment (up to 30%) owing primarily to the poor agreement of the electron polarization data from direct muon decay experiments with theory.

2C. Quasielastic scattering of neutrinos.

The only significant experimental background to the inverse muon decay reaction is quasielastic neutrino scattering $\nu_\mu + N^{(0)} \rightarrow \mu^- + N^{(+)}$ where $N^{(0)}$ is a neutron (or, possibly, a heavier neutral baryon) and $N^{(+)}$ is a proton or some other positively charged baryon, such as the Δ^+. (See figure 1–2a) There is also an analogous reaction of antineutrinos: $\bar{\nu}_\mu + N^{(+)} \rightarrow \mu^+ + N^{(0)}$ (figure 1–2b). These reactions have been studied in great detail in the past two decades of neutrino experiments as a way to probe the form factors of the nucleon.[10,11] Inverse muon decay can be distinguished from quasielastic scattering in four ways. It is characterized by a muon produced at a small angle to the neutrino beam, without extra tracks leading away from the vertex. It is subject to a threshold for the incoming neutrino energy of 10.9 GeV. Its Q^2 distribution is very sharply peaked, covering only values less than 0.2 GeV^2, as compared with the broad quasielastic Q^2 distribution out to 1.0 GeV^2 and higher. (This is due to the low reaction mass of the electron as compared to the nucleon.) The y distribution of inverse muon decays is broad, because of the large amount of unseen energy in the final state, whereas the same distribution for quasielastics is peaked at zero—indeed, this may be taken to be the definition of a quasielastic scattering event.

To simplify the formulation of the dynamics in quasielastic scattering, time-reversal invariance, conserved vector current, lack of an induced pseudoscalar term, and charge symmetry are usually assumed. This assumes that no so-called "second-class currents" are involved. The results are expressed in terms of dipole form factors for the axial and vector currents:

$$F_{V,A}(Q^2) = \frac{F(0)}{(1 + Q^2/M_{V,A}^2)^2} \tag{2.4}$$

where M_A, M_V are mass scales. By conservation of the vector current, M_V is set equal to 0.84 GeV to agree with electron scattering data. The most recent weighted average value of M_A is 1.03±0.04 GeV.[11] This parameter determines the shape of the Q^2 distribution.

In experiments which use heavy nuclear targets, it is necessary to take into account the nuclear binding effects in the Q^2 distribution. These include the Pauli exclusion principle and nuclear shell effects,[12] which are fairly substantial at low Q^2. The different models can differ by as much as 20% in the region of interest, depending on the assumptions made. In the present experiment, a treatment that simply treated the nucleon as a Fermi gas for neutrons and for protons has been used. A plot of the ratio of correction factors for neutrinos to that for antineutrinos as a function of Q^2 is given in figure 2–1. This has been averaged over the various nuclei in the E594 calorimeter. For a nucleus of N neutrons and Z protons, the cross section per nucleon was multiplied by a nuclear correction factor $1 - D/N$ where

$$D = \begin{cases} Z & \text{for } 2x < u - v \\ \frac{(N+Z)}{2}\left[1 - \frac{3x}{4}(u^2+v^2) + \frac{1}{2}x^3 \right. & \\ \qquad \left. - \frac{3}{32x}(u^2-v^2)^2\right] & \text{for } u - v < 2x < u + v \\ 0 & \text{for } 2x > u + v \end{cases} \tag{2.5}$$

in which $x = |\vec{q}|/(2k_f)$ for a Fermi momentum k_f. For neutrino-induced quasielastic scattering events, $u = (2N/A)^{\frac{1}{3}}$ and $v = (2Z/A)^{\frac{1}{3}}$, while for antineutrino-induced quasielastics $u = (2Z/A)^{\frac{1}{3}}$ and $v = (2N/A)^{\frac{1}{3}}$, where $A = N + Z$. The three-momentum transfer to the nucleon (mass m_p) was related to the four-momentum transfer squared by[13]

$$|\vec{q}| = \sqrt{Q^2}\sqrt{1 + \frac{Q^2}{2m_p^2}} \tag{2.6}$$

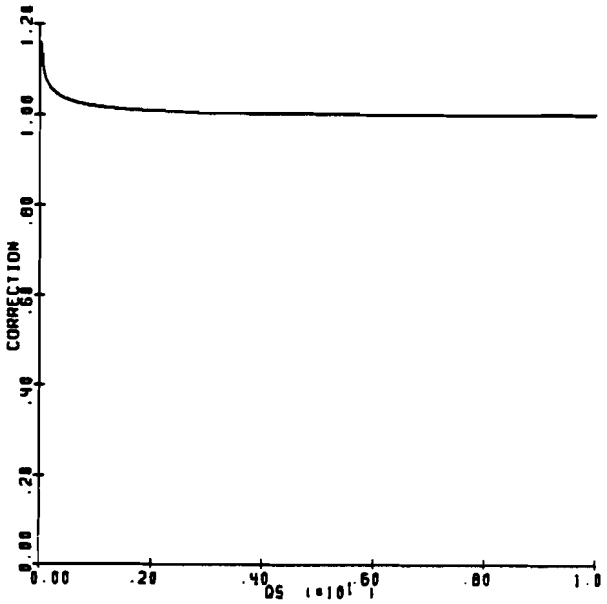

Figure 2–1. Ratio of nuclear correction factors (neutrinos over antineutrinos) vs. Q^2 for quasielastic scattering.

In detectors with limited spatial resolution about the vertex there is also the difficulty that processes such as single-pion production:

$$\nu_\mu + n \rightarrow \mu^- + n + \pi^+$$
$$\nu_\mu + n \rightarrow \mu^- + p + \pi^0$$
$$\nu_\mu + p \rightarrow \mu^- + p + \pi^+$$

may be misidentified as quasielastic events containing only a proton in the final hadronic state. There is a large contribution to these processes through the $I = 3/2$ (Δ) resonant channel and through a non-resonant $I = 1/2$ final state,[14,15] mainly at higher Q^2. In the present experiment, one relies on the ability to subtract such a contamination from the signal in the integrated cross section test (section 5B) by using the antineutrino data. These have the analogous reactions

$$\bar{\nu}_\mu + p \rightarrow \mu^+ + n + \pi^0$$
$$\bar{\nu}_\mu + p \rightarrow \mu^+ + p + \pi^-$$

$$\bar{\nu}_\mu + n \rightarrow \mu^+ + n + \pi^-$$

which may lead to one or more tracks near the vertex. To get an unbiased sample of quasielastic scattering events in the antineutrino data in this experiment, the restriction on finding tracks leading from the vertex (which see, sections 4C.5 and 5A.2e) was not imposed.

CHAPTER III.
EXPERIMENTAL LIMITS ON PARAMETERS IN THE THEORY OF WEAK INTERACTIONS

In this chapter, we will present a summary of the results to date on the couplings in the weak interaction. The first section will be a description of the Gargamelle and CHARM collaboration experiments to observe inverse muon decay in dichromatic beams. The second section will be a brief description of the experimental constraints on non-V−A couplings. The third section will summarize the limits placed on non-V−A couplings in the weak interaction.

3A. Studies of the inverse muon decay in broad band neutrino beams.

Both high enough neutrino energy to overcome the threshold and high enough flux to overcome the low cross section are required to produce observable numbers of the inverse muon decay process. Only relatively recently have neutrino beams been available to study this reaction. Two independent experiments have seen this reaction in the broad band neutrino beams at the CERN-SPS accelerator. These were the Gargamelle heavy liquid bubble chamber experiment[1] which ran from 1977 to 1978, and the CHARM calorimeter experiment[2,3] which ran from 1979 to 1981. They ran in a horn-focussed neutrino beam produced by 400 GeV incident protons. The maximum flux occurred at a neutrino energy of around 15–20 GeV, falling off by

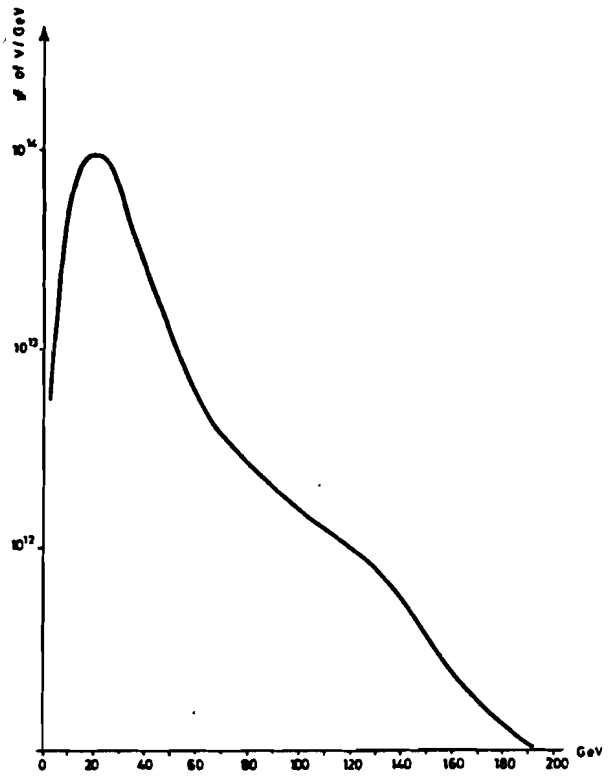

Figure 3–1. CERN-SPS neutrino flux. (Ref. 1)

one order of magnitude by 50 GeV. (See Figure 3–1). The $\bar{\nu}_e$ contamination of the ν_μ beam was estimated[3] to be 11%. The construction and running conditions of these two experiments will now be described briefly, postponing the discussion of the results until chapter 6.

The Gargamelle experiment (which is depicted in Figure 3–2) used a mixture of propane (C_3H_8) and freon (CF_3Br) as a target with mean density 0.51 g/ml. The visible volume was 7.2 m^3, which contained a fiducial volume of 4.01 m^3 and a fiducial mass of one metric ton. A muon track was detected by means of a pair of multiwire proportional chambers placed upstream and downstream of the chamber (the upstream chamber acted as a veto) and an external muon identifier (EMI) made up of two sets of proportional chambers

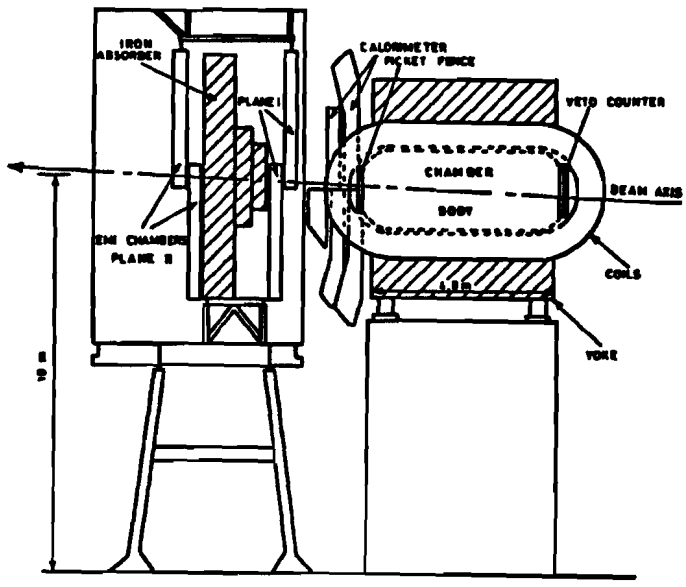

Figure 8–2. Elevation of Gargamelle. (Ref. 1)

separated by iron absorber material. Hit information from the the chambers was taken every 0.5 μsec during the 2 msec spill, and was used to prescreen the data on film. A total of 377000 pictures was taken with the horn was set to focus positive secondaries to favor neutrino production over antineutrino production. The combination of the EMI and the visual scanning efficiencies was 94±3%. The visual scanning searched for recoil proton tracks leading away from a vertex. It identified 84 candidate recoilless events within an angle of 100 mrad from the incident beam direction. The background due to non-interacting single π^- production was estimated to be completely negligible. To estimate some of the quasielastic ν_e background, data taken at the lower energy CERN-PS neutrino beam were used. This had a vanishingly small flux above the threshold for inverse muon decay, so all of the recoilless muons should have come from quasielastics. Nearly all of these had transverse momentum P_T >160 MeV/c, so this cut was applied to the CERN-SPS data, leaving only 26±6 signal events. By an independent method which used

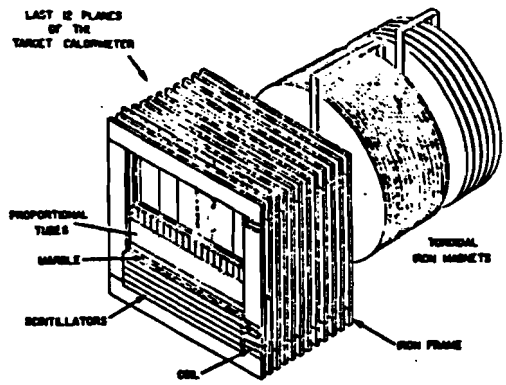

Figure 3–3. View of the CHARM detector.

the distribution of the candidate events in E_ν and θ_μ^2 for inverse muon decay signal and for background, the experimenters arrived at the same number of signal events.

The CHARM detector[4] (see Figure 3–3) used marble slabs for target material. The cross sectional area presented to the beam was 3m×3m. This area was surrounded by a frame of magnetized iron and was instrumented with layers of plastic scintillation counters and of proportional drift tubes. A total of 1560 scintillators and 13000 drift tubes (including the toroid chambers) was used. The main calorimeter was followed by a toroidally magnetized muon spectrometer consisting of an end calorimeter and three end magnets. These were instrumented with drift tubes, which could measure the track coordinates with 1 mm resolution. The event trigger was defined by the coincidence of four scintillator plane hits, a minimum of 50 MeV detected ionization, and a track that traversed the spectrometer. After cutting on muon polarity, and on lack of visible energy about the event vertex, there was a total of

16843 neutrino events. Of these, 937 had $Q^2 < 0.02$ GeV and $p_\mu > 10$ GeV. The background from quasielastic scattering was estimated from the shape of the antineutrino data plotted in Q^2; it accounted for 551±36 of the events, leaving an excess of 386±36. This was corrected for detector acceptance and for selection efficiencies to give a total corrected number of inverse muon decays of 594±56(statistical)±22(systematic) events. Under the conditions of the experiment, the V−A theory with left-handed neutrinos would have predicted about 606 events.

3B. Experimental constraints on non-V−A couplings.

Table 3–1 lists the experimental quantities, other than the inverse muon decay cross section, which place constraints on the deviations from V−A in the context of various alternative models of the weak interaction. We will give a brief description of each of the quantities, leaving a fuller description to the references in the literature[5,6,7] from which this section is adapted.

3B.1. Leptonic charged current.

These quantities are measured in four types of experiment. The first type looked at the ratio of pseudoscalar meson (pion and kaon) decay to electrons and to muons, $R_{\pi(K)}$. The best values for R_π and R_K were measured by Di Capua *et al.*[8] and by the CERN-Heidelberg collaboration.[9] These have been normalized by the V−A values $R_\pi^{V-A} = 1.239 \times 10^{-4}$ and $R_K^{V-A} = 2.474 \times 10^{-5}$. The second type measured the longitudinal polarization of the muon, P_μ, from pion decay.[10] The third type looked at $-(c/v)P_{\beta^-}$, the polarization of electrons produced in nuclear beta decay. The most current estimate for this is given by Koks and van Klinken.[11] Finally, the direct muon decay process, $\mu \rightarrow e\nu_\mu\bar{\nu}_e$, has been characterized by nine parameters: spectrum shape (ρ, η), asymmetry (ξ, δ), electron helicity (h), and transverse

Table 3–1

Quantities constraining non-V−A couplings

Quantity	Measured	V−A value	Units	Ref.
R_π/R_π^{V-A}	1.023±0.019	1	–	8
P_μ	0.99±0.16	1	–	10
R_K/R_K^{V-A}	0.978±0.044	1	–	9
$-(c/v)P_{\beta-}$	1.001±0.008	1	–	11
ρ	0.7517±0.0026	0.75	–	13
$P_\mu\xi$	0.975±0.015	1	–	13, 14
δ	0.750±0.004	0.75	–	20
h	1.008±0.054	1	–	15
$\langle\sigma(\nu_e e)\rangle$	7.6±2.2	5.586	10^{-46} cm^2	7
$\sigma(\nu_\mu e)/E_\nu$	1.54±0.67	1.376	10^{-42} cm^2/GeV	7
$\sigma(\nu_\mu e)/E_\nu$	1.46±0.24	1.503	10^{-42} cm^2/GeV	7
$\sigma(\nu_\mu e)/\sigma(\nu_\mu e)$	$1.37^{+0.65}_{-0.44}$	1.092	–	7
A^{FB}	11.8±3.9	7.57	%	7
h_{VV}	0.009±0.040	0.0048	–	7
R^-	0.264±0.008	0.261	–	7
R^+	0.315±0.009	0.325	–	7
R_p	0.47±0.064	0.401	–	7
R_n	0.22±0.031	0.240	–	7
a_1	-9.7 ± 2.6	-6.64	10^{-5}GeV^{-2}	7
a_2	4.9 ± 8.1	-6.23	10^{-5}GeV^{-2}	7
B	-1.40 ± 0.35	-1.37	10^{-4}GeV^{-2}	7
$P_\mu\xi\delta/\rho$	0.9989 ± 0.0023	1	–	19

electron polarization (α, β, α', β'). Of these, ρ, δ, h, and $P_\mu \xi$ are useful in constraining the non-V−A couplings. These quantities have been measured by various experiments, as indicated by table 3–1.

3B.2. Leptonic neutral currents.

By using data from the neutral current weak interactions, one can eliminate certain ambiguities in the parameters of a model.[7] Among the purely leptonic processes, we can use three sets of data to set limits on the couplings. These are the total cross section for $\bar{\nu}_e e$ scattering averaged over the beam spectrum, $\langle\sigma(\bar{\nu}_e e)\rangle$, and the total cross sections for $\bar{\nu}_\mu e$ and $\nu_\mu e$ scattering, $\sigma(\bar{\nu}_e e)$ and $\sigma(\nu_e e)$. We also use h_{VV}, the coefficient of $(1+\cos^2\theta)$ for $e^+e^- \rightarrow \mu^+\mu^-$, as well as the associated parameter of forward-backward asymmetry A^{FB}, but since the published formulae for these quantities do not seem to agree with the fit values our results will differ from those of the previous studies. The experimental input for h_{VV} was measured at PETRA,[16] and the value for A^{FB} at $\sqrt{s} = 33.5$ GeV has been measured by Bartel *et al.*[17]

3B.3. Semileptonic processes.

When we consider the weak interactions of quarks, we need to make certain assumptions about the ways in which the quarks can participate in non-V−A couplings. To suppress flavor changing neutral currents via the GIM mechanism, in the context of a fermion-mirror fermion mixing model, we must assume that the quark-mirror quark mixing angles are negligible.[7] With this assumption, we may set constraints on the model by looking at the ratios of total cross sections:

$$R^{\pm} = \frac{\sigma_{NC}(\nu_\mu \tilde{N}) \pm \sigma_{NC}(\bar{\nu}_\mu \tilde{N})}{\sigma_{CC}(\nu_\mu \tilde{N}) \pm \sigma_{CC}(\bar{\nu}_\mu \tilde{N})} \tag{3.1}$$

for isoscalar targets $\tilde{N}$ and

$$R_N = \frac{\sigma_{NC}(\nu_\mu N)}{\sigma_{CC}(\nu_\mu N)} \tag{3.2}$$

for nucleons $N = p, n$. These were measured by a number of experiments, as quoted in reference 7. The additional constraints provided by the data on charge asymmetry in polarized lepton-hadron scattering (parameters a_1, a_2, and B) disagree by a constant factor between the fit values of reference 7 and the formulae given both there and in other references.[18] We will adopt these formulae and compute the expected values without comparing to the published fit.

3C. Present limits on non-V−A couplings.

We considered possible deviations from the standard V−A couplings in the framework of three possible models. The most general model, which introduced various amounts of S, T, and P couplings in addition to the standard V and A couplings, was discussed by Mursula *et al.*[6] Since we have been unable to reproduce the derivations of the formula for the inverse muon decay cross section (section BC of appendix B) for the present experimental conditions, this model was not analyzed fully here. Instead the two other hypotheses, which admitted only vector and axial-vector couplings in the charged weak interaction, were investigated in some detail. These were the *fermion–mirror fermion mixing model*, inspired by such models as SO($n > 10$) and SU($n > 5$), and the *left-right symmetric model*, which was based on the flavor group $SU(2)_L \times SU(2)_R \times U(1)$.

The fermion–mirror fermion mixing model combined the conventional left-handed doublet $\begin{pmatrix} \nu'_\ell \\ \ell' \end{pmatrix}_L$ and right-handed singlet representations ℓ'_R, $\nu'_{\ell R}$ of the weak isospin group $SU(2)_L$ with corresponding right-handed doublet

and left-handed singlet representations $\begin{pmatrix}\nu'_\ell\\ \ell'\end{pmatrix}_R$, ℓ'_L, $\nu'_{\ell L}$ to make up the leptonic mass eigenstates of fermions and mirror fermions. The gauge particles were unchanged. The predictions of such a theory depended on the relation of the masses of the mirror fermions to those of the conventional fermions. References 5 and 7 considered six distinct cases in analyzing the experimental results (see appendix B for details). The adjustable parameters were the mixing angles for charged leptons θ_ℓ and for neutrinos ϕ_ℓ, which would all be zero for the V−A limit.

The left-right symmetric model[5,12] introduced gauge bosons W_R of the gauge group $SU(2)_R$. These would mix with the conventional left-handed gauge bosons W_L, through spontaneous symmetry breaking, to form mass eigenstates. The adjustable parameters were the mass ratio of the two gauge bosons m_{W_L}/m_{W_R} and the mixing angle ω. In the V−A limit, $m_{W_L}/m_{W_R} = 0$ and $\omega = 0$. Also, as the center of mass energy increased, the effect of the (heavy) W_R bosons would increase and non-V−A behavior would become more apparent.

Table 3–2a gives the results of our fits to the experimental data for several different cases of the fermion–mirror fermion model. The quantities constraining the fits were the leptonic charged current measurements of ρ, δ, $P_\mu\xi$, h, R_π, R_K, P_μ, P_{β^-}, and the integrated cross section for inverse muon decay, S (excluding the result of the present experiment), the neutral current measurements of $\langle\sigma(\nu_e e)\rangle$, $\sigma(\nu_\mu e)$, and $\sigma(\bar{\nu}_\mu e)$, and the semileptonic quantities R_p, R_n, R^+, and R^-. The goodness-of-fit quantity χ^2 was minimized for these quantities simultaneously after having combined the values of h and P_{β^-} and of R_π and R_K by weighted means. The integrated cross section for the inverse muon decay has a different dependence on the mixing

angles for each of the cases (for details on this dependence, see appendix B).

Table 3–2b gives the results of fits to the experimental data for the left-right symmetric model. The quantities ρ, $P_\mu \xi$, h, R_π, R_K, P_μ, P_{β^-}, and the integrated cross section for inverse muon decay, S, (excluding present results) were used in the χ^2 minimization process, with R_π and R_K being combined beforehand. See appendix B for details on how the integrated cross section of inverse muon decay depended on the two parameters of the theory.

In chapter 5, we will return to these two types of models and re-evaluate the couplings with the value for the inverse muon decay cross section that this experiment was able to obtain. It should be noted, for future reference, that of all the experimental inputs we consider, only one, the longitudinal polarization of the electron in muon decay ($P_\mu \xi$), deviated appreciably from the pure V−A value.

Table 3–2a
Results to fits for fermion–mirror fermion models
(value for S from CHARM experiment)
Best fits and 68.3% C.L. values

Model	θ_e	θ_{emax}	ϕ_e	ϕ_{emax}	θ_μ	$\theta_{\mu max}$	ϕ_μ	$\phi_{\mu max}$	$\sin^2\theta_W$	χ^2/d.f.
a_{coh}	1.1	2.0	8.5	16.5	0.0	2.3	8.9	13.6	0.249	9.4/18
a_{inc}	free*	free	6.5	15.9	free	free	7.7	12.2	0.247	9.9/18
b_{coh}	1.1	1.8	16.0	25.0	0.0	3.8	0.0	44.9†	0.240	10.2/16
b_{inc}	free	free	15.9	25.0	free	free	0.0	4.7	0.240	10.6/18
c	5.0	13.3	14.0	18.8	2.5	9.2	13.9	18.2	0.221	8.3/16
d_{coh}	0.0	38.2†	4.4	7.1	0.0	1.6	9.0	13.6	0.249	9.9/16
d_{inc}	free	free	4.3	7.1	free	free	7.9	12.3	0.246	9.9/18

*Unconstrained parameter
†Parabolic error estimate
All values in degrees. Pure V−A gives zero for all mixing angles.

Table 3–2b
Results to fit for the left-right symmetric model
(value for S from CHARM experiment)

Quantity	Fit value	68.3% C.L.
m_{W_L}/m_{W_R}	0.14	0.18
ω	0.0°	1.9°

$\chi^2 = 3.0$ for 5 degrees of freedom.
Pure V−A value is zero for each parameter.

CHAPTER IV. THE E594 EXPERIMENT AT FERMILAB.

In this chapter, we will try to give a description of the parts of the E594 experiment that played major roles in the observation of inverse muon decay. Section 4A is a brief statement of objectives we wished to reach. Section 4B gives a description of the physical configuration of the apparatus, including the electronics and the beam monitors. Section 4C is a description of the computer routines which were used in the analysis of the data, and which played as important a role in this experiment as the hardware itself. Section 4D summarizes the running conditions for this experiment, including a description of the generation of the dichromatic neutrino beam. The final section, 4E, discusses the way in which the response of the detector and of the analysis routines to neutrino-induced events was calibrated.

4A. Considerations in the choice of detector properties.

A successful counter-based neutrino detector must have a number of properties to be able to record and to analyze inverse muon decay events. The first requirement is that the instrumented volume comprise a large mass. This is especially important in a narrow-band neutrino beam which has a lower flux of neutrinos than a wide-band horn focussed beam. The second requirement

is that the spatial resolution of the detector elements be fine enough so that one can distinguish ordinary quasielastic and deep inelastic events from the signal events. These first two requirements necessitate certain tradeoffs in designing the detector. For instance, choosing a very dense material for the target increases the fiducial mass but decreases the ability to discern low-energy tracks. Also, constructing a large detector increases the useable volume but can also increase the size and number of the counters needed. A third requirement is that there be a way to measure the momentum and sign of the produced muon. This calls for a magnetic spectrometer which can be integrated either with the target portion of the detector (as in the CDHS detector at CERN) or can be a separate downstream portion (as in the present experiment). Finally, the information both from the detector itself and from the beam monitors must be recorded in a way that permits later analysis of the event topology.

4B. Construction of the detector.

The E594 detector was composed of two parts, the fine-grained calorimeter and the muon spectrometer. A schematic elevation view of the detector is given in figure 4–1a. In this section, we will describe the two portions of the detector, and then give a summary of the electronic trigger logic and of the data acquisition system.

4B.1. The fine-grained calorimeter.[1]

The calorimetric portion of the E594 detector was of modular construction. A framework of steel box beams supported the entire weight of the calorimeter, some 340 metric tons. It was divided into nine *bays*, which were composed of from two to five identical *modules* each weighing nine metric tons (along with one $12' \times 12' \times 4''$ tank of liquid scintillator oil), each of

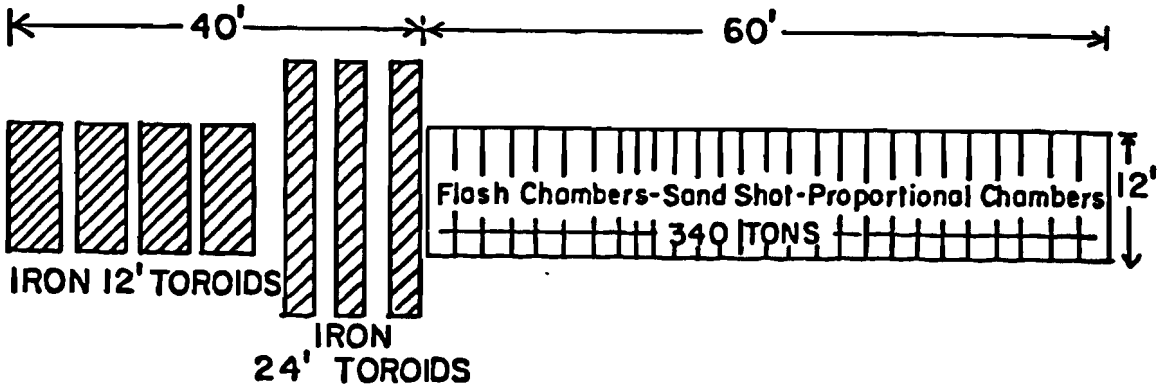

Figure 4–1a. Elevation of the detector.

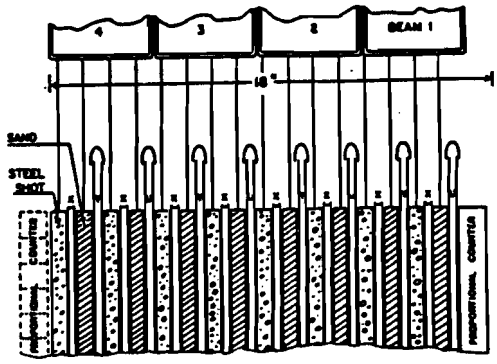

Figure 4–1b. Layout of an individual calorimeter module

Detector properties

Table 4–1

Length of calorimeter	19.6 m
Cross section of calorimeter	12′×12′ (3.7 m×3.7 m)
Total mass	3.4×10^5 kg
Density	1.4 g cm^{-3}
Radiation length (X_0)	12 cm
Absorption length (λ)	83 cm (116 g cm^{-2})
Length in absorption lengths	22 λ
Mean atomic number	21

which was composed of one proportional chamber plus four *beams* of four flash chambers interleaved with four absorber planes. The structure of an

individual module is depicted in figure 4–1b. The detector planes were supported in a way that allowed easy access to the instrumentation; individual planes could be removed for servicing. In all, there were 608 flash chambers, 37 proportional chambers, nine liquid scintillators, and 608 absorber planes. Some of the properties of the overall detector are given in table 4–1. The individual elements that make up the calorimeter are described in detail in the sections which follow.

4B.1a. The flash chambers.

Flash chambers are devices which combine fairly good spatial resolution with low cost and ease of fabrication. They are similar to spark chambers in configuration, but are triggered externally and are segmented by insulating walls within which the plasma discharge propagates. Each flash chamber was constructed of three panels of extruded polypropylene that had cells of rectangular cross section. The panels were taped edge to edge parallel to the cells and aluminum foil was laminated to the two faces of the plane to provide high voltage and ground electrodes 12′×14′in size. A plane had a capacitance of 30 nf. There were approximately 4×10^5 cells in the entire detector, 635 cells per flash chamber, with each cell 5 mm thick, 5.8 mm wide, and 3.6 m long. The walls of the cells were about 0.5 mm in thickness. The flash chambers were supplied continuously with a mixture of 96% Ne, 4% He, 0.17% Ar, 0.10% H_2O, and 0.04% O_2 and N_2 by means of a manifold along one edge; the gas was collected at the opposite edge, purified in molecular sieves, and recirculated at the rate of approximately one volume change per hour. This mixture of gases had been chosen after much research into combining the minimimum refire probability of the chambers with the maximum efficiency.

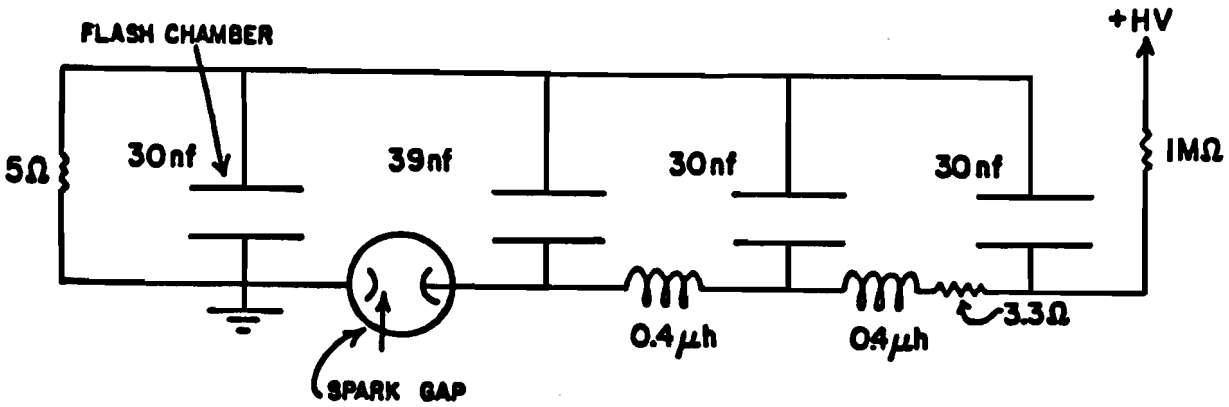

Figure 4–2. HV pulse forming network.

When the trigger logic detected an event, a high voltage pulse was sent to the electrodes of each flash chamber by a **pulse forming network** (PFN) approximately 700 nsec after the event (see figure 4–2). This 4.5 kV peak voltage pulse had a 60 nsec rise time and a 500 nsec duration, and was monitored to insure uniformity in timing, pulse height, and pulse shape. As we shall see in the description of the proportional wire chambers, the RF noise generated by this surge of current was a formidable constraint on the design of readout systems.

The strong electric field between the electrodes caused rapid avalanche multiplication of any ionization left by charged particles that had traversed the gas in a flash chamber cell. This resulted in a plasma which expanded towards the ends of the chamber at a speed of about 0.1 ft $nsec^{-1}$. At one end of a chamber, the plasma discharge was capacitively coupled to a 3 mm wide copper readout strip which connected to ground. (See figure 4–3). The 0.5 A current spike induced on this copper strip in turn induced an acoustic pulse on a 0.005″ ×0.012″ magnetostrictive wire contained in a *wand*

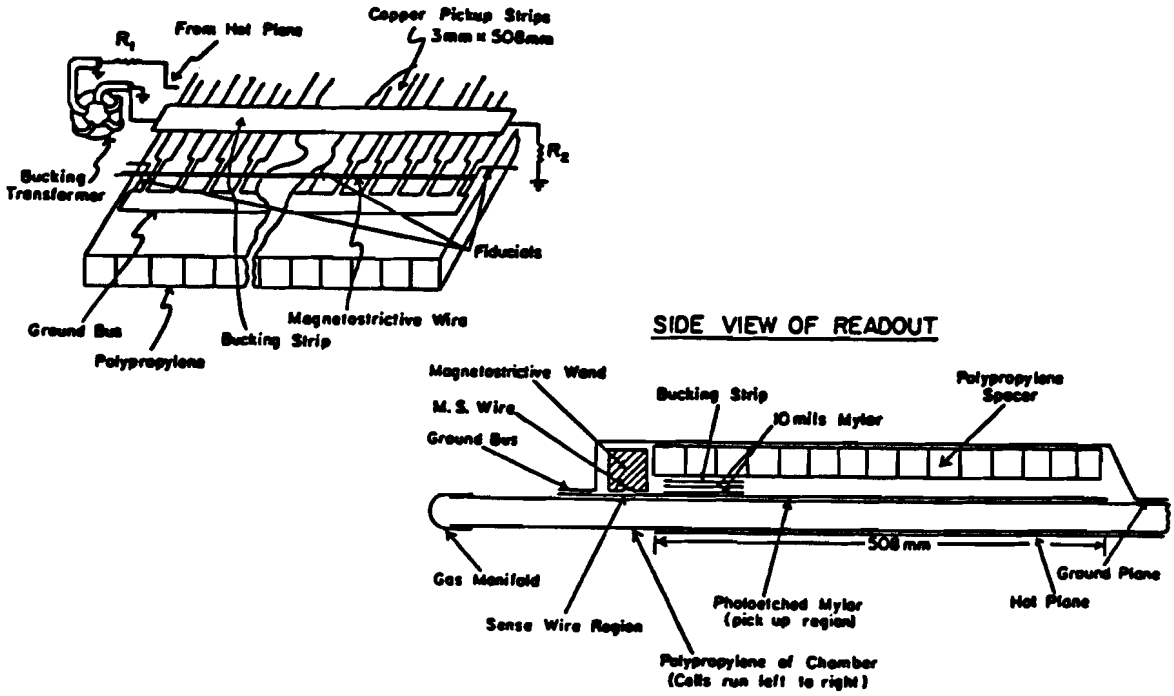

Figure 4–8. Flash chamber readout.

assembly which ran across the flash chamber cells and which was maintained at a constant magnetization. The acoustic pulse then propagated with low dispersion toward the two ends of the wire at about 5000 m sec^{-1} or 1 μsec per cell. Along with the pulses from the chambers, three fiducial markers at known positions along the wand were provided. The pulses were detected and amplified and the information from the timing of the pulse trains from each end yielded a unique pattern of hit cells on the chamber. The clock period used for timing the pulses corresponded to just under half a cell width and had been chosen in order to reduce problems caused by bad synchronization and by variations in cell width.

The information given by a flash chamber was simply whether one or more charged particles had traversed a given cell somewhere along its length, for the nature of the plasma process eliminated any pulse height or particle counting capability. To measure track coordinates in two dimensions, three sets of chambers were used with cells oriented horizontally (the X chambers

illustrated in figure 4–1b) and at approximately ±10° from the vertical (the U and Y chambers) to provide stereo views of an event. There were 304 X chambers and 152 each of U and Y chambers.

4B.1b. The proportional wire chambers.

Prompt information from a neutrino interaction within the detector was gathered with a system of **proportional wire chambers** that traversed the detector, one per module, to make trigger decisions. In addition, pulse height information on charged particles passing through these chambers was gathered, allowing a cross-calibration of the flash chambers' response to energy deposited by particles to the proportional tubes' response. The pattern of hits was latched and stored to give a useful starting point when analyzing the data off-line in determining the boundaries of each event and in deciding whether a given set of hits recorded by the flash chambers was in fact due to an event in time with the event trigger.

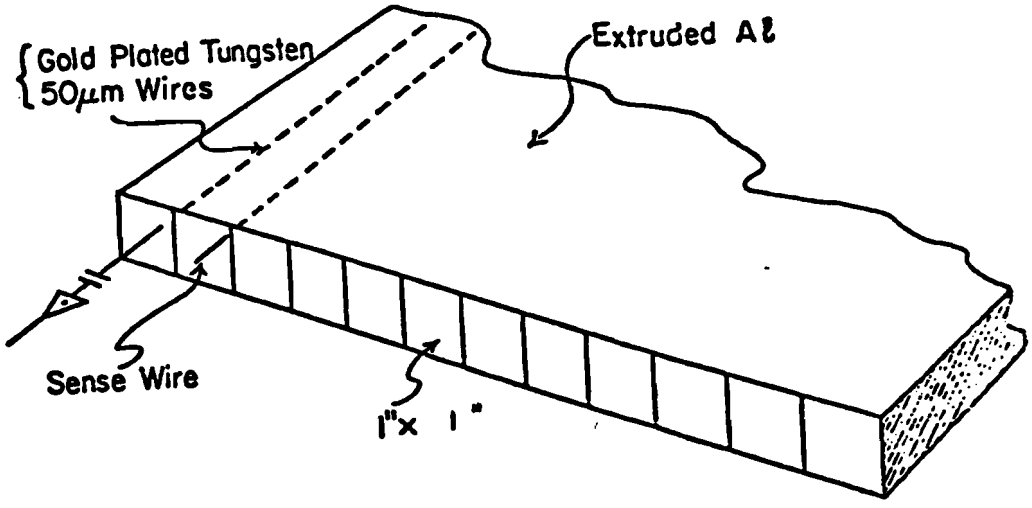

Figure 4–4. Proportional wire chamber.

The proportional wire chambers (figure 4–4) were constructed of extruded aluminum sections 12′ (3.6 m) in length in the shape of eight rect-

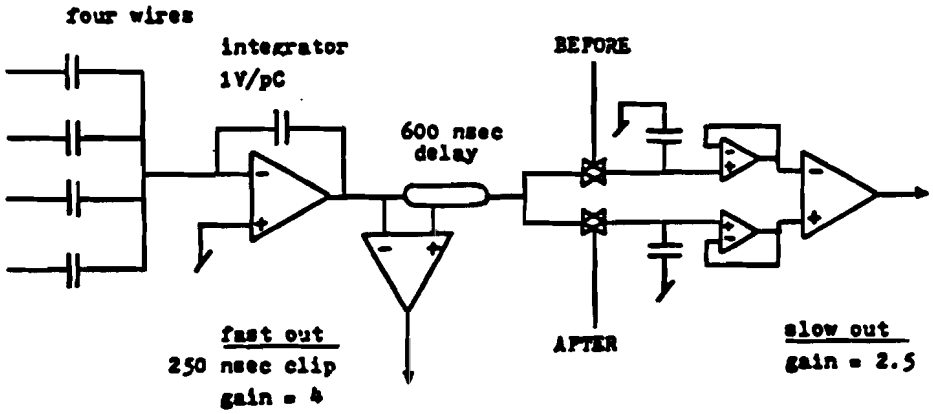

Figure 4–5. Proportional chamber integrating amplifier schematic.

angular cells with inner dimensions 0.840″×0.910″ (2.13 cm × 2.31 cm). Eighteen aluminum extrusions placed edge to edge made up a single 144 wire plane. There were 5300 wires in the entire calorimeter. To provide two views of an event, vertical cells and horizontal cells alternated in successive modules. There was a gold plated tungsten anode wire strung down the middle of each cell, 50 μm in diameter. This was supported at each end by a pin passing through a nylon bolt which made a gas seal in the walls of an aluminum gas manifold. The gas mixture was 90% Ar–10% CH_4 (P-10), and was supplied at 0.5 ft^3 hr^{-1} or one volume change per day, without recirculation.

A positive voltage of 1600V was applied to the anode wire to give a gas gain of approximately 3000. The negative-going signal pulse passed through a blocking capacitor to the input of an FET integrating amplifier which had a gain of 1 V/pC. (See figure 4–5.) There were 1300 amplifier channels in the calorimeter. Four adjacent tubes shared a common amplifier channel to provide 4″ (10.2 cm) spatial resolution. A monolithic 600 nsec tapped delay line differentiated the signal to form the **fast-out** signal which was passed along coaxial cable to the trigger electronics, discriminators, and ADC units. Also, a track and hold system of CMOS switches allowed the signal pulse to

charge up a capacitor which was read out much later over twisted-pair cables to give pulse height information (the *slow-out* signal). To insure integrity of this stored charge during the time when the flash chambers PFNs generated their high voltage pulse, these switches and the signal lines that controlled them had to be protected against transients and the capacitors were selected specifically for their low leakage rate. Tests of the chamber response with and without the flash chambers triggering indicated that these were sufficiently protected against noise. Small Cd^{109} sources mounted directly over the cells allowed calibration of pulse height response between event triggers, so that any variation of the gain with the pressure of the gas or the applied voltage could be detected.[2]

4B.1c. Absorber planes.

The major contribution to the mass of the detector was in the absorber planes. They provided both a target for the neutrinos and a medium for the development of hadronic and electromagnetic showers. In this experiment the absorber material was constructed of hollow acrylic extrusions filled with either sand or steel shot. Each flash chamber was sandwiched between one sand plane and one shot plane. This yielded an average sampling distance of $3\%\lambda = 22\%X_0$ for the flash chambers and $50\%\lambda = 350\%X_0$ for the proportional chambers. The heavy atoms composing the absorber planes constituted a target which was close to isoscalar.

4B.2. The muon spectrometer.

The other major portion of the E594 detector was the system of bending magnets and proportional wire chambers downstream of the calorimeter to measure the momenta of energetic muons produced in charged current neutrino interactions. This momentum could then be combined with the

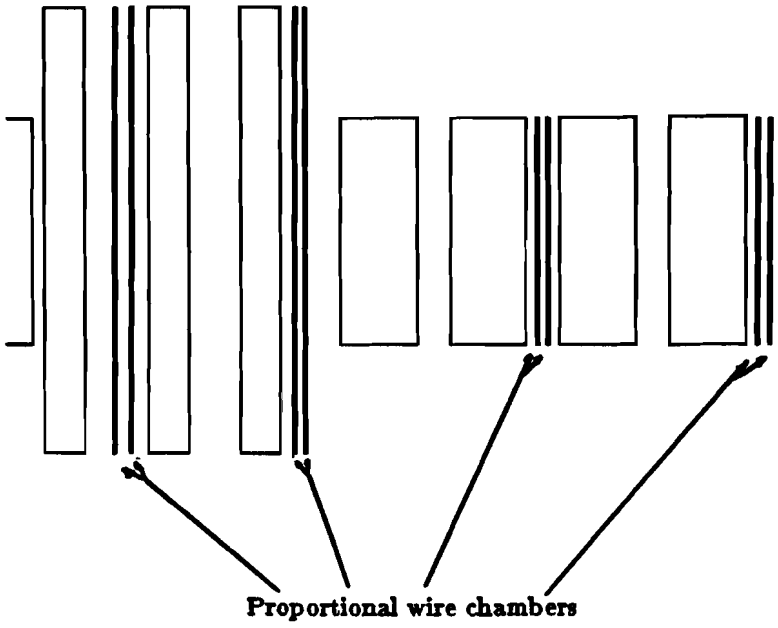

Figure 4–6. Toroidal spectrometer magnets.

muon angle and neutrino energy measured in the calorimeter to specify the kinematics of an inverse muon decay event.

The *magnets* were made from large pieces of iron, the first three being 24′ in diameter and 66 cm in thickness, the last four 12′ in diameter and 125 cm in thickness. There was a 2′ wide hole passing through the centers of the 24′ magnets and a 1′ hole through the 12′ magnets. (See figure 4–6.) The total length of the spectrometer was 40′. The toroidal field was established by passing current through turns of multilayer copper conductor which were cooled with low conductivity water. The field in the iron was nearly saturated and has been measured by means of Hall effect probes. The sense of the field could be set to focus negatively charged muons from neutrino interactions in the calorimeter or positively charged muons from antineutrino interactions, or the magnets could be degaussed for alignment studies.

The toroid proportional chambers[3] were similar to those used in the

calorimeter, but with some important differences. To achieve the required momentum resolution, one needed 0.5″ (1.3 cm) resolution in the sagitta of each muon track coordinate. The following changes to the calorimeter proportional chambers were required. First, instead of using eight cell single layer extrusions, a fifteen cell extrusion was developed with one half cell offset between the two layers. (Cross section shown in figure 4–7.) Also, in order to be able to use the same sort of amplifier used in the calorimeter, a charge division scheme was devised that used two amplifier channels to determine which among several neighboring wires was struck. In this way, a single pair of amplifiers could serve eight cells in the 12′ and in one of the pairs of 24′ chambers, or sixteen cells in the remaining 24′ toroid chamber. This method is described in detail in Appendix C. To provide the increased gas gain needed for charge division the anode wires were at a potential of 1950 VDC, giving a gas gain of 3×10^4. The extrusions were 12′ long in the 12′ toroids, 16′ and 24′ long in the 24′ toroids. The toroid planes were self-triggering and auto-resetting so that the entire amount of charge deposited by a muon could be collected and amplified independent of the varying drift time.

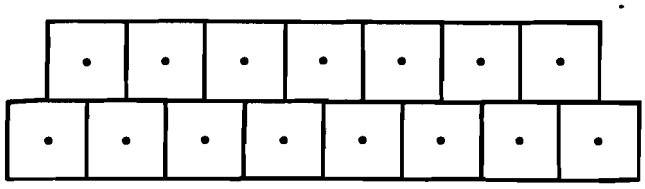

Figure 4–7. Toroid proportional wire chamber extrusion.

There were a total of 3456 wires instrumented in the toroid chambers, with two pairs of double planes in the 24′ magnet gaps and two pairs of double

planes in the 12′ gaps. Each pair consisted of a plane of vertical wires and a plane of horizontal wires. The same gas mixture used in the calorimeter was supplied to the toroid chambers, 90% Ar–10% CH_4, at about 1 ft^3 hr^{-1}.

4B.3. The trigger logic.

The prompt information from the calorimeter and toroid proportional chambers and the liquid scintillators could be combined in a great number of ways to create specialized triggers for particular applications. This section will first catalogue the elements that made up a particular trigger, then describe the two triggers used in gathering inverse muon decay data.

The fast-out signals made by differentiating the integrating amplifier output from each of the 36 channels in a plane were processed with fast electronics on the plane to provide several output signals. An analogue summing circuit on the "Sum and Multiplex" board added up all the fast-outs on that plane to make a **sum-out** signal Σ. On the "Electron Logic Board" the individual fast-outs were discriminated with a 20 mV threshold to form the **hit bit** NIM level logic signal for each amplifier channel. An analogue signal with height equal to 60 mV times the number of hits bits set on a plane was also generated; this was the **analog multiplicity** signal AM.

These fast signals were sent through 50Ω coaxial cables to a second stage of logic residing in NIM standard bins. Cable lengths were adjusted so that the signals from different planes would arrive at the logic simultaneously. The sum-out signals were added linearly to give a total pulse height or **sum-sum** signal $\Sigma\Sigma$ to measure total energy deposited. To form the pre-trigger condition M, the sum-outs were discriminated with a threshold of 50 mV; if the signals from two or more planes exceeded this, M was generated. The analog multiplicities were discriminated and the N condition was satisfied if

more than some preset fixed number of these were above a preset threshold. All of the digital signals were latched for later analysis and all of the analogue signals were sent to peak-sensing ADC units and stored.

The two triggers used to collect inverse muon decay data were the *Quasi* trigger and the *PTH* trigger. The Quasi trigger required that there be hits in the front and back planes of the muon spectrometer, that $\Sigma\Sigma$ correspond to no more than 10 GeV deposited in the calorimeter, and that there be no hit in the upstream scintillator veto counter. This trigger was designed to cut out any large hadronic or electromagnetic shower events in the calorimeter, events where the muon exited the toroid region before reaching the end, and through muon events. The PTH trigger was a low bias trigger formed by the coincidence of the following trigger elements:

$$\begin{cases} \text{M} > 2 \text{ planes} \\ \Sigma\Sigma > 75 \text{ mV} \\ \text{N} > 1 \text{ channel in} > 1 \text{ plane} \\ \text{Front scintillator veto.} \end{cases}$$

Since an average muon passing through the calorimeter deposited 5 GeV of energy, some of the inverse muon events did satisfy this energy deposition requirement, along with some of the quasielastic events. For both neutral and charged current deep inelastic events, this trigger was essentially 100% efficient down to 5 GeV shower energy, with a drop in efficiency below this energy.

4B.4. Beam monitoring and control.

The calculation of the expected number of inverse muon decays depended upon the estimation of the number of neutrinos that passed through the fiducial volume. In this section, we will describe the system for monitoring

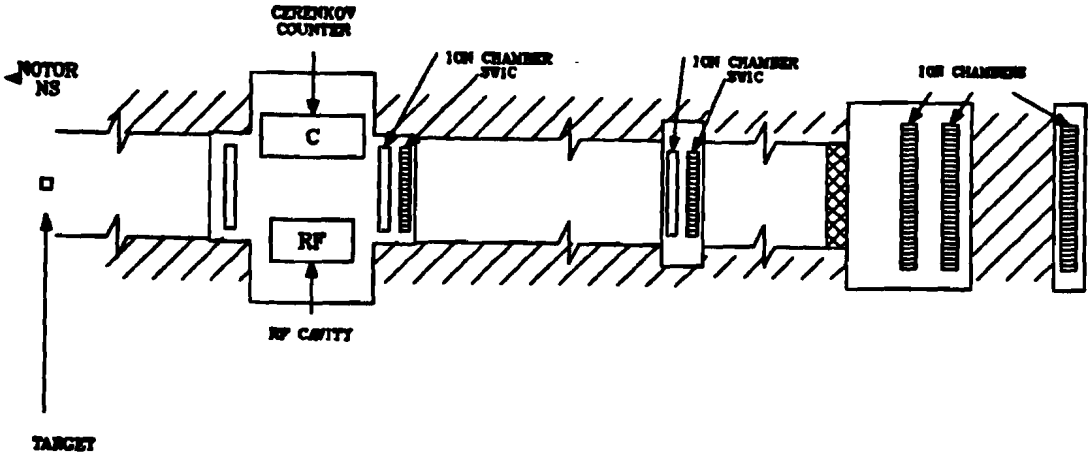

Figure 4–8. Secondary monitor systems.

the number of secondary particles and their composition. We will also make some mention of the beam steering process which was needed to maximize the neutrino flux and to insure that the neutrino beam was centered on the detector.

There were two independent systems for monitoring the secondary flux. (See figure 4–8.) It was important to measure the secondary flux in a redundant fashion because the variation of the response of each system due to environmental changes was different, and also because the averaged measurement using several monitors was more reliable than any single value. The first system consisted of three ionization chambers (referred to as *ion chambers*) located in locations downstream of the proton target. These converted the ionization produced in a volume of gas placed in the beam to a current. The gain of the ion chambers as a function of time was measured by a source gap to correct for variations due to pressure or temperature changes. The second was a resonant cavity tuned to 53.1 MHz (the *RF cavity*) located downstream

of the first ion chamber. This produced a voltage pulse in response to the beam flux. The output pulses of each of these systems were converted to a frequency and scaled to produce digital data which were recorded on magnetic tape. Each of the digitizers was calibrated with known pulses between spills to make sure that its performance was stable. The output of each device was integrated for up to six different several time periods or "gates" so that not only the total number of neutrinos could be determined but also the number that was incident during the live time of the detectors on the neutrino beam line. The master beam gate was synchronized with the passage of the 400 GeV proton beam which was detected by a toroidal pickup.

To give an absolute reference for the beam flux, the output of the RF cavity and of the ion chambers was compared to the observed amount of ^{24}Na produced in a 0.005″ thick copper foil by 200 GeV protons. For this reaction, the activation cross section is known to within about 3%. Corrections to this calibration were made for the differing response of the ion chambers to proton and meson beams and for the effect of the different spill shapes in the foil activation and the neutrino runs on the RF cavity response.

The composition of the secondary beam was measured by a helium differential Čerenkov counter which could be introduced into the beam in place of the RF cavity. This counter had a fixed annular iris, and the counting rate as a function of pressure reflected the amount of each successive charged species making up the beam. The particle fractions thus determined provided a constraint on the simulation of the beam transport which was performed on the Cyber computers. This simulation took the known settings of the train magnets and their geometry and returned a spectrum of particle momenta and spatial distribution at the end of the magnet train, before the particles

reached the decay region. Another computer simulation could then relate these results to an expected neutrino energy and flux at the Lab C detector.

The beam position was monitored by means of a system of split plate multiwire ion chambers. This measured the amount of beam passing on the two sides of a horizontal or vertical boundary to determine the degree of vertical or horizontal mis-steering of the beam respectively. The experimenters would be alerted when this became too great, so that the magnet currents could be corrected. All of the split plate ion chamber outputs, as well as the digitized values of the magnet currents, were recorded on tape.

The systematic error in the neutrino flux contributed to the error in the expected number of inverse muon decay events (see sections 5B and 5C). The estimated error of about 5% is small compared to the statistical error in the observed number of events for any of the cross section tests we have used.

4B.5. Data acquisition.

The large size and fine granularity of the detector along with the relatively high noise environment made the task of data acquisition and storage a major task in this experiment. A typical neutrino event involved thousands or tens of thousands of pieces of flash chamber information as well as proportional tube, scintillator, calibration, and beam monitor information, all of which had to be recorded, packed, and written to magnetic tape.

The flash chambers and proportional chambers were read out using CAMAC compatible crates using 24 bit words. The calorimeter and toroid proportional chambers were addressed separately using separate levels of data multiplexing on the planes themselves and remotely. The data was packed into custom-made CAMAC compatible memory units which were then read onto temporary disk storage by way of block transfers. Flash chamber HV

pulse quality information was gathered by an LSI 11/23 processor with associated memory which then filled CAMAC memory for transfer to the main computer. Monitor information was gathered for the main computer by the MAC system, which also allowed the experimenters to control portions of the beam line. The main computer was a PDP 11/45 that wrote the data onto 800 bpi tape, displayed views of the incoming data on screens in the control room, computed certain statistics for the use of the experimenters to verify that everything was running properly, alerted them when an alarm condition did occur, and did a certain amount of fast data analysis.

4C. Off-line analysis.

In this section we will describe the major parts of the data analysis which were used in the study of inverse muon decay. These include the muon tracking package, the vertex finding routines for quasielastic candidate events, Monte Carlo simulations of the physics of the inverse muon decay and quasielastic scattering processes and of the response of the detector, and data handling routines. Detailed information concerning the software used in the studies of the integrated signal cross section and of the differential cross section are contained in the next chapter where these studies are described. Measures of the performance of several of the routines which were relevant to this thesis are discussed in section 4E below. All of the off-line analysis was written in FORTRAN and run on the Control Data Cyber 175 and 875 computer cluster at Fermilab.

The raw tapes written from the CAMAC units by the data acquisition computer contained the data in a form that was easy to store but hard to read out in a sensible fashion. To solve this problem, a preliminary stage of data handling called *reformatting* was needed; this condensed the data, subtracted

the pedestals from proportional chamber data and the offsets from fiducial marks in flash chamber data, and repackaged each record separately from the others in an orderly arrangement of planes and channels. This simplified the analysis of the data by a large amount and reduced the number of data tapes needed. Only certain rather specialized applications ever needed to use the raw tape information. The analysis routines which are described below all read the data from reformatted tapes.

4C.1. The muon vertex finding routines.

When an event had been identified as a potential inverse muon decay candidate, the vertex routines were called to find the location of the primary interaction and the angle of the muon at this point. The position of the vertex was combined with our knowledge of the dichromatic beam to estimate the energy of the interacting neutrino (see section 4C.4 below on how this was done) and was one necessary input to the muon tracking package (section 4C.2). The location of the interaction was also needed to show where to look for energy that had been deposited by recoil nucleons, nuclear fragments, or other final state hadrons in a quasielastic or low-y inelastic event. The quality of the muon vertex finding procedure and of its applications in this experiment is an illustration of the advantages of good pattern recognition properties in a fine-grained calorimeter.

Only isolated hits were considered within the calorimeter at first; hits that seemed to be associated with many other hits were disregarded temporarily (by using the subroutine CNTRST). Starting at the end of the calorimeter, the process would begin by searching for a string of isolated hits that lined up. The angle and intercept of this track candidate would then define the axis of a limited region or "road" within which the rest of the

candidate muon track could be expected to lie. At this time the hits that had been neglected before by CNTRST were once again taken into consideration. A search for a series of chambers, in any view, containing no hits inside the road would then begin, starting at the end of the calorimeter and proceeding upstream. This location was taken to approximate the longitudinal position of the vertex, with the lateral position given by extrapolating the angle of the track candidate back from the end of the calorimeter. The hits in the vicinity of the vertex would then be fitted via a least-squares method to a straight line in order to refine the slope estimate. Finally, a second search from the end of the calorimeter back to the vertex region for a series of chambers with missing hits would then be performed, using a narrower road.

This approach to finding the interaction vertex through software had the great virtues of reproducibility and speed, which recommend it over the process of visual scanning, with which it in fact agreed quite well. The resolution of the vertex position is discussed in section 4E.2 below.

4C.2. The muon tracking package.

Once a starting point and angle for a muon had been found, the track could then be associated with hits in the toroid proportional chambers. One could then determine the particle's energy by measuring the amount of bending that occured in the magnetic field. The muon tracking package was a least-squares fitting algorithm in several unknowns that analyzed the observed hits, estimated the muon momentum on the basis of the known magnetic field and amount of multiple scattering in the various parts of the detector, and assigned an error in the momentum measurement by using the covariance matrix. It had to be able to cope with the presence of noise hits in the toroid chambers or in the calorimeter. It also depended intimately

on accurate surveying of the two parts of the detector separately and with respect with one another.

The muon tracking process proceeded in two passes, the first using both flash chamber information and toroid chamber information, the second using only flash chamber information. The first pass considered hits in the rear of the calorimeter and fit them to a straight line via least squares. Only hits falling within a road of constant width around the estimated muon track were considered in the calorimeter. Toroid hits were matched on the two sides of the double planes, and were fit to various possibilities for a single track consistent with the known magnetic field. The track candidate and combination of hits which minimized the goodness of fit quantity $\chi^2/d.f.$ (chi-squared per degree of freedom) was chosen. To help eliminate random noise hits, the first pass through the data was performed in two iterations, the second one omitting the one hit that made the largest contribution to $\chi^2/d.f.$ for the best track candidate. The final set of hits for the first pass were used as input for the second pass. This pass fit the hits near the estimated vertex using the same road. In assigning a momentum to the muon, allowance was made for dE/dx of the particle through the calorimeter.

The muon tracking package returned the sign and momentum of the muon, the estimate of the error of this measurement, the $\chi^2/d.f.$ and number of degrees of freedom, and improved estimates of both the track slopes and the errors in these slopes. If an event failed the analysis for any reason, the package was able to communicate the reason for failure to the main program and to tabulate the various failure modes. For debugging purposes, it was possible to print out the results of intermediate steps in the fitting procedure and to vary the values of parameters the package used.

4C.3. The Monte Carlo simulation.

Some aspects of the detector's response to neutrinos were simply impossible to deduce analytically. These included the effect of noise, the efficiency of the pattern recognition routines, the effect of misalignment on the experimental resolutions, and the smearing of the y and Q^2 distributions by the non-Gaussian tails of the resolution. Such effects were investigated by turning to Monte Carlo simulations which would take the best estimates of the kinematics of the particles involved in a reaction, combine these with the best understanding of the physics of the interaction of particles with matter, with magnetic fields, and with detector elements, then simulate the data acquisition process to make data files of fictitious events. These could then be analyzed with the same software used to analyze the real data and the measurements could be compared with the true quantities.

The Monte Carlo package used to simulate the E594 detector was an intricate piece of programming, reflecting in part the complexity of the apparatus. At the same time, since it had many users, each with a different goal in mind, it was designed to be both flexible and easy for a user to operate without much knowledge of its internal operations. At its heart was a list of particles that were generated in the course of an interaction from nuclear and electromagnetic interactions in the absorber medium, from decays, and from the primary vertex. These were propagated relativistically through the detector, made to interact with nuclei in the absorber planes so as to create more particles or to be stopped, decayed, lost energy through ionization, or generated electromagnetic showers. All these processes were modelled with the same lifetimes and ranges that numerous other experiments have measured.[4] The geometry of the detector was included in virtually every de-

tail, the magnetic field in the toroid magnets was modelled, and the different materials that made up the detector were included realistically.

To allow for a reasonable execution speed, a few concessions were made: low energy (<10 MeV) neutrons were ignored, strange particles were not produced, electromagnetic showers were treated by means of a formula for energy deposition rather than as a particle multiplication process, noise was put into the flash chambers in a uniform random way (aside from known "hotspots" and "dead regions" which were included) rather than in the somewhat clustered way it appeared to occur, the trigger conditions were not explicitly made use of in event generation, and the question of noise in the proportional tubes was largely ignored. On the whole, however, these refinements have been studied and have been found not to make very much difference in the final appearance of the events or in the results of most types of analysis. Every attempt to optimize the code has been made, with the result that only about 0.25 seconds of CPU time was needed to generate a single quasielastic or inverse muon decay event. Finally, the response of the detector to calibration beams of hadrons, electrons, and muons has been compared to the results from analyzing Monte Carlo simulated data and, even though the simulation does not itself make use of the calibration results, the responses agreed very well.[5]

4C.4. Neutrino energy determination.

Most applications of the E594 detector to physics in the narrow-band beam required that the incoming neutrino energy be determined to help fix the kinematics of whatever reaction is under study. The way this was done was to use the kinematics of the decay of the secondary pseudoscalar mesons which had been focussed and monitored in the secondary beam line and the

geometry of the beam line itself to define a correlation between the radial position of a neutrino in the detector and its energy.

Since there were two types of pseudoscalar meson produced that could give rise to neutrinos, pions and kaons, the relationship between radius and energy was not one-to-one and it was in fact this aspect that gave the dichromatic beam its name. At a given radius, furthermore, neither the pion band nor the kaon band was perfectly monochromatic either, due to the non-negligible length of the decay region as compared with the distance from the decay region to the detector, and also to the finite momentum bite of the train. There was also contamination from relatively rare decays (such as the pion to electron-neutrino and the three-body kaon to muon-neutrino decays), from wrong sign mesons that would enter the decay region, and from wide-band background neutrinos that resulted from decays of particles which had not passed through the train. To take all of these effects into account, a Monte Carlo simulation of the beam transport process was done using the detailed information on the train and on the secondary beam itself and this generated a series of files that contained the distributions of neutrino energies and types at many different radii from the center of the beam. To use this information when analyzing the true data or when simulating the beam, the neutrino energy package approximated the energy distribution from a given decay mode by two gaussian distributions (one for pion-and one for kaon-band neutrinos) and to interpolate their values between different radii. The value of the distributions at their peaks were used in calculations requiring the neutrino energy using the information from the muon energy to decide whether to use the pion- or the kaon-band value. The performance of the neutrino energy measurement for inverse muon decay events is evaluated in

section 4E.3 below.

4C.5. Utility routines.

There were a great number of miscellaneous routines that made the analysis and debugging of the analysis of neutrino events much easier. The pictures of events that appear in this paper are products of a general event displaying routine and of a graphical output package. There were routines that would read the monitor information that was recorded along with the information from the detector and could compute the number of secondaries that are produced and the number of neutrinos passing through the fiducial volume. Routines that enabled the creation of summary files of kinematic and topological quantities extracted from events allowed easy reanalysis of the data. There were also routines that created alignment, efficiency, and pulse height tables from source calibration and cosmic ray data. Finally, there were the histogramming and data presentation packages HBOOK, HPLOT, and DIGS, which produced most of the plots included in this thesis.

4D. The 1981 and 1982 data collection runs.

There have been two periods of neutrino running and of calibration. The results reported in this thesis came exclusively from the dichromatic beam run and calibration in 1982, so only a brief summary of the 1981 wide band engineering run and calibration will be given here.

The 1981 run comprised several weeks in May–June 1980 for calibration and six months of neutrino running from January to June 1981. The calibration running included exposures to electrons, hadrons, and muons at known energies and angles. The neutrinos were generated by a wide-band horn focussing beamline with 80 kA current through the horn. The decay distance was 349 m. This beam consisted of neutrinos that were very strongly peaked

at low energy, and a flux of antineutrinos an order of magnitude less at most energies. The detector weighed 240 tons total, with 416 flash chambers, and 21 calorimeter proportional chambers. The 24′ toroid proportional chambers had not been installed, and the 12′ toroid chambers were not present for the calibration beam. Various triggers and combinations of triggers were tested, including a low bias energy deposition trigger, an electron trigger, a high Q^2 trigger, and a quasielastic event trigger.

The 1982 run began in January 1982 with neutrino running at various magnet train settings until May, when six weeks of hadron, electron, and muon calibration beam was taken. After this, two weeks of running with the beam collimator closed was taken in order to measure the wide-band background, then studies on cosmic rays were done with the beam off. During periods when the accelerator was operating well, there were up to 1.2×10^{12} protons on target producing about 10^9 muon neutrinos in each spill through the fiducial volume of the detector. This gave a total neutrino exposure of about 5×10^{13} for the whole run (table 5–4). The train was set to focus 100, 140, 165, 200, and 250 GeV/c positively charged particles for the neutrino exposures and 165 GeV/c negatively charged particles (denoted by "−165" in this thesis) for the antineutrino exposure. The +100 and +140 train settings had low numbers of events and peaked at relatively low neutrino energy, so they were not used in the inverse muon decay study.

A diagram of the layout of the Fermilab site and of the neutrino beamline is shown in figure 4–9. Neutral hydrogen atoms which were converted to H^- ions and accelerated in a 750 keV Cockroft-Walton generator, which would feed the 200 MeV linear accelerator after stripping the ions down to bare protons. After this stage, the protons were accelerated in bunches by the

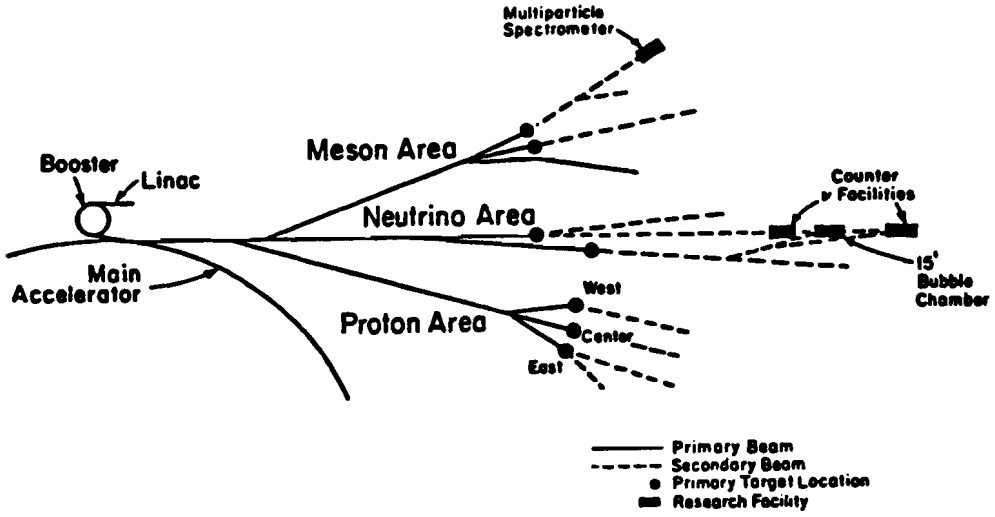

Figure 4–9a. Layout of Fermilab.

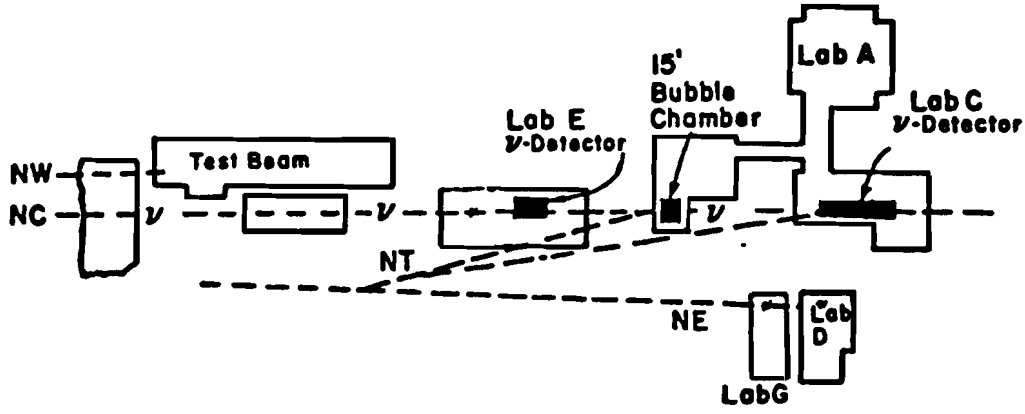

Figure 4–9b. Dichromatic train.

8 GeV booster synchotron, which served as the injector stage to the main ring, a proton synchotron. Here the protons achieved 400 GeV after many turns around the ring; at which time they were routed to the proton switchyard. The beam was divided into three components which were sent to the Meson, the Proton, and the Neutrino beam areas. The absolute normalization of the proton intensity delivered onto the beryllium oxide target in the Neutrino area was done by interposing a piece of copper foil in the beam, which would then be analyzed by nuclear chemical techniques to measure the dose (see section 4B.4). The pions and kaons that were produced in the target were focussed and transported down a train of magnets which could select the desired momentum up to 250 GeV/c. The beam was steered by controlling the current settings of the train magnets via the MAC system. The mesons decayed in flight by the reactions $\pi \rightarrow \mu\nu_\mu$, $K \rightarrow \mu\nu_\mu$, and $K \rightarrow \pi^0\mu\nu_\mu$ in an evacuated decay region. The neutrinos which resulted from these decays would then traverse 1 km of earth which would stop the hadrons that have not decayed as well as the produced muons. The E594 detector was housed in Lab C after the end of this earth shield.

The detector was essentially complete at the time of the run, and the trigger conditions reached more or less their final form as well. Due to the lower neutrino fluxes in the narrow band, the detector was operated on a 100% live basis for both the PTH and the Quasi trigger. If a beam spill passed with neither of these trigger conditions fulfilled, the detector was allowed to trigger on cosmic rays using the liquid scintillators, for alignment and debugging purposes. A few differences from the 1981 calibration run in the flash chamber HV pulse amplitude and timing made corrections in the measured shower energy necessary prior to comparison. There was a

problem in the triggering hardware for the toroid chambers which degraded the spectrometer data for the early part of the run; these runs have been ignored in the present analysis.

A summary of important information concerning the 1982 narrow-band beam run appears in table 4–2.

Table 4–2

Statistics for the 1982 narrow-band beam run

Number of neutrinos in fiducial volume	8×10^{13}
Number of triggers taken	
165 GeV:	28,662
200 GeV:	11,620
250 GeV:	29,278
-165 GeV:	33,040
Primary proton energy	400 GeV
Mean neutrino energy (165 GeV train)	55 GeV

4E. Detector performance.

In this section the response of the detector and of the analysis routines is compared to the expected response. The expected response can sometimes come from calibration, but often one must rely on Monte Carlo simulation to provide such quantities as angular and vertex resolutions.

4E.1. Calibration muon beam.

The best way to measure the energy and angle resolutions of inverse muon decay events was to use a calibration muon beam with a known energy and angle and to compare the software results to the true values. The calibration beam was made up of secondary particles produced by focussing the primary proton beam on a target. These consisted of electrons, mesons,

protons, and muons. All except for the muons were filtered out by inserting pieces of polyethylene ahead of the bending magnets which defined the momentum. Plastic scintillator hodoscopes in coincidence with a "halo" veto (made of plastic scintillation counters positioned off to the sides of the beam) provided the trigger. A problem that one encountered was that since the calibration beam could not uniformly illuminate the detector at all angles and positions, it was necessary to make certain that the portion of the calorimeter that was illuminated by the calibration beam was representative of the whole. The muon calibration beam covered a very small cross sectional area as it traversed the calorimeter, but, since different momenta had different amounts of bending in the spectrometer, different parts of the toroid chambers were illuminated at a given beam angle. Some events were taken with the beam defining hodoscopes displaced so that the muons would enter the detector at a different angle.

Table 4–3. Muon momentum resolution. (Ref. 6)

P_0	P (measured)	$\sigma(P)$	P/P_0	$\sigma(P/P_0)$
22.3	22.9	1.8	1.03	0.08
44.0	44.1	4.1	1.00	0.09
76.8	74.6	8.3	0.97	0.11
108.5	103.1	12.1	0.95	0.11

P_0 was the central momentum setting of the calibration beam
All momenta in GeV

Data were taken at four energies from 22 to 109 GeV (see table 4–3). It was found that the $\chi^2/d.f.$ returned by the muon tracking package was rather sensitive to the range of flash chambers selected in which to perform the angular fit. This has been interpreted as indicating that the error in the magnetic field was small compared with the error in flash chamber alignment.

The fit momentum resolution was found to be:[7]

$$(\sigma(P_\mu)/P_\mu)^2 = (0.11)^2 + (1.49 \times 10^{-3} \cdot P_\mu)^2 \qquad (4.1)$$

and the muon angle resolution to be:[8]

$$\sigma(\theta_\mu) = (1.59 + \frac{97.1}{P_\mu}) \qquad \text{(mrad)} \qquad (4.2)$$

where P_μ is the momentum of the muon in GeV/c.

4E.2. Vertex resolution.

The performance of the vertex finding package for inverse muon decay events was measured both by analyzing Monte Carlo events and by analyzing altered calibration muon events where the upstream portion of the incoming track had been removed. In both of these cases, one knew the expected location of the vertex. In the case of Monte Carlo inverse muon decay events, one also had roughly the same distributions of muon angles and of lateral vertex positions in the detector, so one was not subject to any biases that might have been present in the case of calibration muons which always traversed the same parts of the calorimeter at the same angle. On the other hand, the analysis of calibration muons was not subject to any dependence on the details of flash chamber noise and multiplicity that may have been imperfectly modelled in the Monte Carlo. Finally, one was able to use the redundancy of the three independent flash chamber views to measure how closely the measured vertex reconstructed to an actual point in space.

Table 4–4 summarizes these measurements of the vertex resolution. A few notes on the data samples are in order. The Monte Carlo simulated events consisted of approximately 3000 events constructed with the simulated neutrino spectrum for a magnet train setting of 165 GeV/c, half were

Table 4–4

Vertex resolution

Data set	$\frac{U+Y}{2}$ (cm)	X (cm)	Z (cm)	δ (cm)
Muons, bay 2	9	4.5	18	13
bay 3	8	4.8	3	12
bay 4	9	5.4	9	17
Monte Carlo, V−A	4.0	2.6	1.9	2.2
V+A	5.6	3.1	2.0	2.6

generated with a pure V−A interaction assumed and half with pure V+A. The calibration muon beam events had the hits within a narrow road around either side of the incoming track removed. The road extended from the beginning of the detector to the middle of the second, third, or fourth bay as indicated in the table. Muon energies were 22 and 108 GeV. As for the last column in the table, the quantity

$$\delta = u - y - 2\tan\theta_{uy}(x_0 - x)$$

is the deviation from the ideal matching of the three views. Here, u, x, and y are the coordinates of the vertex in the U, X, and Y chamber views, x_0 is the offset of the X chamber wands, and $\theta_{uy} \approx 10°$ is the experimentally measured inclination of the U and Y chambers from vertical. If $\delta = 0$, the three views for an event reconstructed to a single point in space (whether or not this point was indeed the true interaction vertex). The standard deviation of δ from zero was a measurement of the lateral vertex resolution. We achieved reasonably good performance of the vertex package, although the Monte Carlo resolution outperformed the calibration muon resolution. This may have been due to residual uncertainties in the flash chamber alignment, or mistakes in eliminating the upstream muon hits. For the purposes of the present study, the vertex resolution was adequate both from the point of

view of determining the neutrino energy from its radial position, and for defining regions where hadronic energy from inelastic scattering events may be found.

4E.3. Neutrino energy resolution.

To accumulate enough events to study inverse muon decay effectively, it was desirable to make the fiducial volume as large as possible when analyzing the data. This volume intercepted a beam that was made of mixed pion-band and kaon-band neutrinos. To estimate the neutrino energy, one needed both to determine the neutrino spectrum shape accurately by Monte Carlo studies of the secondary beam train or by analyzing the charged current neutrino events, and to find criteria for assigning individual events to either the pion- or the kaon-band. We will discuss these two tasks briefly here.

As mentioned above, the neutrino energy was returned by a package that relied on distributions provided by a Monte Carlo simulation of the magnet train. These distributions were checked by reconstructing charged current deep inelastic scattering events in the calorimeter with standard energy flow routines. The energy vs. radius correlation was very marked (see figure 4–10a) and the peak energies of the pion and kaon bands were separated by four or more standard deviations at most radii. The quasielastic scattering data showed such a pattern for P_μ (the muon momentum) vs. radius as well (figure 4–10b) out to even larger radii. The inverse muon decay data had a larger range in y than the quasielastics, and P_μ estimates E_ν more poorly. It was possible to use the estimator

$$\langle E_\nu \rangle = \frac{2m_e}{\theta_\mu{}^2}$$

but this would have given an unrealistic estimate of the neutrino energy for ordinary quasielastics (see the discussion of estimators of y in the next

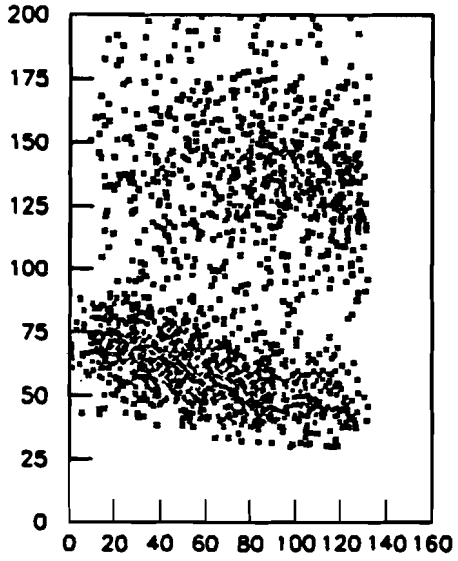

(a)

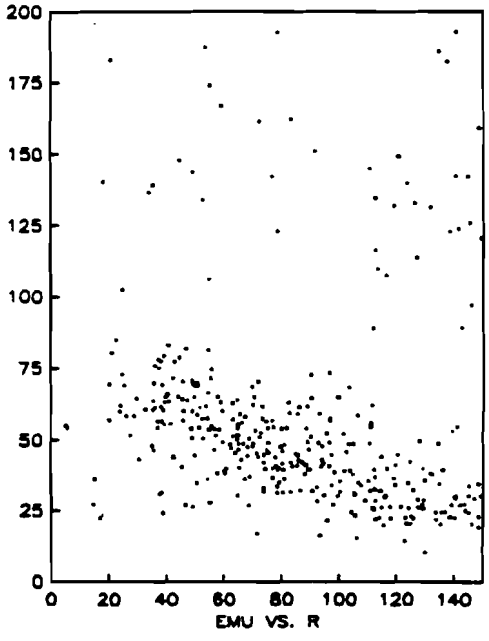

(b)

Figure 4–10. (a) Neutrino energy-radius correlation. (b) Muon momentum-radius correlation.

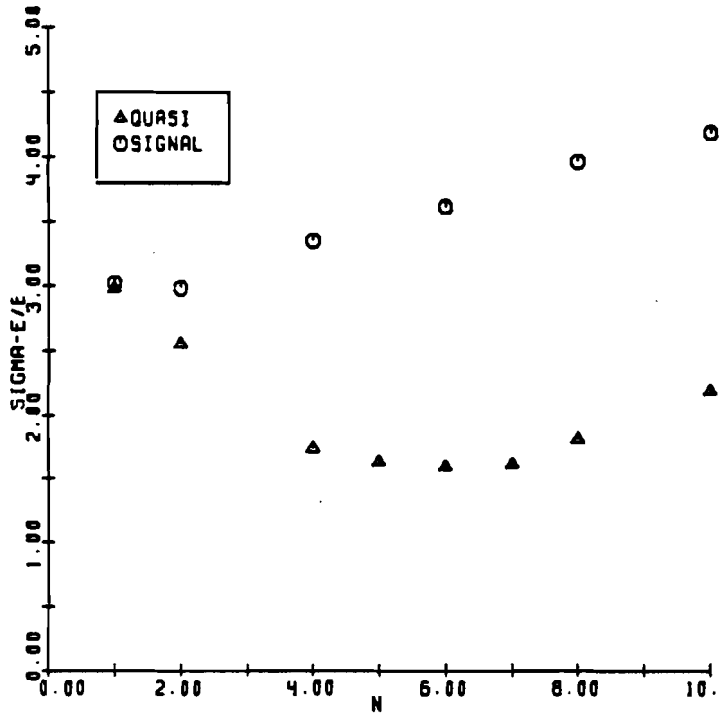

Figure 4-11
Resolution in neutrino energy versus cut location n.

chapter, section 5C). The best way to distinguish quasielastic pion-band neutrino events from kaon-band events was to cut on P_μ, calling all events which had $P_\mu > \langle E_\pi(R) \rangle + n\sigma_\pi(R)$ kaon-band events, where $\langle E_\pi(R) \rangle$ was the mean pion-band energy at the given radius, $\sigma_\pi(R)$ was the one standard deviation spread in the pion-band energy around this, and $n = 6$. The value of n was chosen to minimize the error in energy for quasielastic scattering events (figure 4-11). This did produce a bias by misidentifying high-y kaon-band events as pion-band events and low-y pion-band events in the high-energy tail as kaon-band events, but this effect was small, and was corrected for by analyzing Monte Carlo generated events.

CHAPTER V. RESULTS

In this chapter we shall describe the two ways in which the data have been analyzed to search for inverse muon decay. The first section will introduce the preliminary cuts applied to the data to isolate the candidate inverse muon decay events from the background. A description of the active volume of the detector and an itemization of the number of targets left after cuts will be given in this section. These cuts were applied to the data before performing the two tests, the integrated cross section test and the differential cross section test, which are described in the two sections that follow. Cross checks of the results using Monte Carlo generated data are discussed within each of these sections. The last section of the chapter will give the limits placed by the present experiment on the parameters of the two non-V−A theories given in reference 1 and discussed in Chapter 3.

5A. Cuts on the data.

On account of the very large number of triggers taken in the narrow-band beam run (table 4-2) the only practical strategy for searching for a rare process such as inverse muon decay was by prescreening the data on the basis of features that may be analyzed by computer. Loose criteria were imposed to accept all of the quasielastic candidates, while eliminating events that were clearly irrelevant to the present study—those due to cosmic rays, noise, inelastic scattering, stray beam muons which intercepted the detector, and neutral currents. Events that passed these loose cuts were recorded on tape.

More stringent cuts refined the data sample leaving only fully analyzable events. These were cuts on the position of the vertex within the fiducial volume, the proper success codes for the muon tracking package and for the vertex finding package, the absence of hits around the vertex, and the correct muon polarity. The events which passed these cuts were called *inverse muon decay candidates* and were analyzed using the techniques to be described in sections 5B and 5C.

5A.1. Loose cuts.

To arrive at a set of data of manageable size, the condensed, reformatted tapes were filtered. There were three conditions applied to the data: (1) the latch for the Quasi trigger (section 4B.3) must have been enabled, (2) the vertex for the event must have been located successfully using the vertex package (section 4C.1), and (3) the number of hits in a region about the vertex must not have exceeded sixty in all three views combined. The first criterion rejected all events which did not leave hits in the toroid spectrometer and those which deposited too much energy in the calorimeter proportional chambers. The second condition eliminated most of the triggers due to random coincidences and many of the ones that did not originate within the fiducial volume. The third criterion (called a *"Pacman cut"* in reference to the shape of the region around the vertex) rejected events that had a small shower coming from the vertex which did not deposit enough energy in the proportional chambers to inhibit the Quasi trigger. An illustration of how this cut operated is given in figure 5–1. The program counted the number of hits in each of the three flash chamber views which were less than 50 cm from the vertex in that view. (Due to unequal scale factors in the lateral and longitudinal directions, the contour shown in the figure is an ellipse rather than a circle.) For each chamber, at most one hit within the boundaries of

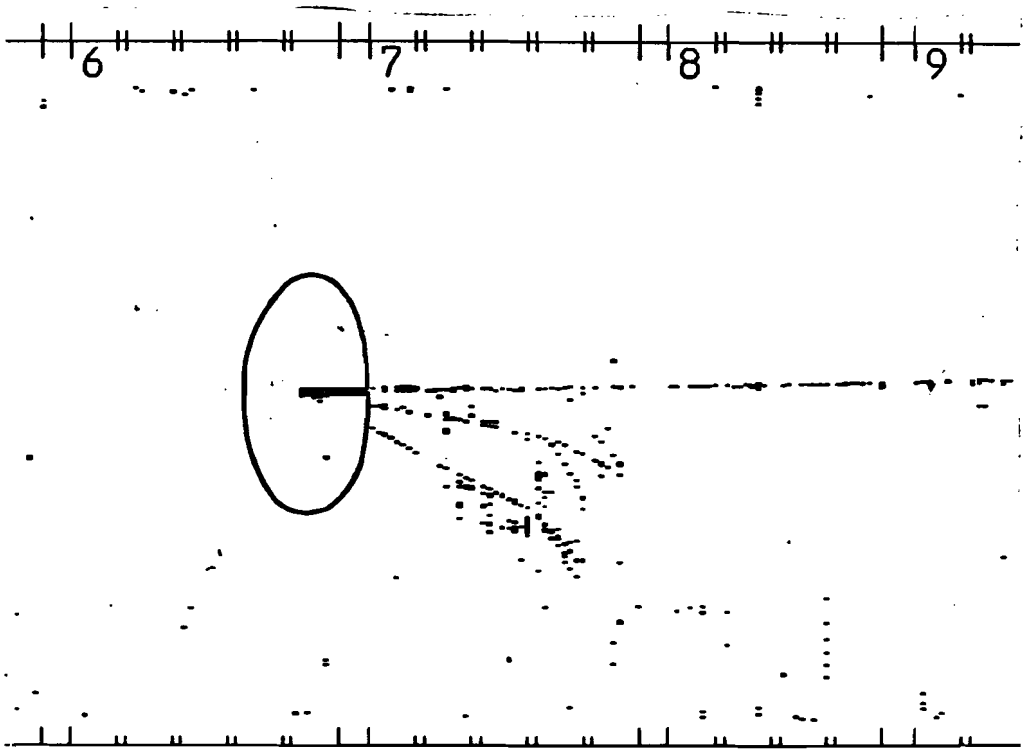

Figure 5–1. Hits around vertex ("Pacman") cut.

a 10 clock count (2.39 cm) "road" defined on either side of the muon track downstream of the vertex may be omitted from this sum. A total of no more than sixty hits in the three views defined a loose cut at this stage.

The events which passed the loose cuts are referred to as "prefilter" events. Monte Carlo simulation showed that these cuts rejected most of the inelastic events but retained nearly all of the quasielastic events.

5A.2. Cuts to identify quasielastic candidates.

The events that passed the loose filter cuts were recorded on disk in the form of four summary files, one for each train setting −165, +165, +200, and +250 GeV/c. These contained the information from the various analysis routines in packed form so that the succeeding software cuts could be varied flexibly without having to mount tapes of the data for each job. Also, summary files in the same format were prepared from Monte Carlo simulations of quasielastic scattering and inverse muon decay events at different train settings and (for inverse muon decay) different choices of the vector- and

axial-vector coupling constants. The true values of kinematic and geometrical quantities for these events were available for later comparison with the measured quantities.

5A.2a. The standard cuts.

The standard cuts applied to the data were the following:

(1) a vertex must have been found successfully,

(2) the vertex must have been located within the fiducial volume (see section 5A.2b),

(3) an event must have at least four toroid chamber hits,

(4) in a road around the muon track in the calorimeter, there must have been an average of at least 0.4 hits per chamber,

(5) a Pacman cut allowing no more than 30 hits in the vicinity of the vertex was required,

(6) an additional cut on hits downstream of the vertex was applied, (the *"QBOX"* cut, described in section 5A.2c),

(7) the muon package must have successfully analyzed the muon trajectory,

(8) the muon must have been negatively charged for positive train settings, and positively charged for the negative train setting,

(9) the fractional uncertainty in the muon momentum σ_p/p as determined by the muon tracking package must have been less than 30%,

(10) the goodness-of-fit quantity $\chi^2/d.f.$ returned by the muon tracking package must have been less than 16,

(11) the muon momentum must have been between 10 and 400 GeV/c,

(12) the maximum slow-out among channels with the hit bit set in any of the four proportional chambers immediately downstream of the vertex must have been less than 5.0 V (PTHBMX cut).

(13) the sum of slow-outs for channels which had their hit bits set in all proportional chambers must have been less than 2.0 V (PTHBSM cut).

These cuts are described in more detail in the following subsections.

5A.2b. The fiducial volume.

The portion of the detector within which inverse muon decay candidate event vertices were accepted was called the fiducial volume. Both the proper estimation of the number of targets and the measurement of detector and software acceptances within this volume were important in calculating the cross section from the data. It was necessary to discriminate against events that could have been subject to poor analysis by other routines. First of all, muons originating upstream of the detector were rejected by excluding the part of the calorimeter upstream of chamber 10. Second, because the vertex finding package itself performed poorly at large radii where the absorber material ended, the fiducial volume was defined so as to include only those events which originated within 150 cm of the center of the neutrino beam. Finally, because the Pacman cut, the QBOX energy deposition cut (which is described in the next subsection), and the muon tracking package all assumed that the event had occurred sufficiently far upstream in the calorimeter to have left a clear track in the last 50 chambers, the part of the calorimeter downstream of chamber 500 was eliminated from the fiducial volume.

The number of target electrons within the fiducial volume was computed from the known masses and composition of the individual detector elements. The composition of the detector was important because atoms of different atomic mass may have different numbers of electrons per unit mass, depending on the ratio of neutrons to protons. Most of the mass in the fiducial volume was in the iron and sand absorber planes, but the acrylic in the absorber extrusions, the oil in the liquid scintillator tanks, and the polypropylene in

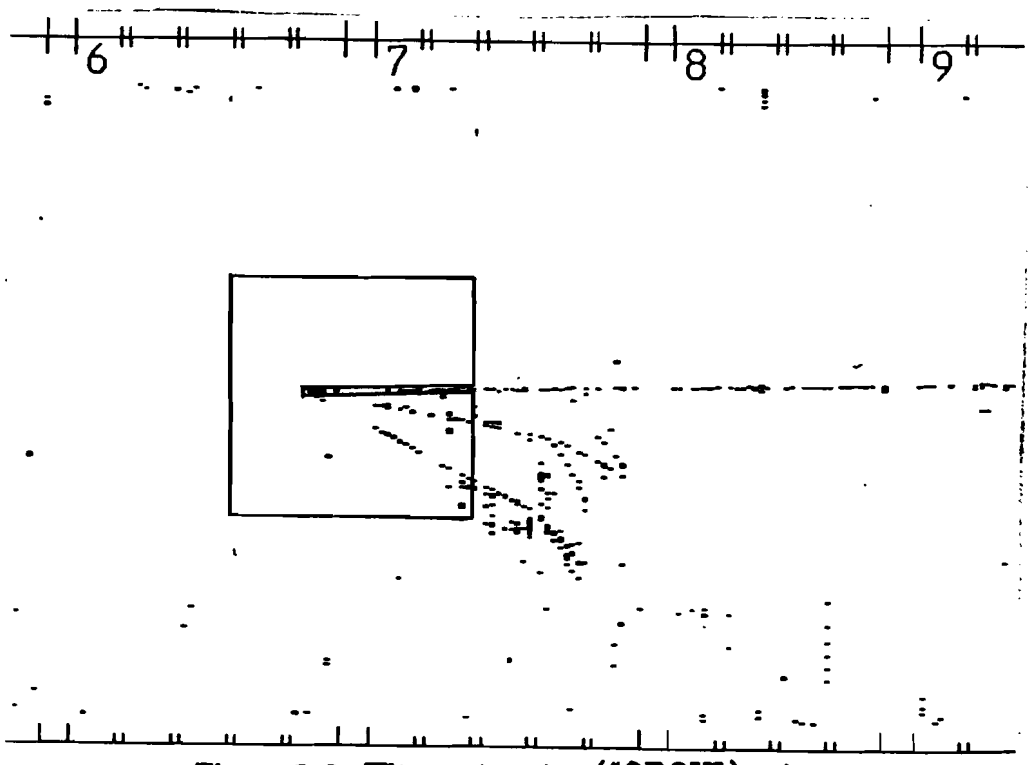

Figure 5–2. Hits past vertex ("QBOX") cut.

the flash chambers did make significant contributions to the total number of electrons owing to the amount of hydrogen in these materials. Table 5–1 gives the total number of electrons for each of the calorimeter components.[2]

Table 5–1. Electrons in fiducial volume

	electron density	# of elements	Total
Per beam	4.479×10^{24} cm^{-2}	135	4.27×10^{31}
Per scintillator	4.384×10^{24}	7	2.16×10^{30}
Per prop. plane	4.874×10^{23}	34	1.17×10^{30}
Grand total			4.60×10^{31}

5A.2c. Filter cuts to discriminate against inelastic events.

These were the cuts that identified events having very little hadronic energy deposition. Number 5, the Pacman cut, (which was described in section 5A.1) was repeated with an upper limit of only thirty hits within the region about the vertex. Number 6, the QBOX cut, was an energy deposition cut which also used the flash chamber information but which focussed more on the area downstream of the vertex, where, according to relativistic kinematics, most of the particles from an inelastic collision would have deposited

energy. This cut counted the number of hits in a box about the vertex extending 50 cm upstream to 150 cm downstream and 50 cm on either side. Hits about the muon track were exempted from the sum, as in the Pacman cut. (See figure 5-2.) A total of 150 hits in all views was allowed. This cut was better than the Pacman cut in identifying events where a small number of hadrons penetrated for some distance before interacting. The cuts on proportional tube response, numbers 12 and 13, were included to help identify events that had energy deposited in an extremely forward direction, where saturation of the flash chamber response might have limited the usefulness of the other two filter cuts. The PTHBSM cut (number 13) specialized in rejecting showers which had penetrated far beyond the event vertex and ordinary showers with an erroneous event vertex. These cuts were performed after the others so as to deal with the least number of events, because the proportional tube information had not been incorporated into the summary files and had to be read directly off of the event records.

The limits on the Pacman and QBOX cut totals were set approximately by looking at the noise hit rate in the calorimeter for muon calibration events scaled by the area of the cut regions. The proportional tube response cuts were also based on the response of the detector to muon calibration events (excluding the first few bays which received a high counting rate during the calibration run) and were relatively loose cuts.

5A.2d. Quality cuts.

The reason for all of the remaining cuts to identify quasielastic candidates was simply to ensure that the kinematic and geometric measurements were of sufficiently high quality to justify further analysis of the event. Most of them were additional checks on the muon tracking package information, upon which nearly all of the observed kinematic quantities relied.

Table 5–2

Events passing second stage of cuts

		Data				+165 Signal MC		Quasi MC	
Cut	Reason	−165	+165	+200	+250	V−A	V+A	+165	−165
0.	Before cuts	1730	1778	796	1089	4467	4416	1723	1588
1.	Vertex failure	1455	1548	680	860	4334	4276	1714	1583
2a.	Upstream	1454	1541	679	856	4333	4276	1713	1583
2b.	Radius > 1.5 m	1174	1189	520	619	4324	4267	1709	1582
2d.	Downstream	1006	1133	492	586	4321	4259	1707	1578
3.	# toroid hits	1048	1086	471	550	4195	3953	1695	1571
4.	# hits in road	1024	1055	460	531	4136	3868	1688	1565
5.	Pacman	466	412	204	227	4024	3761	1655	1555
6.	QBOX	372	320	167	183	3934	3673	1649	1554
7.	Muon package failure	358	307	160	171	3734	3443	1623	1521
8.	Wrong polarity	351	294	151	161	3694	3386	1617	1516
9.	σ_p/p	343	287	145	149	3648	3360	1584	1481
10.	$\chi^2/d.f.$	333	280	142	144	3619	3296	1582	1481
11.	E_μ min	327	274	140	143	3611	3277	1576	1481
12.	PTHBSM	322	269	137	143	3611	3277	1571	1480
13.	PTHBMX	314	259	130	137	3499	3185	1571	1480

5A.2e. Rejection rates.

Table 5–2 summarizes the number of events left after each cut for the data and for Monte Carlo events. The Monte Carlo events were generated in a volume larger than the actual fiducial volume to simulate the contamination due to events which were generated outside of the fiducial volume. Only those events which had been generated within the fiducial volume have been counted in this table. Figure 5–3 displays the fraction of events that survived each cut for each data sample with cut numbers from section 5A.2a along the horizontal axes and percent rejected plotted vertically. The rejection of each of the first six cuts, which discriminate against inelastic events, is shown in the first plot for the data alone. The events which were ultimately rejected because of failures in vertex finding (number 1) had been included on the original condensed data tapes because they had been accepted by older version of the package. These were, in most cases, beyond the edges of the fiducial volume. The next major cut was the one that rejected events with vertices outside the fiducial volume (number 2). One can see the large number of events rejected by the second stage Pacman cut (cut number 5) and by the QBOX cut (number 6) due to hadronic energy deposition. The remaining plots show how the remaining cuts affected the data and the two Monte Carlo simulations, giving similar rejection rates. All of these cuts were below the 10% level. From the plots for signal and background Monte Carlo events one may note the rather low level of rejections overall. There was a higher rate of rejection by the muon tracking package (number 7) for the inverse muon decay events because of the large number of tracks that passed through the holes in the toroids. The increase in the momentum uncertainty (number 9) at the higher train settings for quasielastic scattering events may reflect the increasing muon angle, which decreased the path length in the

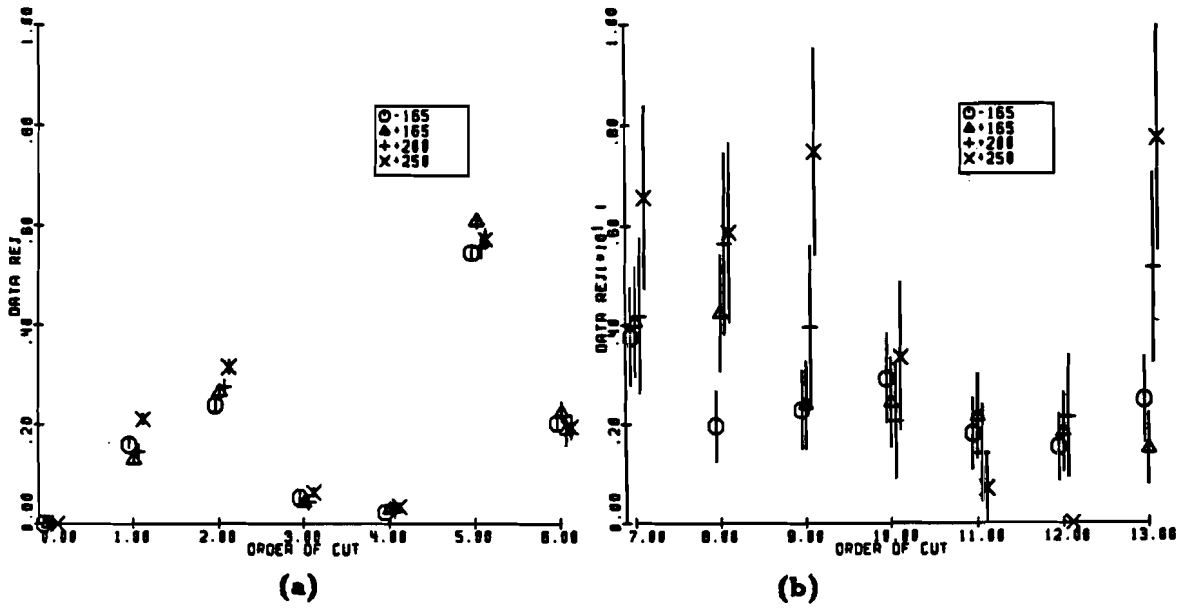

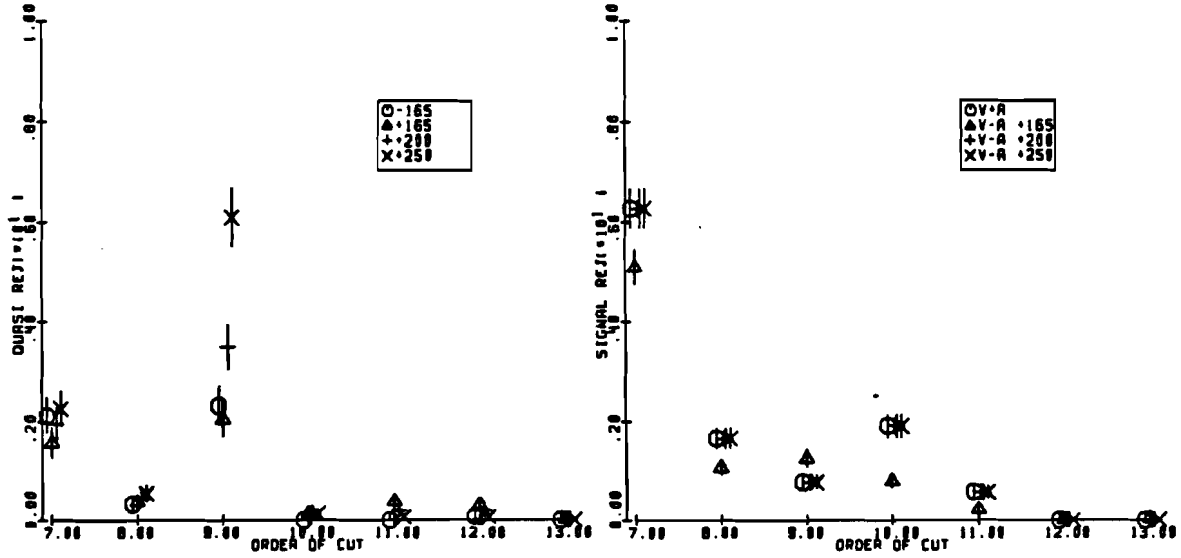

Figure 5–8. Rejection percentages by filter cuts:
(a) and (b) Neutrino data,
(c) Quasielastic scattering Monte Carlo,
(d) Signal Monte Carlo.

(see section 5A.2a for rejection codes)

toroid magnets.

So, within the limits of statistical and systematic error, the data and Monte Carlo sets of events seemed to behave reasonably under the cuts which were imposed. For the earlier filter cuts (numbers 1 to 6) comparison with Monte Carlo would make no sense (because the inelastic portion of the sample was not modelled) and the only cross-check was to compare the positive train settings to the negative setting. Since the Pacman and QBOX cuts had roughly the same rate of rejections, we might assume that these did not significantly reject isolated recoil protons (which were present for the neutrino quasielastic events). The polarity cut (number 8) and the proportional chamber cuts (numbers 12 and 13) exhibited the main discrepancies between data and Monte Carlo sets among the latter seven cuts. These were again readily understood in terms of contamination of the data sample.

5B. The integrated cross section tests.

5B.1. The Q^2 distributions.

With the candidate inverse muon decay samples, we could attempt to do the same sort of analysis that had been done using wide band neutrino beams to identify a low-Q^2 excess in the neutrino events as compared to the antineutrino events. Q^2 was reconstructed from the measured quantities by the formula:

$$Q^2 = -m_\mu^2 + 2E_\mu(E_\mu - p_\mu \cos\theta_\mu) \qquad (5.1)$$

The exact expression for this quantity was $Q^2 = -m_\mu^2 + 2E_\nu(E_\mu - p_\mu \cos\theta_\mu)$ but this formula had the undesirable property of giving negative values when applied to events from kaon-band neutrinos which had been misidentified as pion-band neutrinos. This would have made the computation of nuclear corrections for the quasielastic scattering events impossible, so the slight Q^2

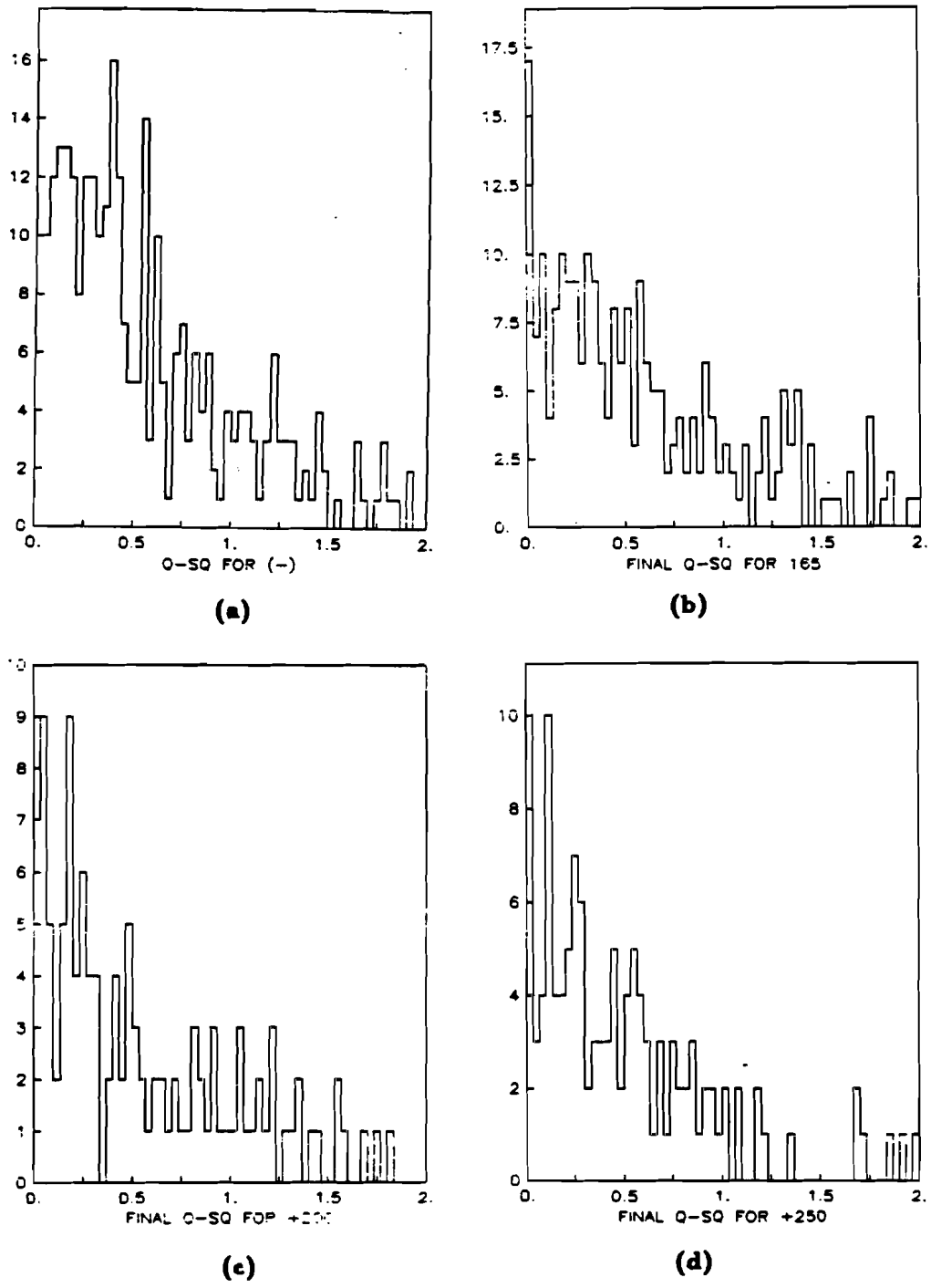

(a) (b) (c) (d)

Figure 5-4. Q^2 distributions, (a) -165, (b) +165, (c) +200, (d) +250 GeV/c.

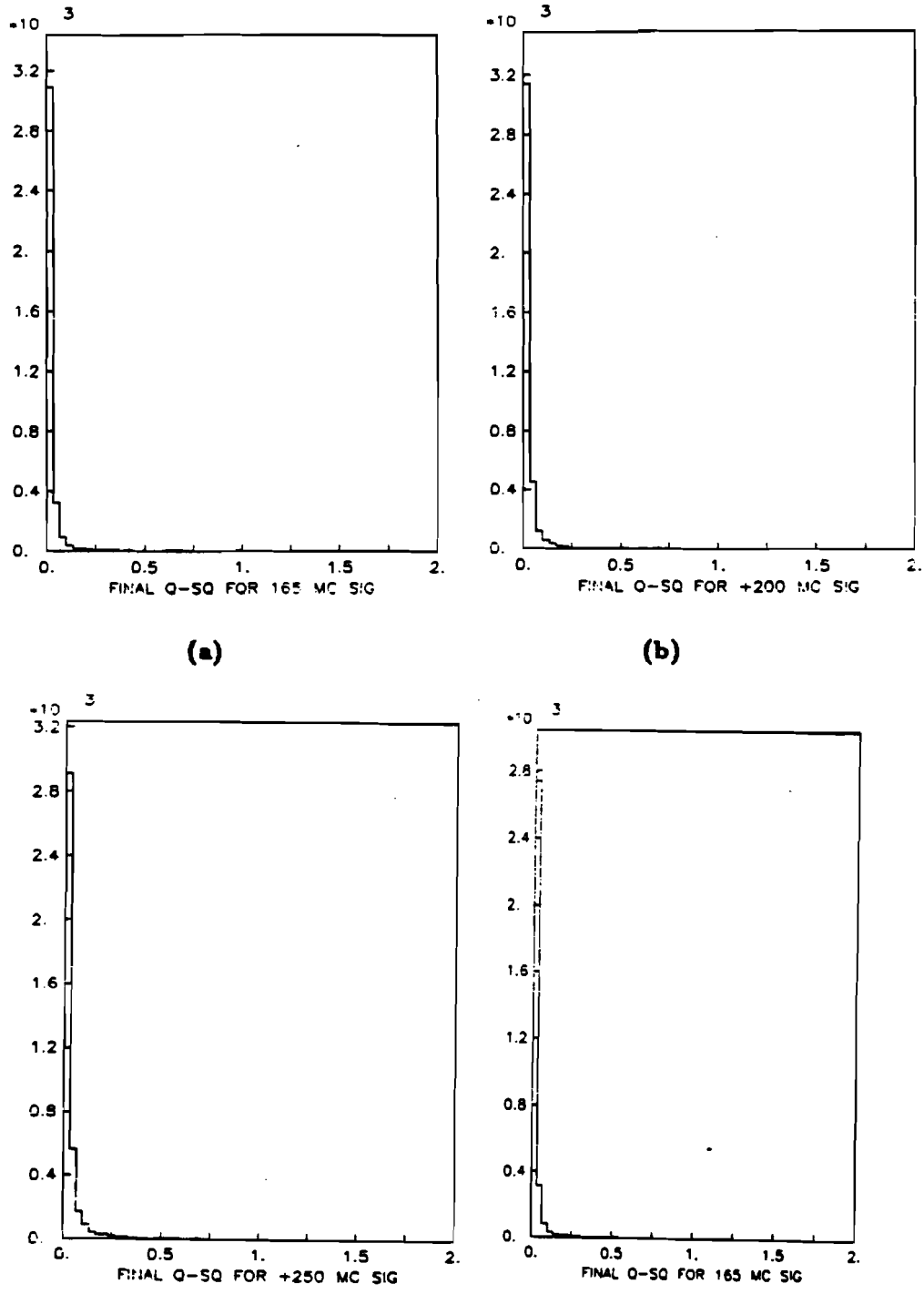

Figure 5-5. Monte Carlo signal Q^2 distributions: (a) +165, (b) +200, (c) +250 (all V−A), (d) +165 (V+A)

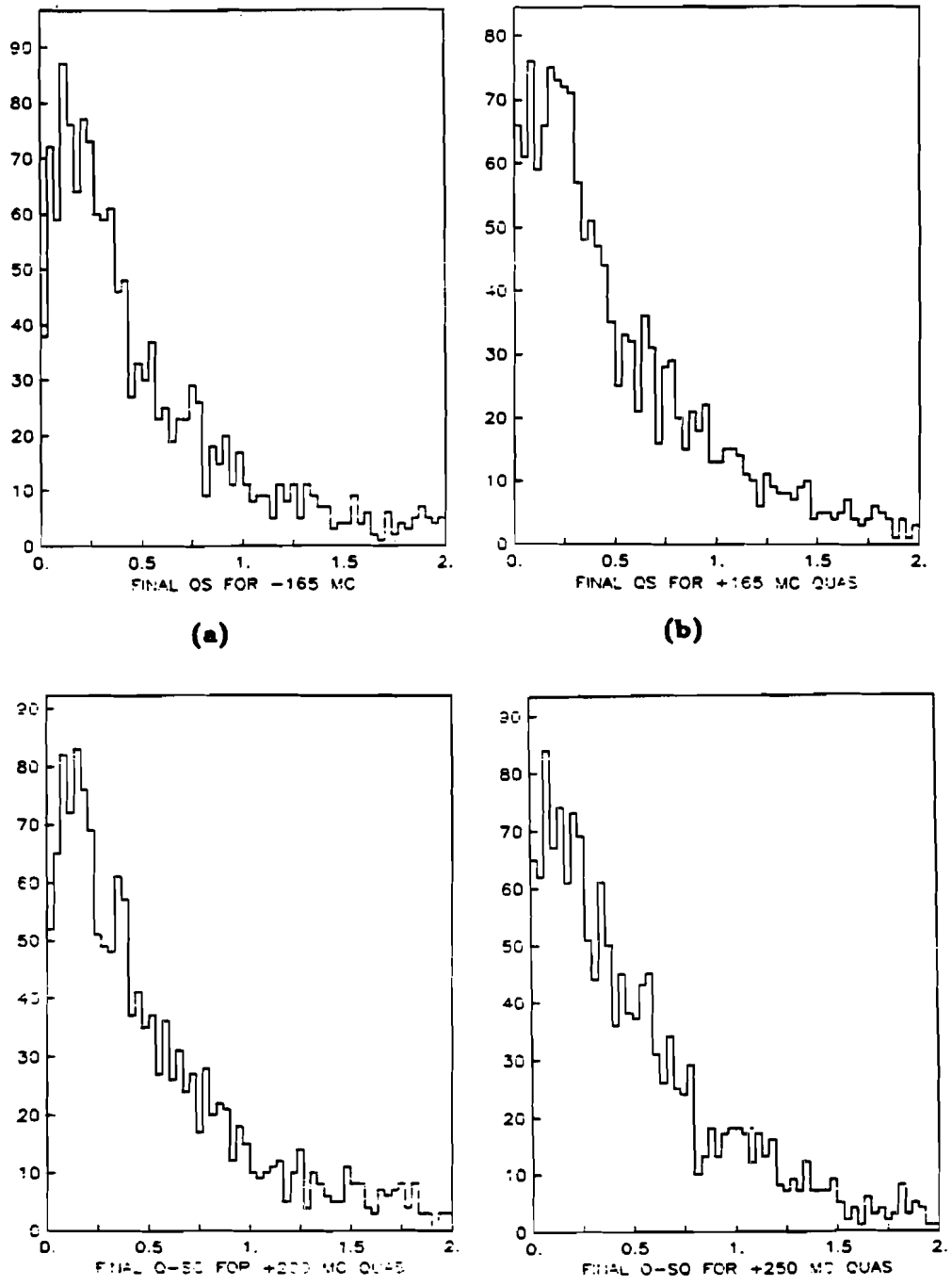

Figure 5–5. Monte Carlo quasielastic Q^2 distributions: (e) -165, (f) +165, (g) +200, (h) +250.

error in equation 5.1 for the inverse muon decay events was tolerated. On account of the extremely small muon angles, a systematic correction for beam divergence, amounting to nearly 1 mrad at a radius of 150 cm, has been applied. The distributions in Q^2 (measured in GeV^2) for the various train settings are shown in figure 5–4. For comparison, the distributions obtained from analysis of the Monte Carlo simulations of pure quasielastic scattering events and of pure inverse muon decay signal are given in figure 5–5. These show the slight broadening of the Q^2 distribution for signal with increasing average neutrino energy, as well as the independence of the distribution for the quasielastic background. Because the shape of the background was insensitive to the energy of the neutrino, it was possible to perform a straight subtraction between the distributions for different train settings. The original bin width was chosen to be comparable to the instrumental resolution; in fact, the true Q^2 distribution for the inverse muon decay Monte Carlo sample was contained primarily within the first bin (Figure 5–5 a through *d*). Events with $Q^2 > 2.0$ GeV^2 were ignored to reduce the contamination of the small number of inelastic scattering events in the distributions.

In order to compare the various distributions so as to check for a low-Q^2 excess we grouped the original binned data into bins containing approximately equal numbers of Monte Carlo quasielastic scattering events. Figure 5–6 plots the low edge in Q^2 for each of the bins at the various train settings. The number of bins was chosen to optimize the resolution in Q^2 while minimizing the sensitivity to statistical fluctuations[3] by requiring that no more than 20% of the new bins contain fewer than five quasielastic candidate events for the data. The rest of the Q^2 study used the rebinned data only.

Since the nuclei of the target material were not precisely isoscalar, the

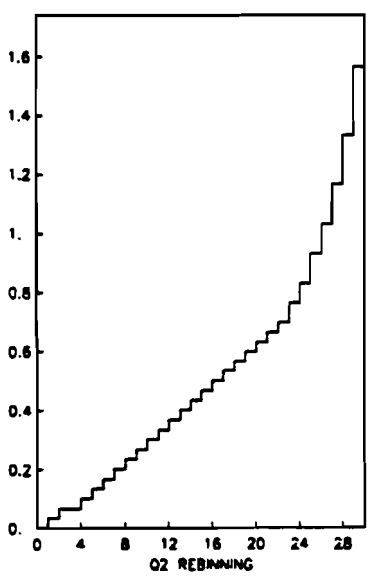

(a)

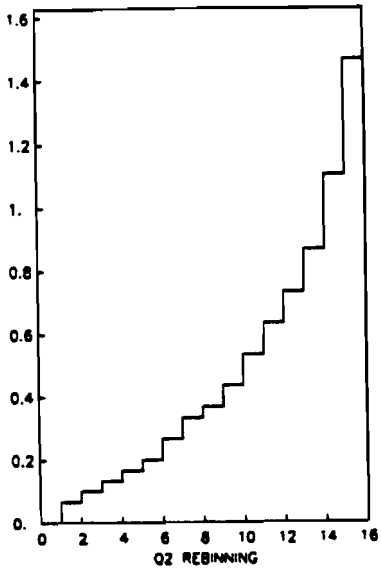

(b)

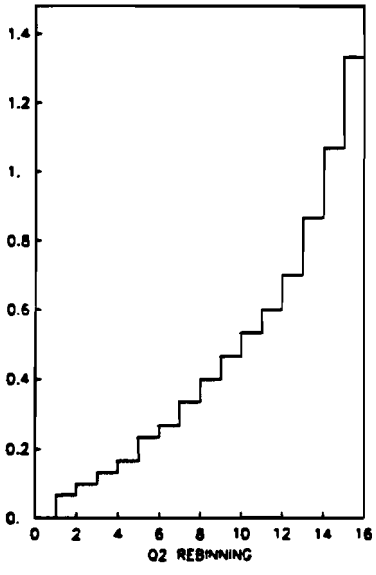

(c)

Figure 5–6. Rebinning scheme in Q^2 (bin number vs. low edge). (a) +165, (b) +200, (c) +250

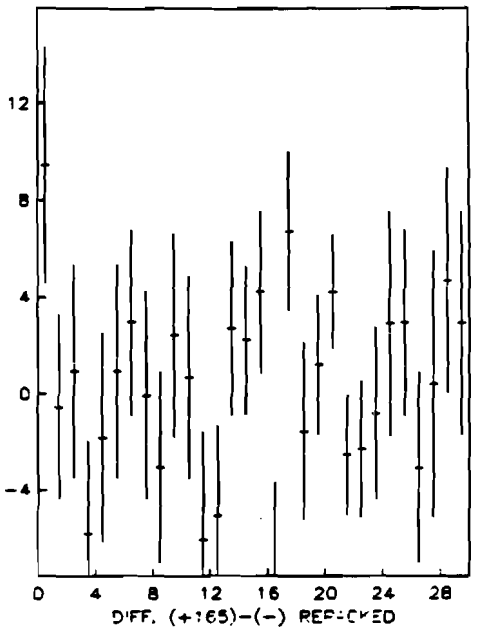

(a)

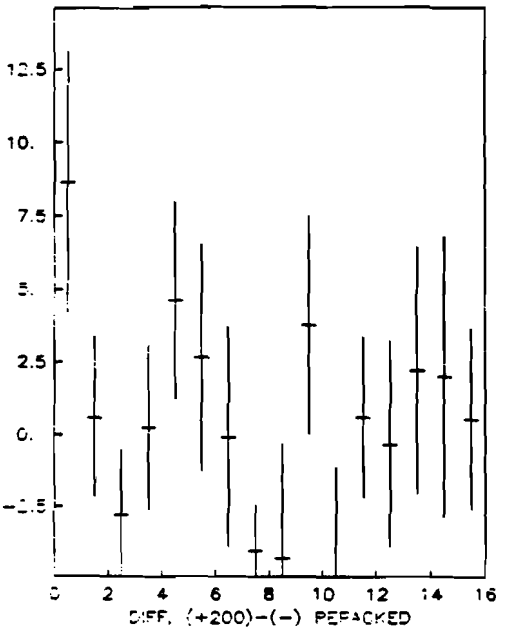

(b)

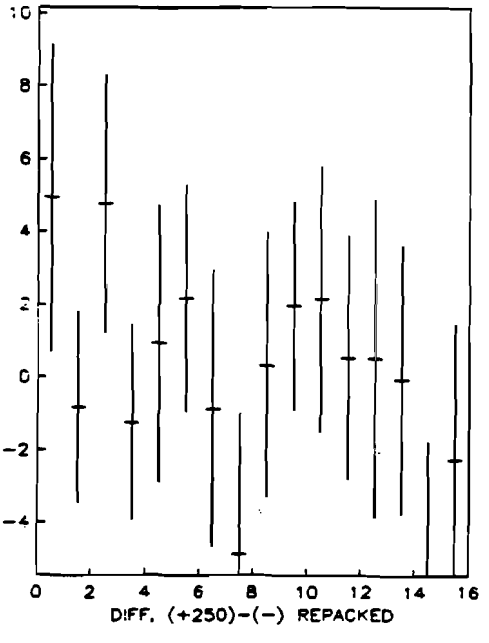

(c)

(a) +165−(−165)
(b) +200−(−165)
(c) +250−(−165)

Figure 5–7. Rebinned differences, Q^2

nuclear effects (Pauli suppression) at low Q^2 gave different values for neutrino-induced quasielastic scattering events and for antineutrino-induced events (section 3C) in the Q^2 region of interest. We used equation (2.5) to find the nuclear correction for each, after determining the average value of $|\vec{q}|$ at the center of each Q^2 bin using equation (2.6). The antineutrino distribution was then multiplied by the ratio of correction factors.

We normalized the rebinned antineutrino distribution to the neutrino distribution to have the same area past the first bin, before subtracting it. This yielded the series of difference plots shown in figure 5–7. In each of these plots, the abscissa is the rebinned Q^2 given in figure 5–6. An excess of events in the lowest Q^2 bin was interpreted as being a signal for inverse muon decay. The error bar for each bin was calculated on the basis of the bin contents of the histograms being subtracted, using Poisson statistics, before normalization. These statistical errors dominated over the systematic errors from the nuclear correction process.

Table 5–3. Observed and expected low-Q^2 excesses.

		V−A	V+A
Train setting	Observed	Expected	Expected
+165	9.5±4.9	7.2	2.4
+200	8.6±4.5	4.0	1.4
+250	4.9±4.2	5.6	1.9
All positives	23.0±7.9	16.9	5.7

Likelihood ratio V−A vs. V+A : 7.0

Table 5–3 gives the Q^2 inverse muon decay signal for each train setting. In this table, also, are the numbers of events as predicted by the pure V−A and pure V+A models, which were calculated in the following manner:

$$\langle \sigma_T \rangle = \int ds\, \phi(s) \int_0^{y_{max}(s)} dy\, \frac{d\sigma}{dy}(s) \qquad (5.2)$$

$$\text{Number expected} = \langle\sigma_T\rangle \cdot N_\nu \cdot (N_e/A) \cdot \eta_1 \cdot \eta_2 \cdot \eta_3 \qquad (5.3)$$

where $\phi(s)$ is the beam spectrum in the Mandelstam variable s (Equation 2.3), $y_{max}(s) \equiv (s - m_\mu^2)/s$ is the maximum y at a given s, $\frac{d\sigma}{dy}(s)$ is the differential cross section for inverse muon decays as a function of s (Equation 2.1), N_ν is the number of muon neutrinos through the fiducial volume, N_e/A is the number density of electrons, assuming a cross sectional area $A = 7.07 \times 10^4$ cm^2. (section 5A.2a), η_1 is the probability that a signal event will lie within the first Q^2 bin (from figures 5–5 and 5–6), η_2 is the probability that a signal event will pass all the filter cuts (from Table 5–2), and η_3 is the trigger efficiency for inverse muon decay candidate events. In calculating the numbers in table 5–3, we used $\eta_3 = 0.86$ for the trigger efficiency as determined from muon calibration data.[4] The likelihood ratio quoted in table 5–3 gives the "betting odds" on pure V−A versus pure V+A as determined from the results at the three individual train settings.[5]

$$\text{Likelihood ratio} = \frac{\Pi \exp\left(\frac{-N_{obs}-N_{V-A}}{\sigma_{V-A}}\right)}{\Pi \exp\left(\frac{-N_{obs}-N_{V+A}}{\sigma_{V+A}}\right)} \qquad (5.4)$$

where the products are taken over the three train settings.

Table 5–4. Acceptance of low-Q^2 signal, number of neutrinos on target and average integrated cross sections.

Train setting	η_1^{V-A}	η_1^{V+A}	N_ν	$\langle\sigma_T^{V-A}\rangle$	$\langle\sigma_T^{V+A}\rangle$
+165	0.86	0.83	2.35×10^{13}	1.07×10^{-39}	0.367×10^{-39}
+200	0.81	0.92	1.01×10^{13}	1.38×10^{-39}	0.47×10^{-39}
+250	0.76	0.91	1.12×10^{13}	1.91×10^{-39}	0.64×10^{-39}
All positives			4.47×10^{13}		

Table 5–4 lists the acceptance of the lowest bin, η_1, for V−A and V+A as determined from Monte Carlo signal distributions, the number of muon neutrinos N_ν obtained from monitor information (section 4C.5), and the

average integrated cross section $\langle \sigma_T \rangle$ in units of cm^2 for V−A and V+A , at each train setting.

5B.2. The $E\theta^2$ distributions.

An analogous analysis of the distributions in $E_\mu \theta_\mu^2$ was carried out, and is illustrated by figures 5–8 to 5–11. Here, as before, the muon angle has been corrected for beam divergence, and the data were rebinned on the basis of Monte Carlo distributions, with a maximum $E\theta^2$ of 40 MeV. The signal distributions were nearly identical for the different train settings, because of the relationship

$$E\theta^2 = 2m_e(1-y) \tag{5.5}$$

and the slow dependence of y_{max} on E_ν. In this variable the shape of the background changed with beam energy and an expression for the nuclear was not available, so it was not possible to normalize the data for different train settings simply. Therefore, the antineutrino data were simply multiplied by the bin by bin ratio of the Monte Carlo quasielastic scattering distributions for the appropriate positive train setting and for the −165 GeV antineutrino setting. This correction was carried out on the basis of the Monte Carlo quasielastic scattering distributions in figure 5–9. The neutrino and antineutrino data were normalized to have equal totals from the second bin to 40 MeV before subtraction.

The results of the rebinned differences are given in table 5–5 along with the number of expected excesses in the $0 < E\theta^2 < 1.5$ MeV bin. Because of the theoretical constancy of the $E\theta^2$ distributions, the calculation of the expected number of events differed from that done in the Q^2 analysis by replacing the η_1 factors with a single acceptance factor, $\eta_4 = 0.86$, for all train settings. Due to the uncertainty in the nuclear correction and because of the difficulty of estimating the covariance of these results with those from

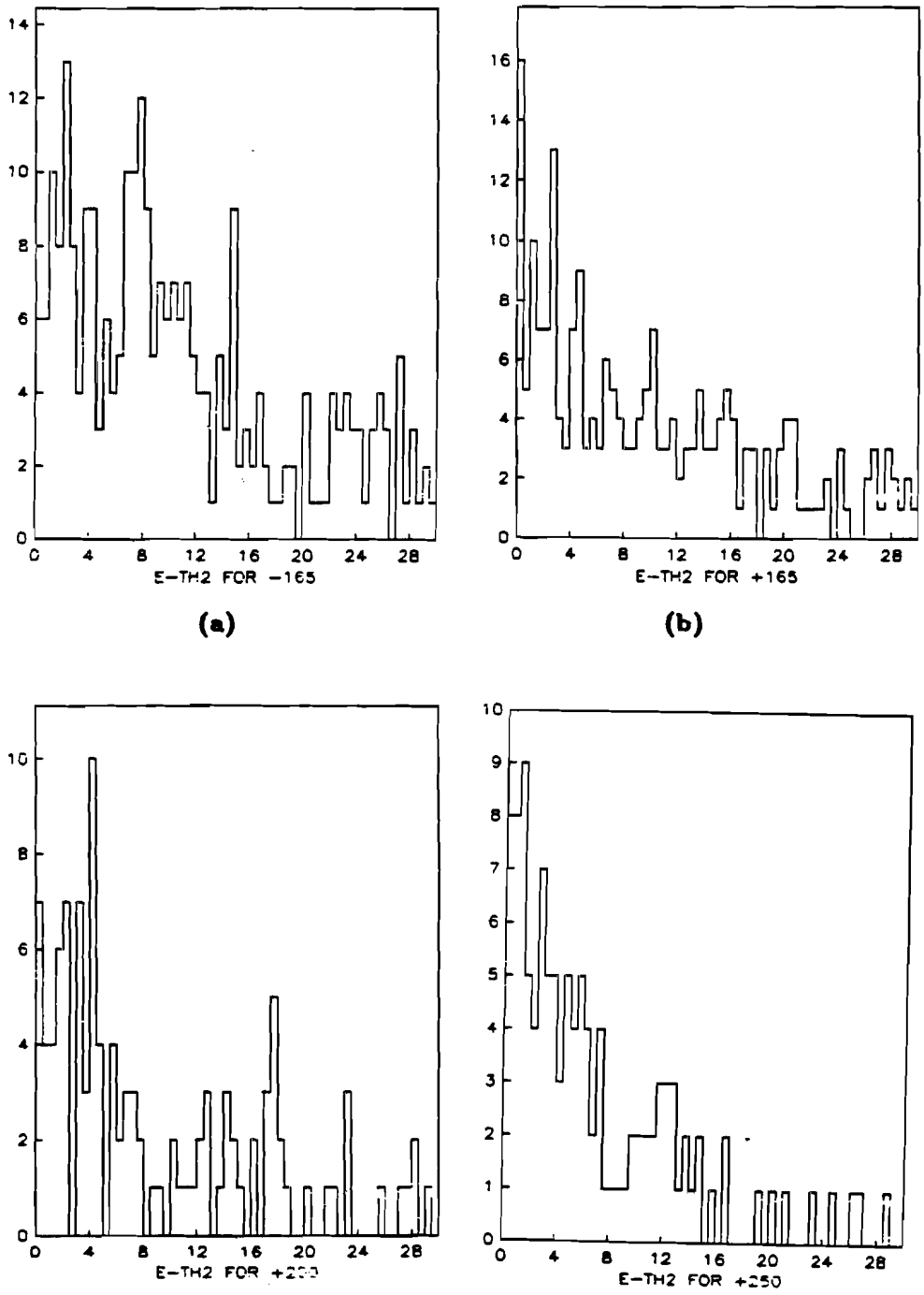

Figure 5-8. $E\theta^2$ distributions
(a) -165, (b) +165, (c) +200, (d) +250 GeV/c

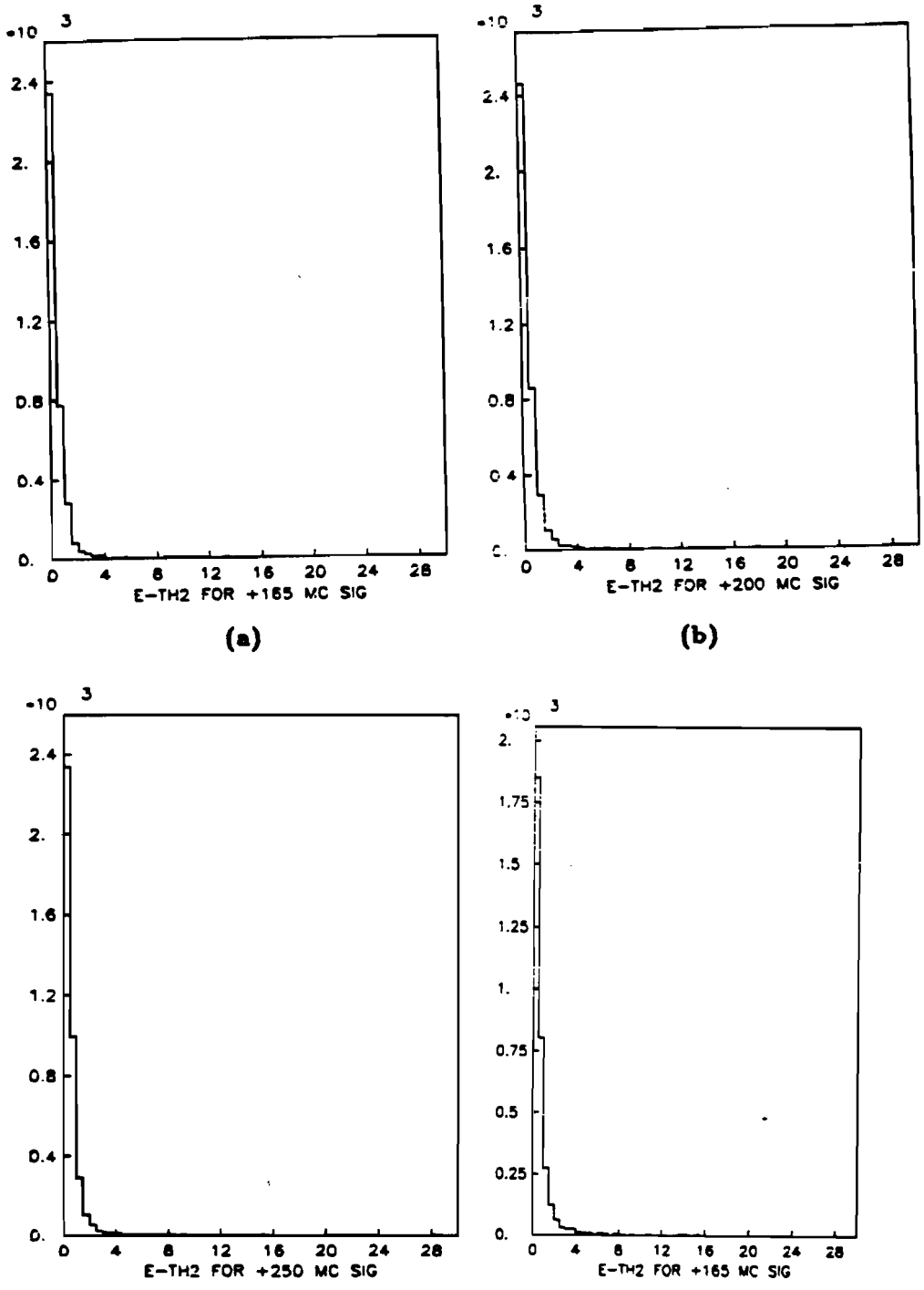

Figure 5–9. Monte Carlo signal $E\theta^2$ distributions: (a) +165, (b) +200, (c) +250 (all V−A), (d) +165 (V+A)

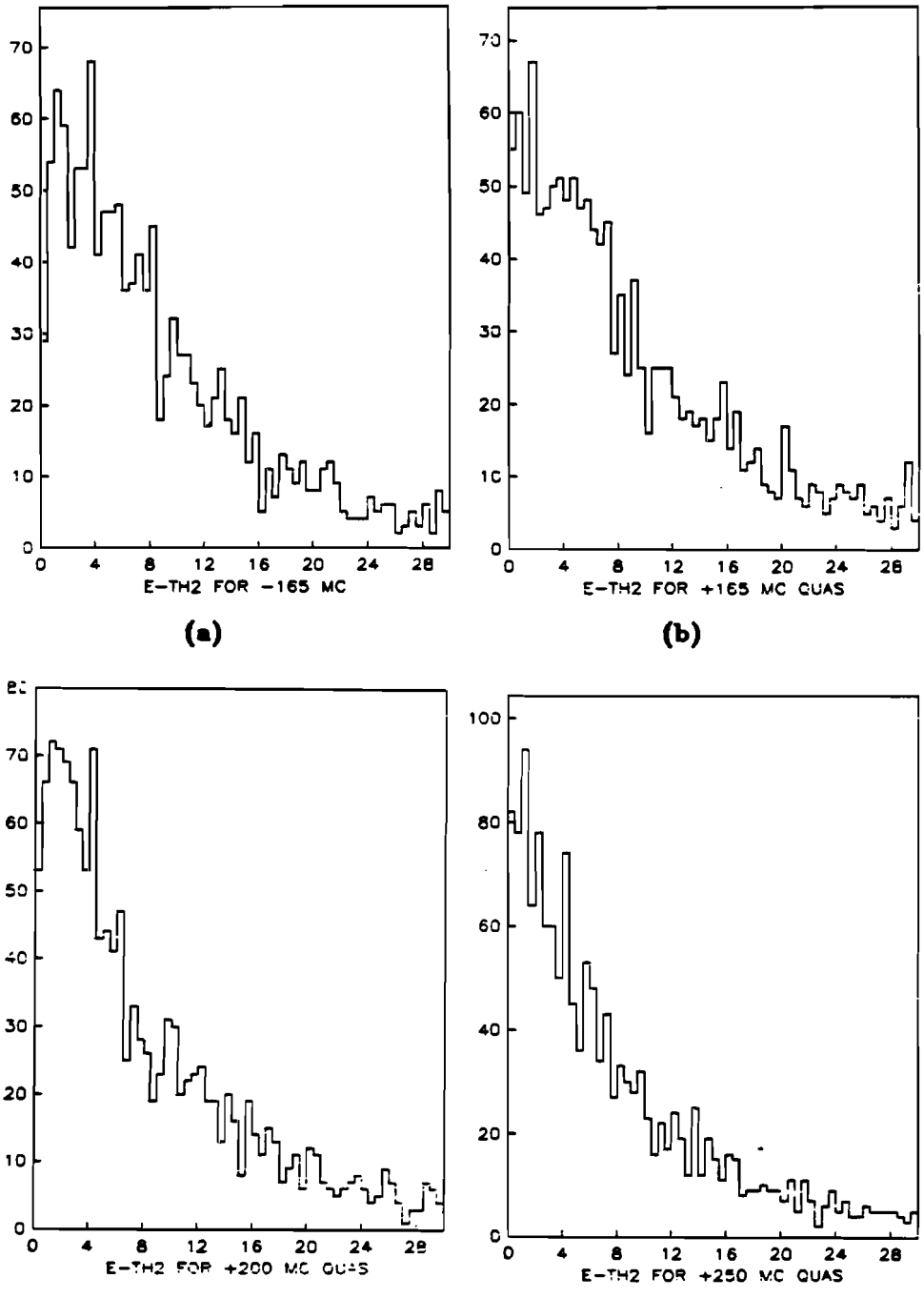

Figure 5-9. Monte Carlo quasielastic $E\theta^2$ distributions: (e) -165, (f) +165, (g) +200, (h) +250.

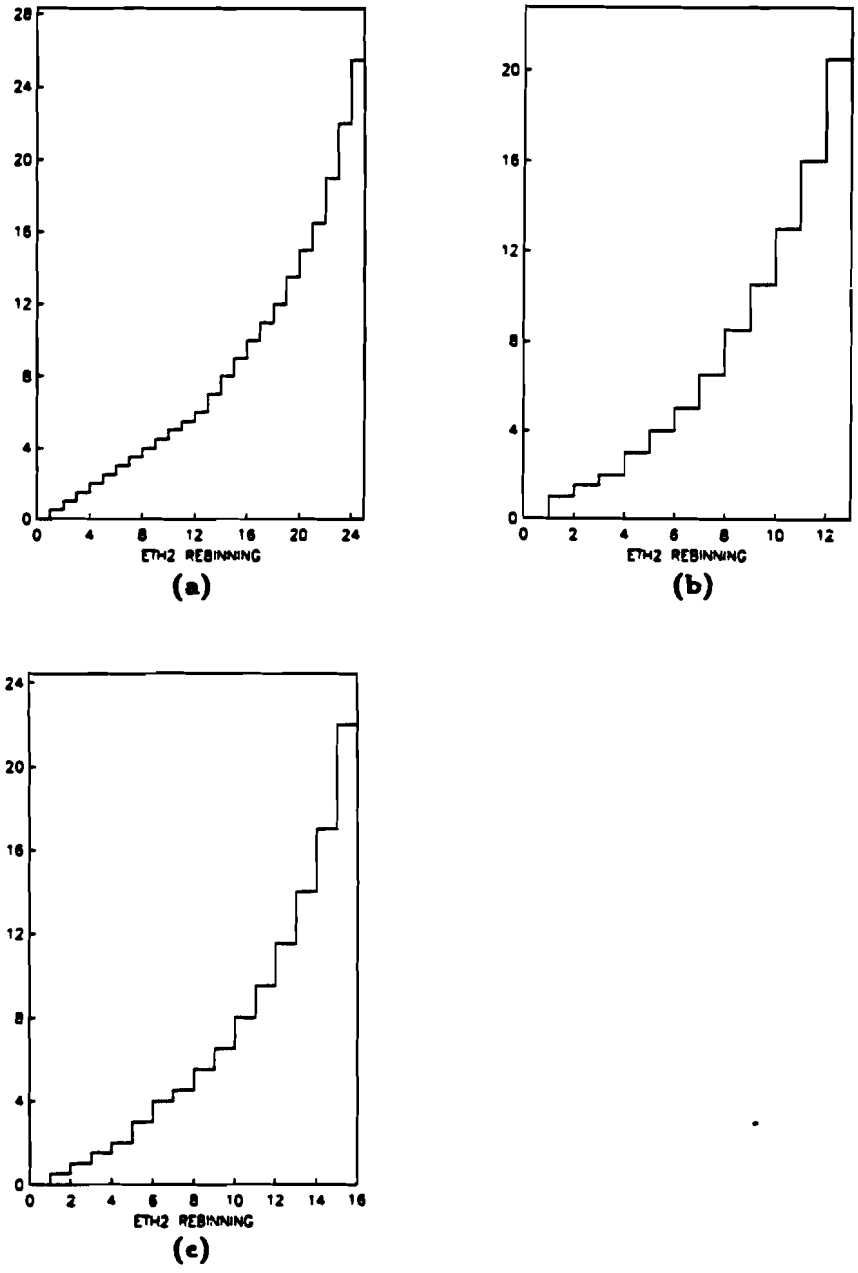

Figure 5–10. Rebinning scheme in $E\theta^2$ (bin number vs. low edge). (a) +165, (b) +200, (c) +250

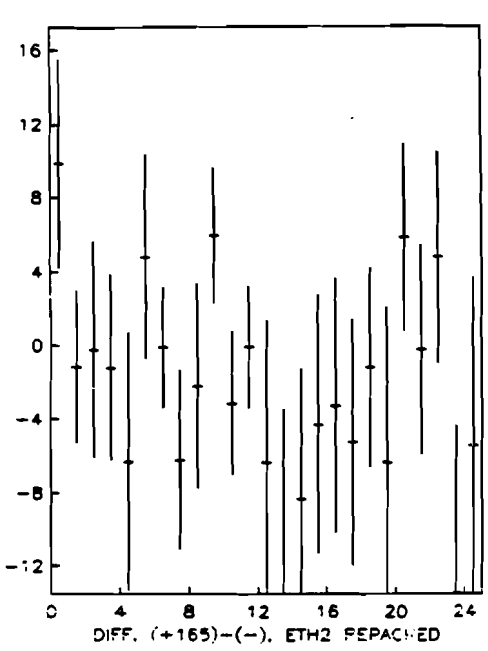

(a)

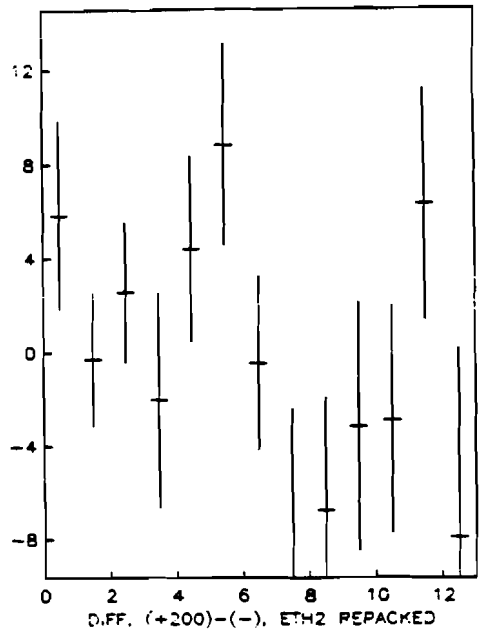

(b)

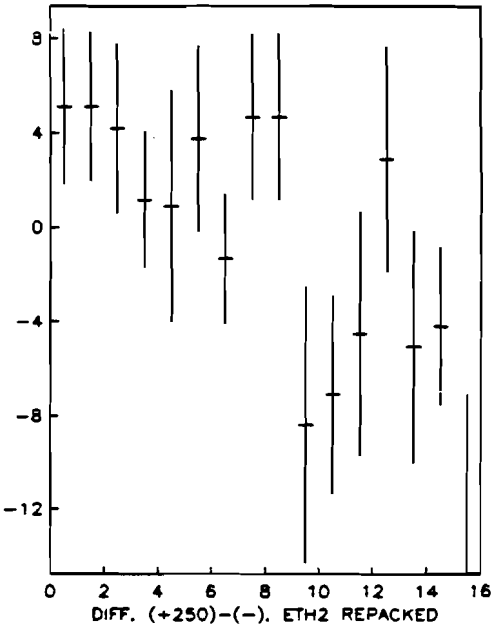

(c)

(a) +165−(−165)
(b) +200−(−165)
(c) +250−(−165)

Figure 5–11. Rebinned differences, $E\theta^2$

Table 5–5. Observed and expected low-$E\theta^2$ excesses.

		V−A	V+A
Train setting	Observed	Expected	Expected
+165	9.9±5.7	5.3	1.8
+200	5.8±4.0	4.3	1.5
+250	5.1±3.3	4.6	1.5
All positives	20.8±7.7	14.2	4.8

Likelihood ratio for V−A vs. V+A : 5.9

the test using the Q^2 distributions, it was decided not to use these numbers in the final estimation of non-V−A couplings. They are mainly intended to bolster confidence in the results of the Q^2 test, as evidenced by the likelihood ratio of 5.9 for V−A over V+A.

5C. The differential cross section test.

It was possible to exploit our ability to judge the energy of the neutrinos produced by the dichromatic train to achieve an independent measure of possible non-V−A couplings in the weak interaction. One advantage this approach had over the integrated cross section tests was its relative insensitivity to the details of the nuclear effects. Another was that this estimate did not depend on the antineutrino data, so that any mistakes in comparing different train settings were eliminated. The technique used was to fit the distributions in y for the data (figure 5–12) to those for quasielastic scattering and inverse muon decay processes (figure 5–13) obtained from Monte Carlo. Although the kinematics of inverse muon decay require that $y = 1 - E_\mu\theta^2/(2m_e)$, a formula independent of the neutrino energy (and, in principle, applicable even to broad-band neutrino data), using this estimator for the data in this experiment was found to result in much poorer results for the differential cross section test and it was rejected. In beams with low average neutrino energy, such as present broad-band beams, the range in y for the inverse muon decay

is very small and difficult to distinguish from the $y = 0$ quasielastic scattering events.

Realistic modelling of the detector response, with adequate statistics, was used. Before fitting, the data were rebinned in a way similar to that used in the integrated cross section tests. (Figure 5–14.) After the smearing, the distributions in y for V−A and for V+A were quite similar, so it was not possible to discern which was the better fit to the data. This similarity did, however, make it possible to come up with an unbiased estimate of the total number of inverse muon decay events and to compare that to the expected number of events for each hypothesis.

The results of the fits are shown in table 5–6. Linear least-squares fitting in one variable (the percentage of quasielastics) was the method used, minimizing the goodness of fit quantity χ^2. Each of the data distributions was fit by inverse muon signal and quasielastic Monte Carlo distributions generated at the appropriate train setting. The error in the fit variable was determined by the change needed to increase χ^2 by one. The V−A theory was favored over pure V+A by a factor of 3.6 by likelihood ratio.

5D. Limits placed on non-V−A parameters.

The conventional model of pure V−A interaction is favored by the results of both of the integrated cross section tests and by the differential cross section test. If we combine two independent likelihood ratios we get betting odds of 25 (Q^2 test with y test) and 21 ($E\theta^2$ with y). In this section, we will look at models more general than the pure V−A and pure V+A models and set limits on possible couplings.

5D.1. The P and λ parameters.

Figure 5–15a is reproduced from the most recent results for the wide-

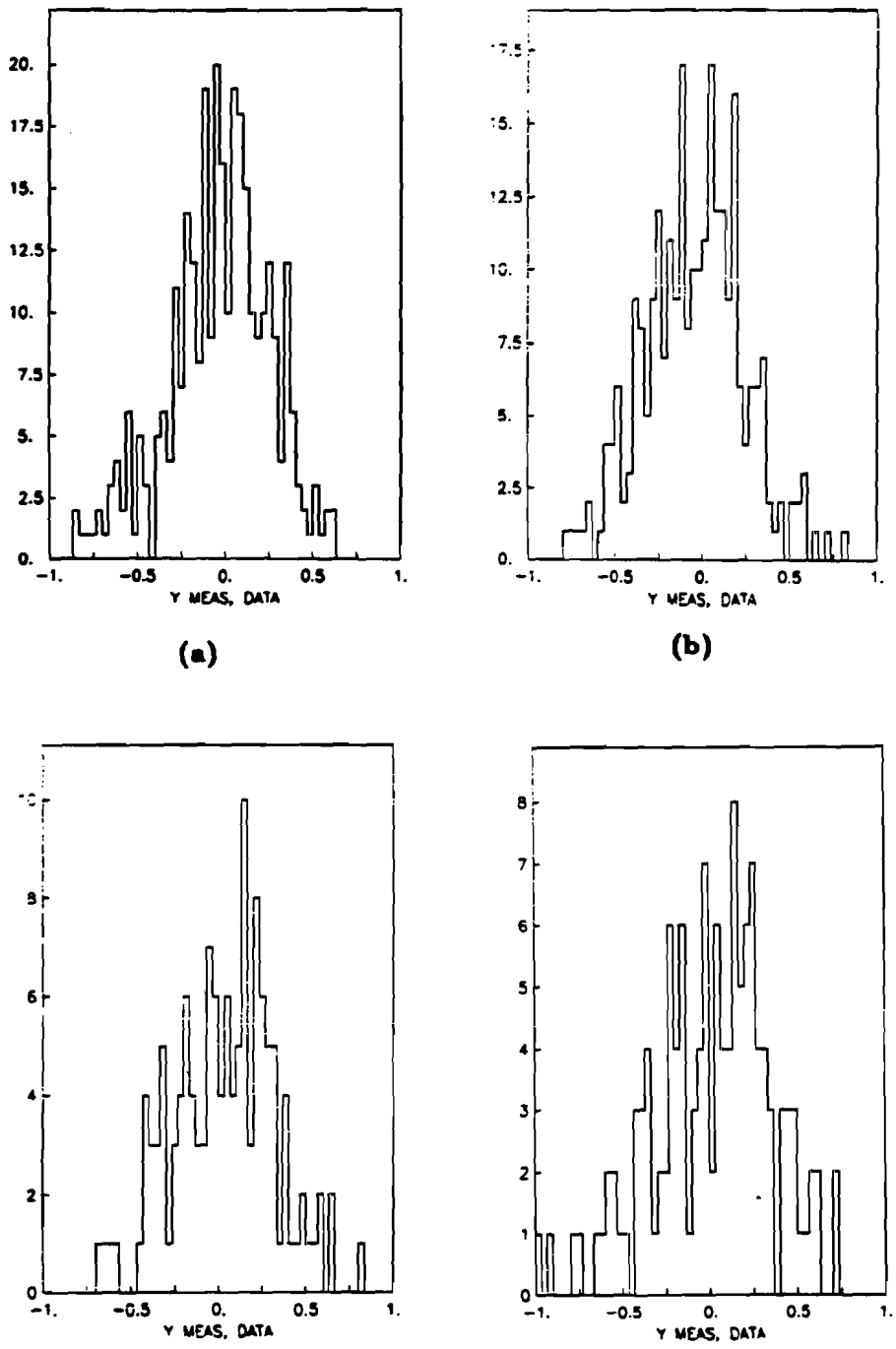

Figure 5–12. y **distributions**
(a) -165, (b) +165, (c) +200, (d) +250 GeV/c

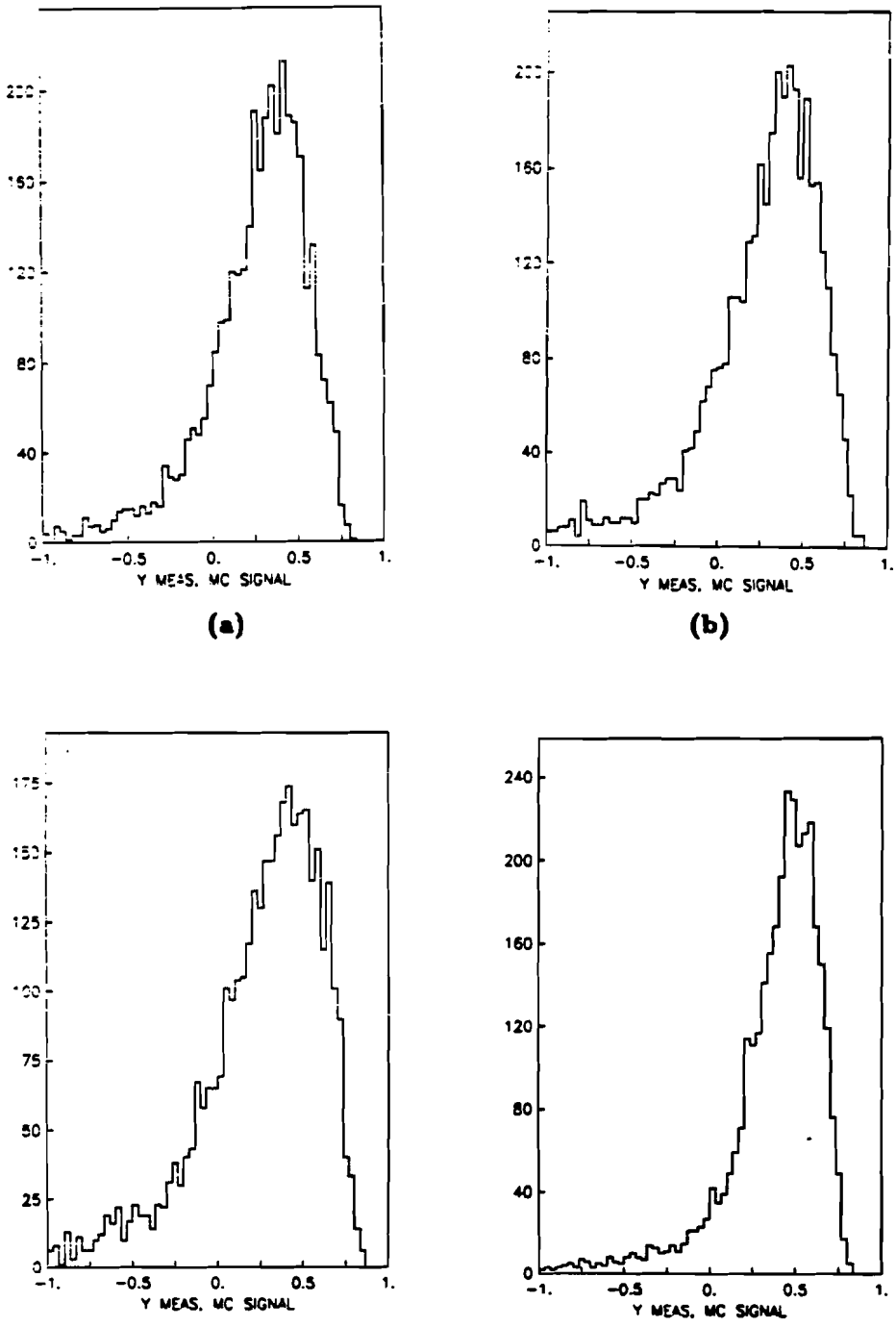

Figure 5–18. Monte Carlo signal y distributions: (a) +165, (b) +200, (c) +250 (all V−A), (d) +165 (V+A)

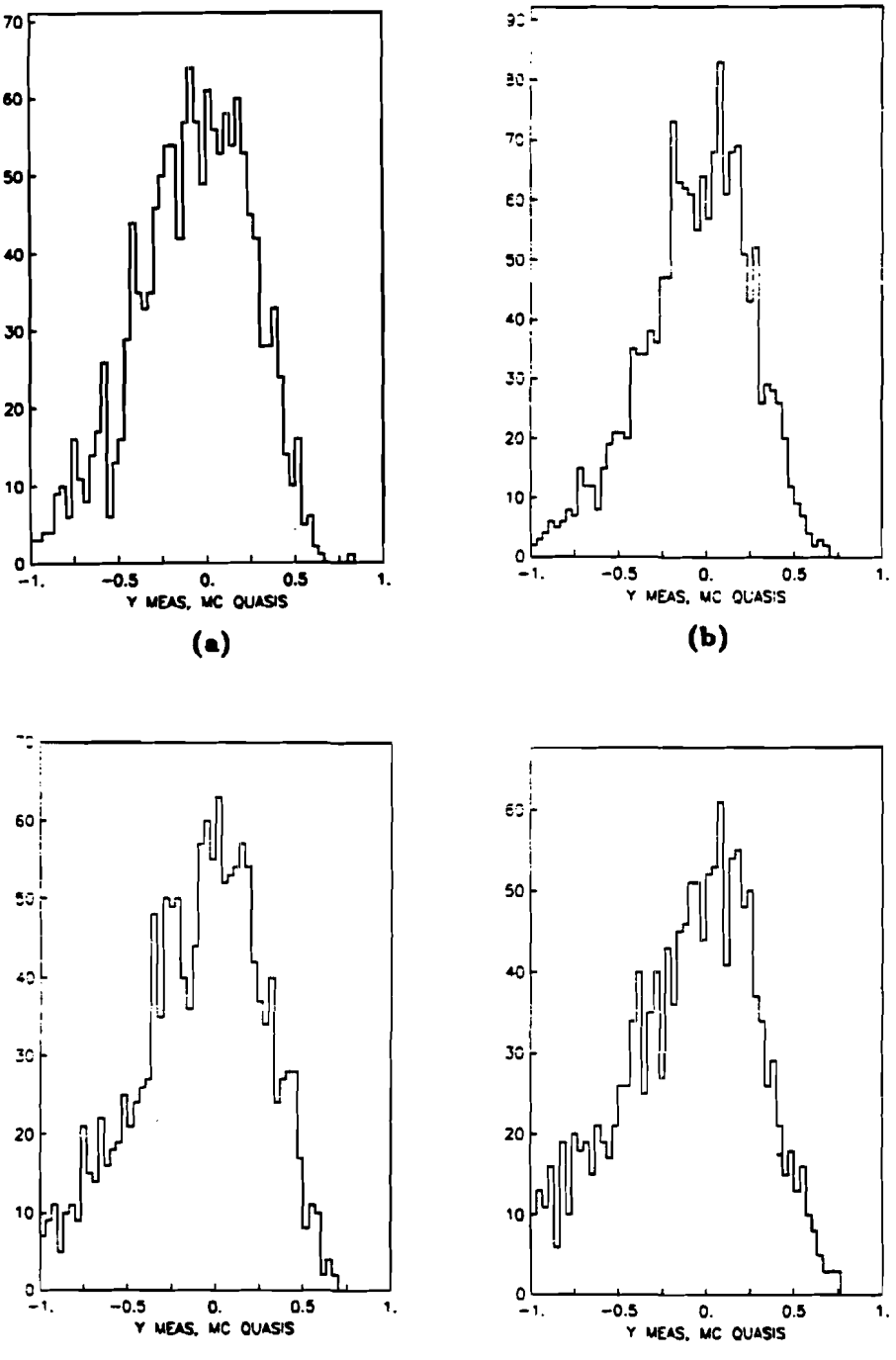

Figure 5-13. Monte Carlo quasielastic y distributions: (e) -165, (f) +165, (g) +200, (h) +250.

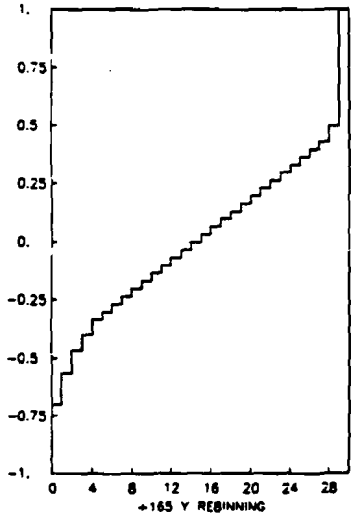

(a)

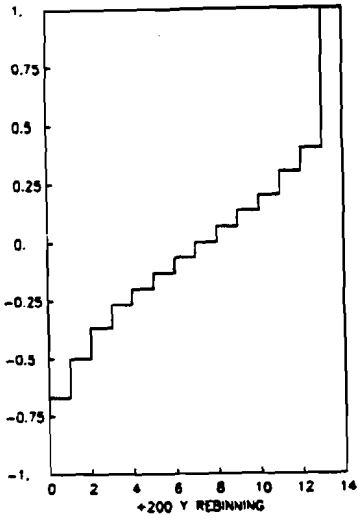

(b)

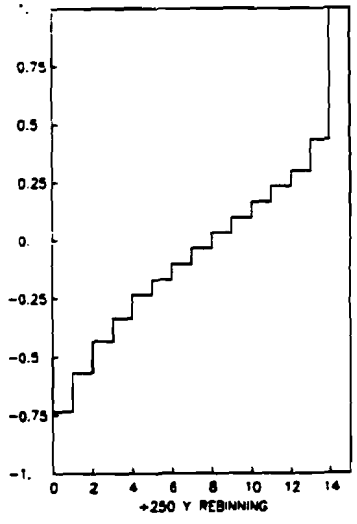

(c)

Figure 5–14. Rebinning scheme in y.
(a) +165, (b) +200, (c) +250

Table 5–6. Fits to y distributions.

Train setting	Observed	V−A Expected	V+A Expected
+165	9.8±8.8	10.0	3.4
+200	15.1±11.6	5.8	2.0
+250	19.9±10.8	8.5	2.8
All positives	43.9±18.1	24.3	8.2

Likelihood ratio for V−A vs. V+A : 3.6

band beam study of the inverse muon decay reaction.[6] It depicts the 90% confidence level limits on P and λ for the Gargamelle and CHARM detector experiments. Figure 5–15b gives the same plot for this experiment using the results of the tests described in the preceeding two sections of this thesis. For each train setting, the ratio $S = \mathrm{N}_{obs}/\mathrm{N}_{exp}^{\mathbf{V-A}}$ was formed. The measurements of S from the Q^2 test are independent for different train settings up to the common dependence on the −165 data distribution and on the −165 Monte Carlo quasielastic distribution for the nuclear corrections. Also, this test and the y distribution test did rely on a common set of assumptions that went into the formulation of the Monte Carlo simulations for inverse muon decays and for quasielastic scattering events. The errors on S were computed by combining the statistical errors with those imposed by limitations in estimating the total number of neutrinos (5% error in normalization),[7] the fiducial mass (3% error in the number of electrons),[8] and the various acceptances denoted by η_1, η_2, η_3 above (binomial error). When the errors were added in quadrature, the statistical errors clearly dominated.

When we combined the different measurements of S, treating them as independent measurements, we found $S = 1.00 \pm 0.28$ for the best fit and 1σ limit. Due to the rather small sample of inverse muon decay events in this experiment ($\approx$ 20 versus 600 for the CHARM experiment) the limits were much less restrictive. To the level of accuracy attainable by this technique,

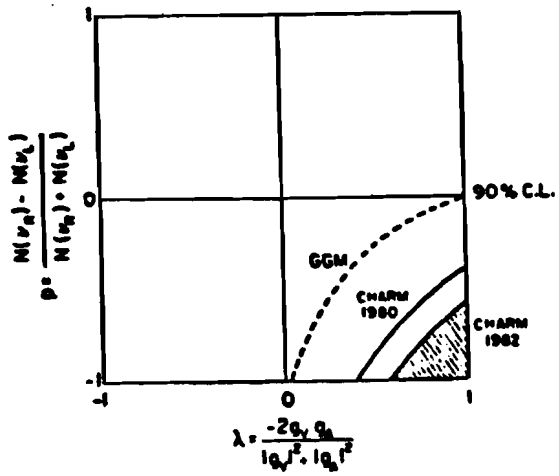

(a)

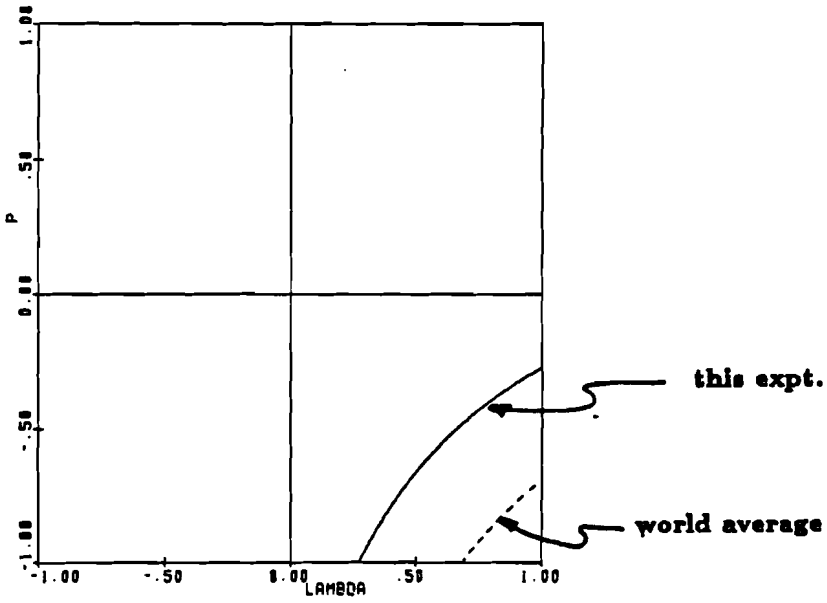

(b)

Figure 5–15. 90% confidence limits on non-V−A parameters P and λ: (a) for Gargamelle and CHARM, (Ref. 6) (b) for this experiment

however, it is clear that our results are in agreement with previous ones and with the pure V−A theory as well. The dotted contour in figure 5–15b shows the result obtained by combining the value for S from the CHARM experiment ($S = 0.98 \pm 0.12$) with the value from this experiment:

$$S = 0.982 \pm 0.110 \tag{5.6}$$

Both of these contours were obtained from the one-sided 90% confidence interval for the normal distribution: $(-1.96\sigma < S - \langle S \rangle < \infty)$. This will tend to underestimate the errors on P and on λ if $\langle S \rangle$ is greater than one, but we have chosen this method in order to be consistent with previous plots of the limits on these parameters.

5D.2. Limits on the general V, A parameters.

Table 5–7a sets out the limits imposed on the angular parameters for the fermion-mirror fermion mixing models of Maalampi *et al.*[1] by a least squares fit to the most recent results to the various tests described in Chapter 3. The dependence on the cross section of inverse muon decay is described in Appendix B. The value of S used was the world average (equation 5.6). The new values of S and $\sigma(S)$ left the values of the parameters of these models virtually unchanged (compare to table 3–2a). The contributions to χ^2 by the experimental constraints used are listed by size (for model "c") in table 5–8 to indicate how the fits were more influenced by constraints other than the inverse muon decay cross section.

Table 5–7b gives the results for the left-right symmetric model in the same format as table 3–2b. Here the revised value for S had no effect on the best fit for the model parameters or on the errors. Figure 5–16 shows the 68.5% confidence limit region (outer contours) and best fit (inner) contours in parameter space, using the old value of S, the value obtained by this

Table 5–7a
Results to fits for fermion–mirror fermion models
(world average value for S)
Best fits and 68.3% C.L. values

Model	θ_e	θ_{emax}	ϕ_e	ϕ_{emax}	θ_μ	$\theta_{\mu max}$	ϕ_μ	$\phi_{\mu max}$	$\sin^2\theta_W$	χ^2/d.f.
a_{coh}	1.1	2.1†	8.0	15.7	0.0	2.3	8.9	13.6	0.249	9.5/18
a_{inc}	free*	free	5.5	15.0	free	free	7.6	12.1	0.246	10.0/18
b_{coh}	1.1	1.9	16.0	25.0	0.0	3.8	0.0	44.9†	0.240	10.2/16
b_{inc}	free	free	15.9	24.9	free	free	0.0	4.7	0.240	10.6/18
c	5.0	13.3	14.0	18.8	2.5	9.2	13.9	18.2	0.221	8.3/16
d_{coh}	0.1	43.6†	4.4	7.1	0.0	1.6	9.0	13.7	0.249	9.8/16
d_{inc}	free	free	4.3	7.0	free	free	7.8	12.1	0.246	10.0/18

*Unconstrained parameter
†Parabolic error estimate
All values in degrees. Pure V−A gives zero for all mixing angles.

Table 5–7b
Results to fit for the left-right symmetric model
(world average value for S)

Quantity	Fit value	68.3% C.L.
m_{W_L}/m_{W_R}	0.14	0.18
ω	0.0°	1.9°

$\chi^2 = 3.0$ for 5 degrees of freedom.
Pure V−A value is zero for each parameter.

Table 5–8. Contributions to χ^2 from each experimental constraint.

Model c		Left-right	
Constraint	χ^2	Constraint	χ^2
$P_\mu \xi$	2.31	$P_\mu \xi$	2.46
R_p	1.37	ρ	0.75
A^{FB}	0.99	S	0.19
a_2	0.68	P_β^{GT}	0.05
a_1	0.68	h	0.03
ρ	0.66	$P_\mu \xi \delta / \rho$	0.02
$\langle \sigma(\nu_e e) \rangle$	0.61	P_μ	0.004
$\sigma(\nu_\mu e)/E_\nu$	0.25		
δ	0.21		
R_n	0.21		
$\sigma(\bar{\nu}_\mu e)/E_\nu$	0.20		
S	0.19		
h	0.08		
$P_\mu \xi \delta / \rho$	0.06		
$\sigma(\nu_\mu e)/\sigma(\bar{\nu}_\mu e)$	0.03		
h_{VV}	0.02		
B	0.01		
r^+	0.006		
r^-	0.002		
P_μ	0.002		
R_π	0.00003		

experiment, and the world average. The contributions to χ^2 by the various experimental constraints are ranked in table 5–8.

If we use only the weighted mean value for S obtained by the two tests in this thesis, ignoring all of the wide-band data, we obtain the limits given in table 5–9. For most of the parameters of the various fermion–mirror fermion models, there was only a modest increase in the upper limits and virtually no change in the best fit values, indicating that the main constraints were those imposed by experimental uncertainties in other tests of the V−A theory.

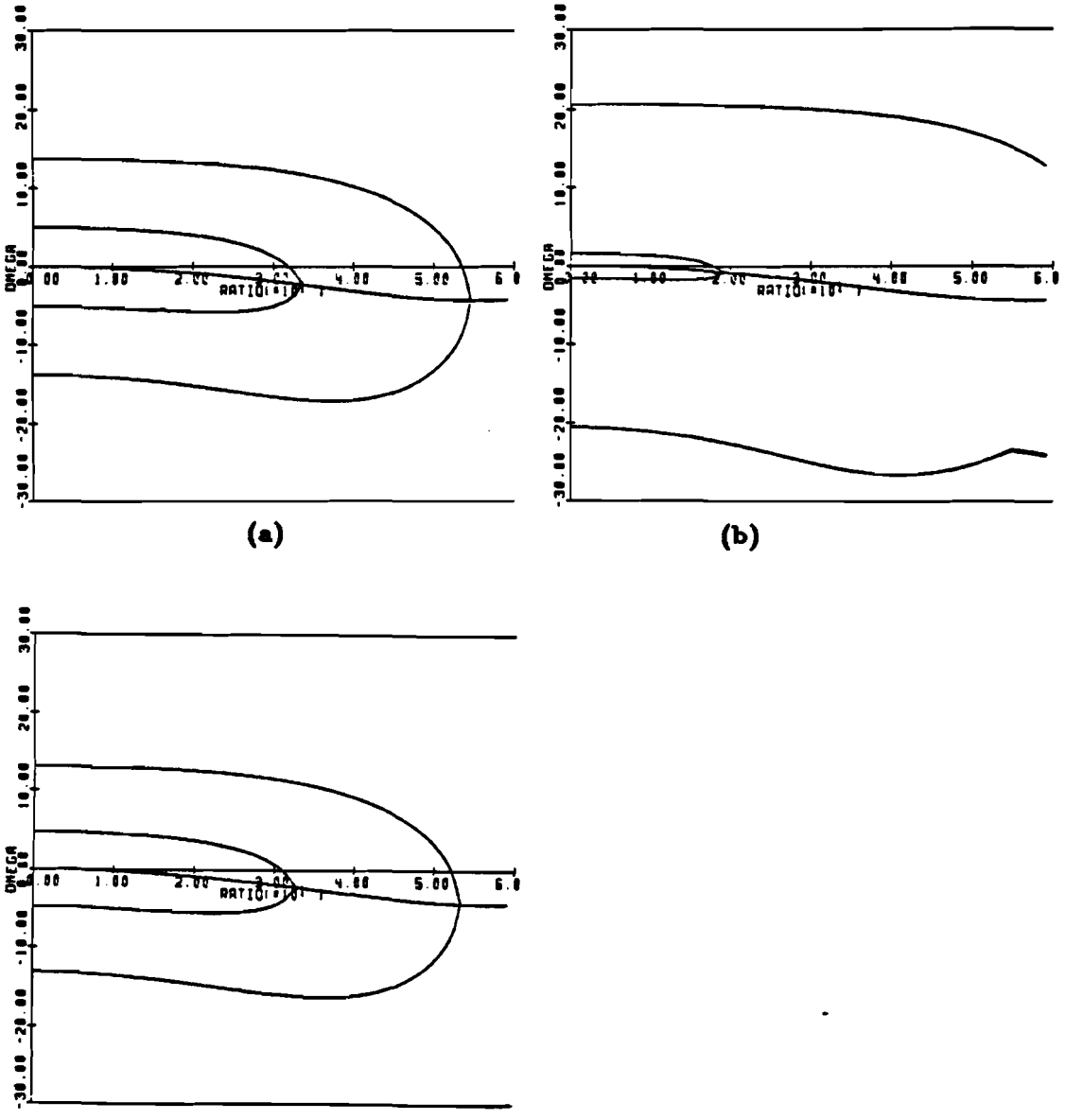

(a) (b)

(c)

Figure 5–16. 68.5% confidence limits on left-right symmetric model parameters mass ratio m_{W_L}/m_{W_R} and mixing angle ω.
(a) previous limits ($S = 0.98 \pm 0.12$) (b) this experiment ($S = 1.00 \pm 0.28$)
(c) combined value $S = 0.98 \pm 0.11$

Table 5–9a
Results to fits for fermion–mirror fermion models
(value for S from this experiment)
Best fits and 68.3% C.L. values

Model	θ_e	θ_{emax}	ϕ_e	ϕ_{emax}	θ_μ	$\theta_{\mu max}$	ϕ_μ	$\phi_{\mu max}$	$\sin^2\theta_W$	χ^2/d.f.
a_{coh}	1.1	2.0	12.0	21.8	0.0	2.3	8.8	13.5	0.249	9.4/18
a_{inc}	free*	free	13.7	23.3	free	free	8.5	12.9	0.248	9.7/18
b_{coh}	1.1	1.9	16.0	25.0	0.0	3.8	0.0	45.0†	0.240	10.2/16
b_{inc}	free	free	15.9	25.0	free	free	0.0	4.7	0.240	10.5/18
c	5.0	16.8	13.9	18.8	2.4	9.2	13.9	14.3	0.221	8.2/16
d_{coh}	0.4	42.8†	4.4	7.1	0.0	1.6	9.0	13.7	0.249	9.8/16
d_{inc}	free	free	4.4	7.1	free	free	8.3	12.8	0.247	10.3/18

*Unconstrained parameter
†Parabolic error estimate
All values in degrees. Pure V−A gives zero for all mixing angles.

Table 5–9b
Results to fit for the left-right symmetric model
(value for S from this experiment)

Quantity	Fit value	68.3% C.L.
m_{W_L}/m_{W_R}	0.14	0.18
ω	0.0°	1.9°

$\chi^2 = 3.0$ for 5 degrees of freedom.
Pure V−A value is zero for each parameter.

CHAPTER VI. CONCLUSIONS

This concluding chapter will critique the studies of the inverse muon decay that have been conducted to date, including the present experiment. A few questions concerning the significance and reliability of the experimental method used will be addressed.

The Gargamelle experiment[1] obtained the $E_\mu \theta_\mu^2 / 2m_e$ distribution shown in figure 6–1. In this illustration, the background shape was measured by a run taken with neutrinos at the CERN-PS below the threshold of inverse muon decay. To apply this to the SPS run at energies over threshold, the transverse muon momentum P_T was assumed not to vary with neutrino energy, and the parallel component of momentum was assumed to scale with energy. The normalization of the background component was computed in two ways. One was by comparing the number of events with $P_T > 160\,\mathrm{MeV/c}$ for the PS run to that for the SPS run, and extrapolating to the range $P_T < 160$ MeV/c. The other was by means of a likelihood fit to the joint distribution in E_μ and θ_μ^2 using theoretical densities for signal, quasielastic scattering from nucleons, and quasielastic scattering from nuclei. The two determinations of the relative normalization were in good agreement.

The advantage of using the low energy data to identify the quasielastic component of the SPS results was that the nuclear effects must have been the same for the two. The difference in the scanning efficiency was measured and incorporated into the extrapolation.

The CHARM experiment[2] used much the same method for detecting the

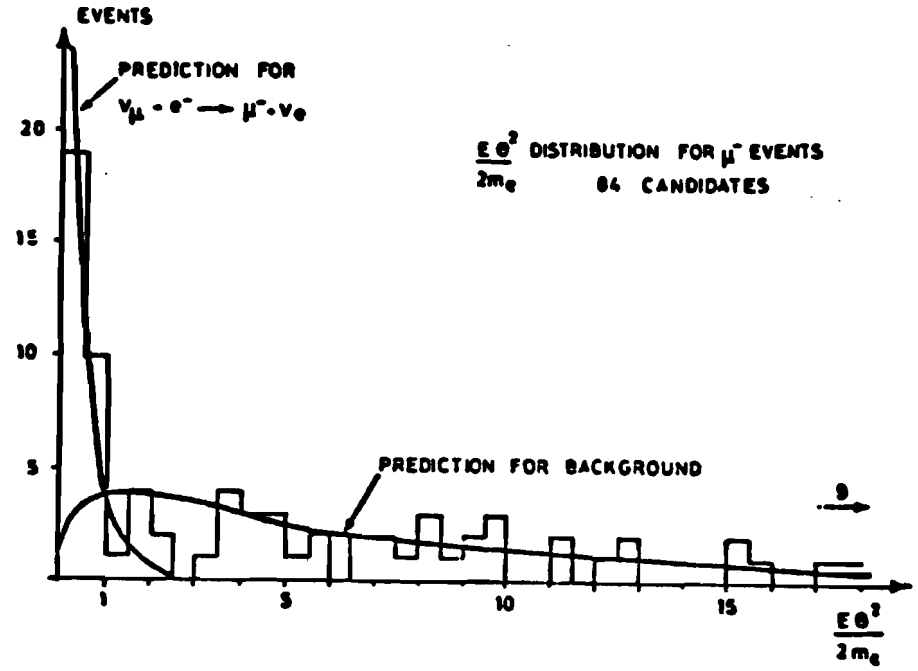

Figure 6–1. Gargamelle $E\theta^2/2m_e$ distribution. (Ref. 1)

inverse muon decays in the Q^2 distribution as the present experiment (figure 6–2) except that because of the increased neutrino yield and live time in the wide-band beam it was able to bin more finely in the low-Q^2 region. The cuts on the data relied mainly on scintillator pulse height response to measure the amount of deposited energy near the vertex, which had sufficiently fine resolution to distinguish one charged track from a number of charged tracks. The region in Q^2 above 0.1 GeV^2 was neglected due to the difference in recoilless neutrino and antineutrino acceptance there. No nuclear correction was made to eliminate the difference in the amount of Pauli suppression for neutrinos and antineutrinos. The lack of such a correction would tend to bias the results toward the V−A theory because of the dip in the antineutrino spectrum which is not the same as the one in the neutrino spectrum (compare figure 5–4*a* to figures 5–4*b* through *d* as well as figure 2–1).

Data from the present experiment are displayed in the variables Q^2 in figure 5–4 and in $E\theta^2$ in figure 5–8. In the present experiment, due to the

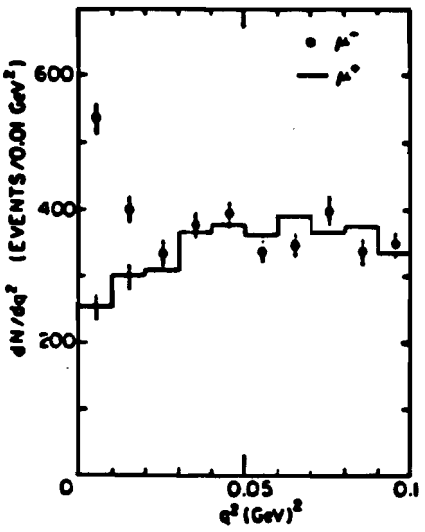

Figure 6–2. CHARM Q^2 distributions

limited number of events, the normalization of the Q^2 distributions was over a wider range, but the energy deposition cut was purposely left fairly loose so as not to reject proton recoils from true quasielastics. Preliminary studies using the proton recoil tracking package to discriminate against events that had a clear recoil strongly affected the result of subtracting the normalized distributions, resulting in a much larger number of inverse muon decay events than expected. To help show that something similar has not also happened with the present set of filter cuts, the Monte Carlo neutrino and antineutrino quasielastic spectra were subjected to the same analysis as the data. No low-Q^2 excess was found. A complementary analysis of the neutrino data, subtracting the Monte Carlo quasielastic distribution for either neutrinos or antineutrinos, yielded consistent results with the subtraction of the antineutrino data. These are not compelling arguments as to the appropriateness of the cuts, because of the limitations of the simulation used (which did not take into account such effects as scattering off of entire nuclei, inelastic scattering, nuclear shell and spin effects in quasielastic scattering, or noise hit correlation in the calorimeter), but they do illustrate both the sensitivity of

the technique to differences between the data and the overall consistency of the results.

Along the same lines, the consistency check provided by the differential cross section test was interesting. This test did not depend at all on the form of the nuclear corrections to the Q^2 distribution, but gave answers which agreed very well with the other tests. When the -165 data were fit to the quasielastic scattering and inverse muon decay distributions in the same manner as the positive train setting data, a null result for the excess ($N < 18.5$ out of 311 total events, best fit $N = 6.4$) was observed at the 1σ confidence level. This agreed with the additive conservation of lepton number. In contrast, each of the positive train settings yielded best fit values at least 1σ away from zero.

As for the theoretical analysis of the result, it must be pointed out here how important it is to use approximations only in their appropriate range of validity. As pointed out in more detail in Appendix A, the approximation used by the CHARM experiment in deriving their expression for the differential cross section $\frac{d\sigma}{dy}$ held only in the limit $s \gg m_\mu^2 = 0.011$ GeV^2. This kinematic range cannot adequately represent the wide-band beam exposure in the CERN-SPS (figure 3–1) which peaked at $E_\nu = 20$ GeV, corresponding to $s = 0.02$ GeV^2. The effect is to make the expected number of events for pure V$-$A greater than the correct value and for pure V+A smaller than the correct value. Of course, with a cross section linearly dependent on s, the effect of misrepresenting the part of the neutrino spectrum just above the threshold energy (where the approximation is furthest from true) is less significant than a similar error over all energies would be.

The limits on non-V$-$A couplings in the fermion-mirror fermion and left-right symmetric models[3] were still valid because the derivation of the

dependence on the inverse muon decay cross section did not use this approximation. One feature of this derivation which remains obscure was the origin of the integration constant c which depended on the nature of the neutrino energy spectrum. In analyzing the present data, it has not been altered from its assigned value of 0.375, even though the neutrino spectrum was quite different in most respects from that of the CERN-SPS beam.

In the future, when more precise measurements of such quantities as the decay asymmetry ξ in direct muon decay will have been made, the inverse muon decay cross section will be more significant in setting the best limits on non-V−A couplings in the weak interactions. Limits on scalar, pseudoscalar, and tensor couplings may be revised, in principle, in a fashion similar to that of reference 3, although such a study was beyond the scope of the present paper. Finally, in the higher range of s that will be available to the new generation of accelerators, given sufficiently good statistics and sufficiently good muon momentum resolution, the present analysis may well be extended to future experiments in dichromatic neutrino beams. Depending on the way in which any deviations from the usual V−A theory might arise, the extension of this study to a higher center of mass energy range may make certain departures from the usual V−A theory more prominent (e.g., due to finite mass for the right-handed gauge boson in the left-right symmetric model). The present level of knowledge concerning this topic is such that there is still room for significant and physically relevant effects, whether due to grand unification theories or for some other reason, to be observed experimentally.

APPENDIX A: DERIVATION OF CROSS SECTION $\frac{d\sigma}{dy}$

The derivation of the cross section for the inverse muon decay $\nu_\mu + e^- \rightarrow \mu^- + \nu_e$ is given here in detail as a convenience for the reader to make sense of a subject in disarray. The earliest treatment of the reaction[1] gave a formula for the Hamiltonian that contained serious errors. Other references[2,3] give identical formulae for cross sections $\frac{d\sigma}{d\cos\theta}$ but define the same parameters differently. Owing to the confusion over whether the approximation $s \pm m_\mu^2 \approx s$ can be taken, one of these references[3] has given an inaccurate formula for $\frac{d\sigma}{dy}$. None of the references delve into the details of the Dirac algebra. Understanding the theoretical parameters, however, can come only from seeing how the parameters derive from first principles.

The most general Hamiltonian density for this reaction containing only V and A couplings is:

$$\mathcal{H} = \tfrac{1}{\sqrt{2}}\bar{e}\gamma_\lambda(1-\gamma_5)\mu \cdot \bar{\nu}_\mu\gamma^\lambda(g_V + g_A\gamma_5)\nu_e. \qquad (A.1)$$

where g_V and g_A are the vector and axial vector complex coupling constants and ν_μ, e, μ, and ν_e are spinors corresponding to each of the fermions. (This is in "charge retention" ordering; it is related to "charge changing" ordering $\sum_i \bar{\mu}(g_i + g_i'\gamma_5)O_i\nu_\mu \cdot \bar{\nu}_e O_i e$, which is familiar from the application of elementary Feynman rules, by a Fierz transformation.[4] This transformation would introduce couplings $i = S, P, A, V$.) The square of the matrix element is

given by

$$
\begin{aligned}
|\mathcal{M}|^2 =& \frac{1}{2M_W^2}\left[\bar{e}\gamma_\lambda(1-\gamma_5)\mu\bar{\mu}\gamma_\sigma(1-\gamma_5)e\right] \\
& \cdot\left[\bar{\nu}_\mu\gamma^\lambda(g_V+g_A\gamma_5)\nu_e\bar{\nu}_e\gamma^\sigma(g_V^*+g_A^*\gamma_5)\nu_\mu\right] \\
=& \frac{1}{2M_W^2}T_1T_2
\end{aligned}
\tag{A.2}
$$

where the mass of the intermediate vector boson M_W is included to approximate the full propagator, at the low center of mass energies typical of this reaction. We can rewrite these factors in terms of traces:

$$
\begin{aligned}
T_1 =& \tfrac{1}{4}Tr\left[(\not{p}_e+m_e)(1+\gamma_5\not{s}_e)\gamma_\lambda(1-\gamma_5)(\not{p}_\mu+m_\mu)(1+\gamma_5\not{s}_\mu)\gamma_\sigma(1-\gamma_5)\right] \\
T_2 =& Tr\left[\not{p}_1(1-P\gamma_5)\gamma^\lambda(g_V+g_A\gamma_5)\not{p}_2\gamma^\sigma(g_V^*+g_A^*\gamma_5)\right]
\end{aligned}
\tag{A.3}
$$

where we have denoted the polarization vectors of the electron and of the muon by s_e and s_μ, the four-momenta of ν_μ and ν_e by p_1 and p_2, and the initial neutrino beam polarization by $P \equiv \dfrac{N(\nu_R)-N(\nu_L)}{N(\nu_R)+N(\nu_L)}$. Using the identities

$$
\begin{aligned}
\gamma_5(1-P\gamma_5)\gamma_\mu =& -\gamma_\mu(P+\gamma_5) \\
(1-\gamma_5)^2 =& 2(1-\gamma_5) \\
(1-\gamma_5)(1+\gamma_5) =& 0 \\
Tr(\text{odd number of } \gamma_\mu) =& 0
\end{aligned}
\tag{A.4}
$$

we have

$$
\begin{aligned}
T_1 =& \tfrac{1}{4}Tr\left[(\not{p}_e+m_e)(1-\not{s}_e)\gamma_\lambda(1-\gamma_5)(\not{p}_\mu+m_\mu)(1-\not{s}_\mu)\gamma_\sigma(1-\gamma_5)\right] \\
=& \tfrac{1}{4}Tr\Big[(\not{p}_e+m_e)(1-\not{s}_e)\gamma_\lambda\Big((\not{p}_\mu+m_\mu\not{s}_\mu)\gamma_\sigma(1-\gamma_5)^2 \\
& +(m_\mu-\not{p}_\mu\not{s}_\mu)\gamma_\sigma(1+\gamma_5)(1-\gamma_5)\Big)\Big] \\
=& \tfrac{1}{2}Tr\left[(\not{p}_e-m_e\not{s}_e)\gamma_\lambda(\not{p}_\mu-m_\mu\not{s}_\mu)\gamma_\sigma(1-\gamma_5)\right]
\end{aligned}
\tag{A.5}
$$

$$T_2 = Tr\left[\not{p}_1\gamma^\lambda\not{p}_2\gamma^\sigma\left((|g_V|^2+|g_A|^2)+(g_V g_A^*+g_A g_V^*)\gamma_5\right)(1+P\gamma_5)\right]$$
$$=(|g_V|^2+|g_A|^2)\,Tr\left[\not{p}_1\gamma^\lambda\not{p}_2\gamma^\sigma(1-\lambda\gamma_5)(1+P\gamma_5)\right]$$
$$=8M_W^2G_F^2\,Tr\left[\not{p}_1\gamma^\lambda\not{p}_2\gamma^\sigma((1-\lambda P)-(\lambda-P)\gamma_5)\right] \qquad (A.6)$$

where

$$\lambda = \frac{-2\,Re(g_V g_A^*)}{|g_V|^2+|g_A|^2}$$
$$\text{and} \qquad (A.7)$$
$$G_F^2 = \frac{|g_V|^2+|g_A|^2}{8M_W^2}$$

is the Fermi coupling constant. Reference 2 seems to disagree with both this derivation and the formula in reference 3 on the sign of the parameter λ. We can now use the identity[5]

$$Tr\left[\gamma_\alpha\gamma_\sigma\gamma_\beta\gamma_\tau(a-b\gamma_5)\right]Tr\left[\gamma^\nu\gamma^\sigma\gamma^\mu\gamma^\tau(c-d\gamma_5)\right]$$
$$= 32ac\left[g_\alpha^\nu g_\beta^\mu + g_\alpha^\mu g_\beta^\nu\right] + 32bd\left[g_\alpha^\nu g_\beta^\mu - g_\alpha^\mu g_\beta^\nu\right] \qquad (A.8)$$

to get

$$|M|^2 = 4G_F^2\Big[32(\tfrac{1}{2})(1-\lambda P)\big((p_e+m_e s_e)\cdot p_1\,(p_\mu+m_\mu s_\mu)\cdot p_2$$
$$+(p_e+m_e s_e)\cdot p_2\,(p_\mu+m_\mu s_\mu)\cdot p_1\big)$$
$$+32(\tfrac{1}{2})(\lambda-P)\big((p_e+m_e s_e)\cdot p_1\,(p_\mu+m_\mu s_\mu)\cdot p_2$$
$$-(p_e+m_e s_e)\cdot p_2\,(p_\mu+m_\mu s_\mu)\cdot p_1\big)\Big] \quad . \qquad (A.9)$$

All the charged lepton polarization factors drop out when we average over s_e (picking up a factor of $1/2$) and sum over s_μ. The Mandelstam variables may now be incorporated:

$$s = (p_e+p_1)^2 = m_e^2+2p_e\cdot p_1$$
$$= (p_\mu+p_2)^2 = m_\mu^2+2p_\mu\cdot p_2$$
$$t = (p_1-p_\mu)^2 = m_\mu^2-2p_1\cdot p_\mu$$
$$= (p_e-p_2)^2 = m_e^2-2p_e\cdot p_2 \qquad (A.10)$$

$$|\mathcal{M}|^2 = 8G_F^2\Big[(1-\lambda P)\Big((s-m_e^2)(s-m_\mu^2)+(t-m_e^2)(t-m_\mu^2)\Big)$$
$$+(\lambda-P)\Big((s-m_e^2)(s-m_\mu^2)-(t-m_e^2)(t-m_\mu^2)\Big)\Big] \quad (A.11)$$

If we now neglect m_e^2 with respect to s, but keep m_μ^2,

$$|\mathcal{M}|^2 = 8G_F^2\Big[(1-\lambda P+\lambda-P)s(s-m_\mu^2)$$
$$+(1-\lambda P-\lambda+P)t(t-m_\mu^2)\Big]. \quad (A.12)$$

In the center of momentum system,

$$E_1 = \frac{s-m_e^2}{2\sqrt{s}} = p_1$$
$$E_\mu = \frac{s+m_\mu^2}{2\sqrt{s}}$$
$$p_\mu = \frac{s-m_\mu^2}{2\sqrt{s}}$$

$$t = m_\mu^2 - E_1E_\mu + 2p_1p_\mu\cos\theta$$
$$= \frac{1}{2s}\Big[2m_\mu^2 s - s^2 + m_e^2 s - m_\mu^2 s - m_e^2 m_\mu^2$$
$$+(s-m_e^2)(s-m_\mu^2)\cos\theta\Big]$$
$$= \frac{1}{2s}(s-m_e^2)(s-m_\mu^2)(1-\cos\theta)$$
$$\approx \frac{1}{2}(s-m_\mu^2)(1-\cos\theta) \quad (A.13)$$

where θ is the angle between the muon direction and the incoming neutrino direction.

$$|\mathcal{M}|^2 = 8G_F^2 s(s-m_\mu^2)\Big[(1+\lambda)(1-P)$$
$$+\frac{1}{4}(1-\lambda)(1+P)\big((1-\tfrac{m_\mu^2}{s})(1-\cos\theta)+2m_\mu^2\big)$$
$$(1-\cos\theta)\Big] \quad (A.14)$$

$$\frac{d\sigma}{d\cos\theta} = \frac{1}{8s^2}\frac{(s-m_e^2)(s-m_\mu^2)}{4\pi s}|\mathcal{M}|^2$$
$$= \frac{G_F^2}{16\pi s}(s-m_\mu^2)\Bigg\{4(1+\lambda)(1-P)$$
$$+ (1-\lambda)(1+P)\left[1+\frac{m_\mu^2}{s}-\left(1-\frac{m_\mu^2}{s}\right)\cos\theta\right]$$
$$\times(1-\cos\theta)\Bigg\} \qquad (A.15)$$

This formula agrees with the formulae given by both reference 3 and reference 2.

To arrive at the differential cross section $\frac{d\sigma}{dy}$, we first need to set up the kinematics in the center of momentum frame. Let the four-momentum transfer be given by $q \equiv p_1 - p_\mu$ and let the unit 3-vectors $\vec{\mathbf{x}}$ and $\vec{\mathbf{x}}'$ be in the direction of the neutrino and of the muon respectively. If we start out by leaving in all the charged lepton mass terms, we have

$$\begin{aligned} p_e: &\quad \tfrac{1}{2\sqrt{s}}\left(2m_e^2+2E_\nu m_e\ ,\ -2E_\nu m_e\vec{\mathbf{x}}\right)\\ q: &\quad \tfrac{1}{2\sqrt{s}}\left(-m_e^2-m_\mu^2\ ,\ (2E_\nu m_e)\vec{\mathbf{x}}-(m_e^2-m_\mu^2+2E_\nu m_e)\vec{\mathbf{x}}'\right)\\ p_1: &\quad \tfrac{1}{2\sqrt{s}}\left(2E_\nu m_e\ ,\ 2E_\nu m_e\vec{\mathbf{x}}\right) \qquad (A.16)\end{aligned}$$

Since $\cos\theta = \vec{\mathbf{x}}\cdot\vec{\mathbf{x}}'$ we have

$$p_e\cdot q = \frac{m_e}{2s}\Big[2E_\nu^2 m_e(1-\cos\theta) - E_\nu m_e^2(1+\cos\theta)$$
$$- E_\nu m_\mu^2(1-\cos\theta) - m_e^3 - m_e m_\mu^2\Big]$$
$$= \frac{m_e}{2s}\Big[E_\nu(2E_\nu m_e - m_\mu^2)(1-\cos\theta)$$
$$- E_\nu m_e^2(1+\cos\theta) - m_e^3 - m_e m_\mu^2\Big]$$
$$p_e\cdot p_1 = \frac{1}{4s}\left[4E_\nu^2 m_e^3 + 4E_\nu^2 m_e^2 + 4E_\nu^2 m_e^2\right]$$

$$= \frac{m_e}{2s} \left[2E_\nu m_e (2E_\nu + m_e) \right] \qquad (A.17)$$

We can neglect the terms m_e^3, $m_e m_\mu^2$, and $E_\nu m_e^2(1+\cos\theta)$ with respect to the first term in the equation for $p_e \cdot q$, each of which is down by at least six orders of magnitude, and also neglect m_e with respect to E_ν in the equation for $p_e \cdot p_1$. Then, since the inelasticity $y \equiv p_e \cdot q \, p_e \cdot p_1$ we have

$$\begin{aligned} y &= \left(\frac{1}{2} - \frac{m_\mu^2}{4 m_e E_\nu} \right) (1 - \cos\theta) \\ &= \frac{1}{2} \left(\frac{1}{2} - \frac{m_\mu^2}{s} \right) (1 - \cos\theta) \end{aligned} \qquad (A.18)$$

We apply the chain rule and substitute for $(1-\cos\theta)$ in the cross section:

$$\begin{aligned} \frac{d\sigma}{dy} &= \frac{d\sigma}{d\cos\theta} \left(\frac{dy}{d\cos\theta} \right)^{-1} \\ &= \frac{G_F^2}{16\pi s} (s - m_\mu^2) \Big\{ 4(1-P)(1+\lambda) \\ &\qquad + (1+P)(1-\lambda) \frac{2sy}{s - m_\mu^2} \left[s + m_\mu^2 - s + m_\mu^2 + 2sy \right] \Big\} \frac{2s}{s - m_\mu^2} \\ &= \frac{G_F^2}{4\pi} (s - m_\mu^2) \left\{ (1+P)(1-\lambda) y \frac{m_\mu^2 + sy}{s - m_\mu^2} + (1-P)(1+\lambda) \right\}. \end{aligned} \qquad (A.19)$$

A previous experiment[3] takes a further approximation $s \pm m_\mu^2 \approx s$ to get

$$\frac{d\sigma}{dy} \approx \frac{G_F^2}{4\pi} s \left[(1+P)(1-\lambda) y^2 + (1-P)(1-\lambda) \right]. \qquad (A.20)$$

This approximation is not valid in this experiment because for a reasonable neutrino energy of 20 GeV, $s \approx 0.02$ GeV^2, $m_\mu^2 = 0.011$ GeV^2 and the cross section would be wrong by a factor of 2.

APPENDIX B: DETERMINATION OF COUPLINGS FROM THE INVERSE MUON DECAY RATE

This appendix is intended to give more details concerning the predictions for the inverse muon decay rate on the basis of the theories mentioned in section 3C of the text. It is essentially a condensation and reorganization of the material in references 1 and 2.

BA. Fermion–mirror fermion mixing models.

Let us consider first the fermion–mirror fermion mixing model. The charged leptonic current is:

$$J^{\mu} = [\bar{\ell}'\gamma^{\mu}(1-\gamma_5)\nu_{\ell}' + \bar{L}_{\ell}'\gamma^{\mu}(1-\gamma_5)N_{\ell}'] + \text{h.c.} \qquad (B.1)$$

where the conventional leptons are ℓ' and ν_{ℓ}' and the mirror leptons are L_{ℓ}' and N_{ℓ}'. The primes are to distinguish the chirality states from the mass eigenstates:

$$\begin{pmatrix} \ell \\ L_{\ell} \end{pmatrix} = \begin{pmatrix} \cos\theta_{\ell} & -\sin\theta_{\ell} \\ \sin\theta_{\ell} & \cos\theta_{\ell} \end{pmatrix} \begin{pmatrix} \ell' \\ L_{\ell}' \end{pmatrix}$$
$$\begin{pmatrix} \nu_{\ell} \\ N_{\ell} \end{pmatrix} = \begin{pmatrix} \cos\phi_{\ell} & -\sin\phi_{\ell} \\ \sin\phi_{\ell} & \cos\phi_{\ell} \end{pmatrix} \begin{pmatrix} \nu_{\ell}' \\ N_{\ell}' \end{pmatrix} \qquad (B.2)$$

The angles θ_{ℓ} and ϕ_{ℓ} are called mixing angles. We make the definitions

$$\alpha_{\ell} \equiv \frac{2\cos(\theta_{\ell}+\phi_{\ell})\cos(\theta_{\ell}-\phi_{\ell})}{\cos^2(\theta_{\ell}+\phi_{\ell}) + \cos^2(\theta_{\ell}-\phi_{\ell})}$$
$$\tilde{\alpha}_{\ell} \equiv \frac{2\sin(\theta_{\ell}+\phi_{\ell})\sin(\theta_{\ell}-\phi_{\ell})}{\sin^2(\theta_{\ell}+\phi_{\ell}) + \sin^2(\theta_{\ell}-\phi_{\ell})}$$
$$\beta_{\ell} \equiv \cos 2\theta_{\ell} \qquad . \qquad (B.3)$$

The effect of mirror fermion mixing upon the experimental tests that we have chosen will depend on the masses of the mirror leptons. Since charged mirror

leptons lighter than about 20 GeV/c^2 are excluded by present experiments in e^+e^- rings, we need only consider the different mass scales for mirror neutrinos. Ignoring, for our purposes, the third and any higher generations, we have four special cases:

model	$m(N_e)$	$m(N_\mu)$
a	$\ll m_e$	$\ll m_e$
b	$\ll m_e$	$> m_K$
c	$> m_K$	$> m_K$
d	$> m_K$	$\ll m_e$.

With respect to inverse muon decay, two cases of models a, b, and d may be distinguished. If the difference in masses between N_μ and ν_μ is small (less than 1/2 eV) the neutrino beam and mirror neutrino beam will form coherent weak eigenstates by the time it reaches the detector. If one goes to the opposite extreme and assumes that the difference is on the order of 10 eV or so, then the oscillations will average incoherently at the detector. We shall then speak only of the special "coherent" and "incoherent" cases a_{coh}, a_{inc}, b_{coh}, and b_{inc}.

If we let

$$\begin{aligned} \cos(\theta_\ell - \phi_\ell) &= V_\ell, \qquad \sin(\theta_\ell - \phi_\ell) = \tilde{V}_\ell, \\ \cos(\theta_\ell + \phi_\ell) &= A_\ell, \qquad \sin(\theta_\ell + \phi_\ell) = \tilde{A}_\ell \end{aligned} \tag{B.4}$$

then the differential cross section is

$$\begin{aligned} \frac{d\sigma}{dy} = \frac{G_F^2}{16\pi} s \Bigg\{ & (V_e^2 + A_e^2)(V_\mu^2 + A_\mu^2)\left(2 - 2y + y^2 - \frac{m_\mu^2}{s}(2-y)\right) \\ & + 4V_e A_e V_\mu A_\mu \left(2y - y^2 - \frac{m_\mu^2}{s} y\right) \\ & - 2P_{\nu_\mu} \Bigg[\left((V_e^2 + A_e^2) V_\mu A_\mu + (V_\mu^2 + A_\mu^2) V_e A_e \right) \left(1 - \frac{m_\mu^2}{s}\right) \\ & + \left((V_e^2 + A_e^2) V_\mu A_\mu - (V_\mu^2 + A_\mu^2) V_e A_e \right) \\ & \times \left(1 - 2y + y^2 - \frac{m_\mu^2}{s}(1-y)\right) \Bigg] \Bigg\} \end{aligned} \tag{B.5}$$

In experiments testing the integrated cross section, the inelasticity y and the Mandelstam invariant s are averaged over the neutrino energy spectrum. The cross section is then normalized by the pure V−A prediction for the reaction to give a quantity that is called S. So, for the various fermion–mirror fermion models, we have

Model

$$
\begin{aligned}
\mathrm{a_{coh}} \qquad S &= \tfrac{1}{2}\left[(\cos^4\theta_\mu + \sin^4\theta_\mu)(1+c)\right. \\
&\quad \left. + \beta_e(\cos^4\theta_\mu - \sin^4\theta_\mu)(1-c)\right] \\
\mathrm{a_{inc}} \qquad S &= \tfrac{1}{2}(\cos^4\theta_\mu + \sin^4\phi_\mu)\left[(\cos^4\theta_\mu + \sin^4\theta_\mu)(1+c)\right. \\
&\quad \left. + \beta_e(\cos^4\theta_\mu - \sin^4\theta_\mu)(1-c)\right] \\
\mathrm{b} \qquad S &= \tfrac{1}{4}\left[(1+\alpha_\mu^2)(1+c) + 2\beta_e\alpha_\mu(1-c)\right] \\
\mathrm{c} \qquad S &= \tfrac{1}{4}\left[(1+\alpha_\mu^2)(1+c) + 2\alpha_e\alpha_\mu(1-c)\right] \\
\mathrm{d_{coh}} \qquad S &= \tfrac{1}{2}\left[(\cos^4\theta_\mu + \sin^4\theta_\mu)(1+c)\right. \\
&\quad \left. + \alpha_e(\cos^4\theta_\mu - \sin^4\theta_\mu)(1-c)\right] \\
\mathrm{d_{inc}} \qquad S &= \tfrac{1}{2}(\cos^4\phi_\mu + \sin^4\phi_\mu)\left[(\cos^4\theta_\mu + \sin^4\theta_\mu)(1+c)\right. \\
&\quad \left. + \alpha_e(\cos^4\theta_\mu - \sin^4\theta_\mu)(1-c)\right] \qquad (B.6)
\end{aligned}
$$

where c performs the average over the y terms in the cross sections. For the CHARM experiment, $c = 0.375$, and this value was used for the present experiment.

BB. Left-right symmetric models.

This model uses a charged current Lagrangian of the form

$$\ell^{cc} = -\frac{g}{2\sqrt{2}}[W_L^\dagger(J_\ell^V - J_\ell^A) + W_R^\dagger(J_\ell^V + J_\ell^A)] + \mathrm{h.c.} \qquad (B.7)$$

where W_L and W_R are charged left- and right-handed spin-1 gauge boson fields and the leptonic currents are $J^V_{\ell,\kappa} = \bar{\ell}\gamma_\kappa\nu_\ell$ and $J^A_{\ell,\kappa} = \bar{\ell}\gamma_\kappa\gamma_5\nu_\ell$. The

gauge particles will form eigenstates W_1 and W_2 with a mixing angle ω

$$\begin{pmatrix} W_1 \\ W_2 \end{pmatrix} = \begin{pmatrix} \cos\omega & -\sin\omega \\ \sin\omega & \cos\omega \end{pmatrix} \begin{pmatrix} W_L \\ W_R \end{pmatrix} \tag{B.8}$$

We now define

$$\epsilon = \frac{1+\tan\omega}{1-\tan\omega} \qquad r = \frac{m_{W_1}^2}{m_{W_2}^2}$$
$$\eta_{AA} = \frac{r+\epsilon^2}{1+r\epsilon^2} \qquad \eta_{AV} = \frac{(r-1)\epsilon}{1+r\epsilon^2}$$

$$\sqrt{\tfrac{1}{2}}G_{LR} = \frac{g^2}{8}\left[\left(\frac{\sin\omega-\cos\omega}{m_{W_1}}\right)^2 + \left(\frac{\sin\omega+\cos\omega}{m_{W_2}}\right)^2\right] \tag{B.9}$$

The differential cross section for inverse muon decay is then

$$\begin{aligned}\frac{d\sigma}{dy} =& \frac{G_{LR}^2}{16\pi}s\left[(1+\eta_{AA}^2)\left(2-2y+y^2-\frac{m_\mu^2}{s}(2-y)\right)\right. \\ &+ 2\eta_{AA}\left(2y-y^2-\frac{m_\mu^2}{s}y\right) \\ &\left.+ 4\left(\eta_{AV}^2 + P_{\nu_\mu}\eta_{AV}(1+\eta_{AA})\right)\left(1-\frac{m_\mu^2}{s}\right)\right]\end{aligned} \tag{B.10}$$

and the normalized integrated cross section is

$$S = \tfrac{1}{4}\frac{(1+\eta_{AA})^2 + 4\eta_{AV}^2 + 4P_{\nu_\mu}\eta_{AV}(1+\eta_{AA}) + c(1-\eta_{AA})^2}{1+\eta_{AA}^2+2\eta_{AV}^2}. \tag{B.11}$$

This depends on the parameters $m(W_1)/m(W_2)$ and ω through the parameters η_{AA} and η_{AV}.

BC. Models with more arbitrary couplings.

Reference 2 quotes the formula for the normalized, integrated cross section for inverse muon decay

$$\begin{aligned}S =& \frac{1}{2A}\Big\{(1+c-2c')\left[|G_S|^2+|G_S'|^2+|G_P|^2+|G_P'|^2\right. \\ &\left.- 2P\Re(G_S G_S'^* + G_P G_P'^*)\right]\end{aligned}$$

$$
\begin{aligned}
&+ 2(1+c+2c')\left[|G_T|^2 + |G'_T|^2 - 2P\Re(G_T G'^{*}_T)\right] \\
&- 2(1-c)\left[\Re(G_S G^{*}_T + G'_S G'^{*}_T - G_P G^{*}_T - G'_P G'^{*}_T)\right. \\
&\left. - P\Re(G_S G'^{*}_T + G'_S G^{*}_T - G_P G'^{*}_T - G'_P G^{*}_T)\right] \\
&+ 2(1+c)\left[|G_V|^2 + |G'_V|^2 + |G_A|^2 + |G'_A|^2\right. \\
&\left. + 2P\Re(G_V G'^{*}_V + G_A G'^{*}_A)\right] \\
&+ 4(1-c)\left[\Re(G_V G^{*}_A + G'_V G'^{*}_A)\right. \\
&\left. + P\Re(G_V G'^{*}_A + G_A G'^{*}_V)\right]\Big\} \qquad (B.12)
\end{aligned}
$$

where c is the constant from averaging over the y distribution (= 0.375 for CHARM), c' is another constant of unspecified origin (= 0.5 for CHARM), P is the neutrino handedness, and the various complex coefficients G_i are coupling constants. The V−A limit is obtained when $G_V = G_A = 1$, $G'_V = G'_A = -1$, and all other G_i constants are 0. The dimensionless parameter A is related to the muon lifetime τ_μ as follows:

$$
A = \frac{3072\pi^3\tau_\mu}{m_\mu^5 G_0^2}\left[1 + \frac{e^2}{8\pi^2}\left(\frac{25}{4} - \pi^2\right)\right]^{-1}\left[1 + 4\eta\frac{m_e}{m_\mu} - 8\frac{m_e^4}{m_\mu^2}\right]^{-1} \qquad (B.13)
$$

and is equal to 16 in the V−A case.

Owing to the lack of details on the derivation in reference 2, we shall not, in this thesis, attempt to reproduce the limits on the S, P, and T couplings with our results on the inverse muon decay. It would be beyond the scope of this work to derive a formula for the differential cross section $\frac{d\sigma}{dy}$ in the most general case. This is what would be required to exploit properly the ability to measure the y dependence of this reaction using a narrow-band neutrino beam.

APPENDIX C: CHARGE DIVISION READOUT OF THE TOROID PROPORTIONAL CHAMBERS

In this appendix we shall describe the scheme which allowed us to determine which among 4470 wires were hit in a given event, using only 720 amplifier channels.

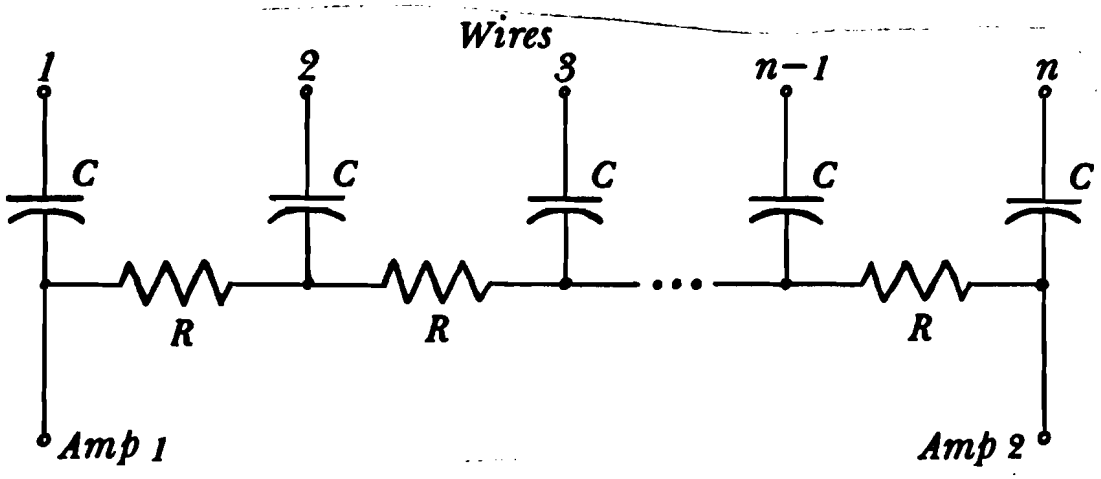

Figure C–1. Charge division network.

In charge division, a group of adjacent wires are connected in parallel using a resistive-capacitive network. (See figure C–1.) For two of the double 24′ planes the wires were read out in groups of sixteen, using 68Ω resistors, with an amplifier on each end. The other planes were read out in groups of eight, with 100Ω resistors. If we approximate these by the continuous case, as a transmission line with constant resistance, inductance, and capacitance per unit length, we obtain the telegrapher's equation.[1] Solving this equation,

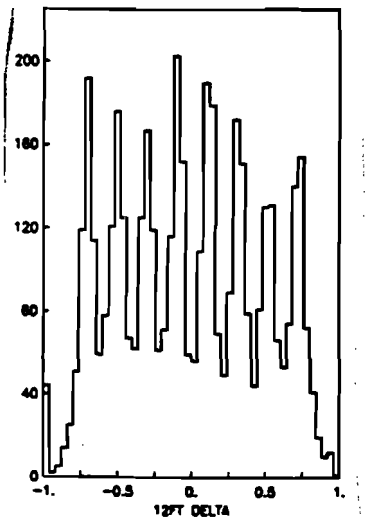

Figure C–2. Δ plot.

we find that a charge deposited at point x along the transmission line of length l would be divided between the two ends as follows:

$$\Delta = \frac{Q_0 - Q_1}{Q_0 + Q_1} = \frac{l - 2x}{l} \qquad (C.1)$$

where Q_0 and Q_1 are the charges measured at $x = 0$ and at $x = l$. The simple linear relation between Δ and the position of the charge deposited carries over in the discrete case. Figure C–2 plots Δ for all of the 12′ chambers in about four thousand neutrino and antineutrino triggers. The peaks here correspond to the wire positions (eight, in this case) and are fairly well separated.

The amplifiers were substantially similar to those in the calorimeter. The charge collection time for the sample and hold circuit was increased to insure that all of the charge deposited by a track would be sampled independent of the amount of drift time.

The main limitation of the charge division system was its inability to deal with multiple hits within a group of wires. Information on the total amount of charge received at the amplifiers was not enough to reconstruct the

hit locations, and the resolution was degraded. Multiple hits may have come from delta-ray production in the toroid magnets, accidental coincidences with cosmic rays or noise, or from multiple muons. On the whole, however, the toroid spectrometer chambers were able to give sufficiently good momentum resolution at moderate muon energies for the purposes of this thesis.

LIST OF REFERENCES—Chapter 1.

1. W. Pauli, *Proc. Solvay Congr.* (1933), 324.

2. E. Fermi, *Zeit. Phys.* 88 (1934), 161.

3. T. D. Lee and C. N. Yang, "Question of Parity Nonconservation in Weak Interactions," *Phys. Rev.* 104 (1956), 254.

4. C. S. Wu *et al.*, "Experimental Test of Parity Conservation in Beta Decay," *Phys. Rev.* 105 (1957), 1413–1415.

LIST OF REFERENCES—Chapter 2

1. E. Commins, P. H. Bucksbaum, **Weak Interactions of Leptons and Quarks**, Cambridge: Cambridge University Press, 1983, p. 10.

2. H. Frauenfelder *et al.*, *Phys. Rev.* **107** (1957), 643.
P. Cavenagh *et al.*, *Phil. Mag.* **41** (1950), 701.
A. de Shalit *et al.*, *Phys. Rev.* **170** (1968), 1200.

3. M. Goldhaber *et al.*, *Phys. Rev.* **109** (1958), 1015.

4. R. P. Feynman, M. Gell-Mann, *Phys. Rev.* **109** (1958), 193.
R. Marshak, E. Sudarshan, *Phys. Rev.* **109** (1958), 1960.

5. F. Bergsma *et al.*, "Experimental Study of the Reaction $\nu_\mu e^- \rightarrow \mu^- \nu_e$," *Phys. Lett.* **122B**, (1983) 465–470.
Commins and Bucksbaum, *op. cit.* , p. 128.

6. L. Wolfenstein, "Lepton Number Violation and Neutrino Mass," Carnegie-Mellon University preprint CMU–HEP84–84.

7. M. L. Goldhaber *et al.*, *Phys. Rev.* **109** (1958), 1015.

8. G. L. Kane, "Generalized Higgs physics and technicolor," *Les Houches Session XXXVII, 1981, Gauge Theories in High Energy Physics, Part I* ed. Mary K. Gaillard and Raymond Stora, Amsterdam: North-Holland, 1983, pp. 415-440.

9. K. Mursula *et al.*, "The Lorentz Structure of Leptonic Charged Weak Interactions,"*Nucl. Phys.* **B219** (1983), 321–340.

10. J. Lovseth, "On the Angular Distribution of the Brookhaven 1962 Neutrino Experiment," *Phys. Lett.* **5** (1963), 99–201.

11. T. Kitagaki *et al.*, "High-energy quasielastic $\nu_\mu n \rightarrow \mu^- p$ scattering in deuterium," *Phys. Rev. D28* (1983) 436–442.

12. Y.-P. Yao, "Nuclear Effects on the Quasi-Elastic Neutrino Scattering $\nu + n \rightarrow \mu^- + p$," *Phys. Rev.* **176** (1968), 1680–1685.
J. S. Bell, C. H. Llewellyn Smith, "Quasielastic Neutrino-Nucleus Interactions," *Nucl. Phys.* **B28** (1971), 317–340.
S. K. Singh, "The Effect of Final State Interactions and Deuteron Binding in $\nu + d \rightarrow \mu^- pp$,"*Nucl. Phys.* **B36** (1972), 419–435.
C. H. Llewellyn Smith, "Neutrino reactions at accelerator energies," *Phys. Rep.* **3** (1972), 310–313.

13. B. Goulard, H. Primakoff, "Nuclear Structure Effects in 'Elastic' Neutrino-induced Reactions," *Phys. Rev.* **135** (1964) B1147.

14. D. H. Perkins, "Review of Neutrino Experiments," *Proc. 1975 Intl. Symp. on Lepton and Photon Interactions at High Energies*, Stanford: (1975), 575.

15. R. T. Ross, "A Study of the Reaction $\nu p \rightarrow \mu^- \pi^+ p$," *Neutrinos-78*, ed. E. C. Fowler, Purdue University, (1978), 929-938.

LIST OF REFERENCES–Chapter 3

1. N. Armenise *et al.*, "Experimental Study of the Reaction $\nu_\mu + e^- \rightarrow \mu^- + \nu_e$," *Phys. Lett.* **84B** (1979), 137–142.

2. M. Jonker *et al.*, "Experimental Study of Inverse Muon Decay," *Phys. Lett.* **93B** (1980), 203–209.

3. F. Bergsma *et al.*, "Experimental Study of the Reaction $\nu_\mu e^- \rightarrow \mu^- \nu_e$," *Phys. Lett.* **122B** (1983), 465–470.

4. A. N. Diddens *et al.*, "A Detector for Neutral-Current Interactions of High-Energy Neutrinos," *Nucl. Instr. and Meth.* **178** (1980) 27–48.
C. Bosio *et al.*, "Proportional Drift Tubes for Large Calorimeter Detectors," *Nucl. Instr. and Meth.* **157** (1978), 35–46.

5. J. Maalampi *et al.*,"Study of the V, A Structure of the Charged Leptonic Current," *Nucl. Phys. B***207** (1982), 233–250.

6. K. Mursula *et al.*,"The Lorentz Structure of Leptonic Charged Weak Interactions," *Nucl. Phys. B***219** (1983), 321–340.

7. K. Enqvist *et al.*, "Mirror Leptons," *Nucl. Phys. B***226**, (1983), 121–151.

8. E. Di Capua *et al.*,"Study of the Decay $\pi \rightarrow e + \nu$," *Phys. Rev.* **133** (1964), B1333–B1340.
D. Bryman, C. Picciotto, "Revised value for the $\pi \rightarrow e\nu$ branching ratio,"*Phys. Rev. D***11** (1975), 1337.

9. K. S. Heard *et al.*,"A Measurement of the $(K^+ \rightarrow e^+\nu)/(K^+ \rightarrow \mu^+\nu)$ Branching Ratio," *Phys. Lett.* **55B** (1975), 327–330.
J. Heintze *et al.*,"A New Measurement of the $(K^+ \rightarrow e^+\nu)/(K^+ \rightarrow \mu^+\nu)$ Branching Ratio," *Phys. Lett.* **60B**,302–304.

10. R. Abela *et al.*, "Measurements fo the polarization of the $2p$ and $1s$ states in muonic atoms and helicity of the muon in pion decay," *Nucl. Phys. A* **395** (1983), 413–434.

11. F. W. J. Koks, J. van Klinken, "Investigation on β-Polarization at Low Velocities with β-Particles from the Decay of Tritium," *Nucl. Phys. A***272** (1976), 61–81.

12. M. A. B. Bég *et al.*, "Manifest Left-Right Symmetry and its Experimental Consequences," *Phys. Rev. Lett.* **38** (1977), 1252–1255.

13. S. Derenzo, "Measurement of the Low-Energy End of the μ^+ Decay Spectrum," *Phys. Rev.* **181** (1969), 1854–1866.

14. V. V. Akhmanov *et al.*, "Asymmetry of Positrons from the Decay $\pi^+ \rightarrow \mu^+ \rightarrow e^+$ in the Longitudinal 140 000 Oe Magnetic Field," *Sov. Jour. Nucl. Phys.* **6** (1968), 230–238.

15. F. Corriveau *et al.*, "Measurement of the positron longitudinal polarization in muon decay," *Phys. Rev. D***24** (1981), 2004–2007.

16. F. Niebergall, *Proc. Int. Conf. Neutrino '82*, vol. 2, (Budapest, 1982), 62.

17. W. Bartel *et al.*, "Observation of a Charge Asymmetry in $e^+e^- \rightarrow \mu^+\mu^-$," *Phys. Lett. B***108** (1982), 140–144.

18. A. Argento *et al.*, "Electroweak Asymmetry in Deep Inelastic Muon Nucleon Scattering," *Phys. Lett.* **120B** (1983), 245–250.
J. D. Bjorken, "Model-independent remarks on electron-quark parity-violating neutral current couplings," *Phys. Rev. D***18** (1976), 3239–3243.

19. J. Carr *et al.*, "Search for Right-Handed Currents in Muon Decay," *Phys. Rev. Lett.* **51**, (1983), 627–630.
K. Mursula, "Leptonic Charged Weak Interactions in the Left-Right Symmetric Model," *Nucl. Phys. B***241**, (1984), 173-188.

20. D. P. Stoker *et al.*, "Search for Right-Handed Currents by Means of Muon Spin Rotation," *Phys. Rev. Lett.* **54**, (1985), 1887–1890.

LIST OF REFERENCES–Chapter 4

1. F. E. Taylor *et al.*, "The Construction and Performance of Large Flash Chambers," *IEEE Transactions on Nucl. Sci.* , **NS–27** (1980), 30–37.

D. Bogert *et al.*, "The Operation of a Large Flash Chamber Neutrino Detector at Fermilab," *IEEE Transactions on Nucl. Sci.* , **NS–29** (1982), 363–367.

2. F. Sauli, "Principles of Operation of Multiwire Proportional and Drift Chambers," CERN report 77-09 (1977).

J. A. Jaros, "Drift and Proportional Tracking Chambers," SLAC-PUB-2647, (1980).

3. J. Bofill *et al.*, "The Application of Resistive Charge Division in Large Proportional Tube Chambers," *IEEE Transactions on Nucl. Sci.* , **NS–29**, (1982), 400–401.

4. Particle Data Group, "Review of Particle Properties," *Phys. Lett.* **111B**, (1982).

5. A. Mukherjee, "Shower Monte Carlo Versus Calibration," E594 internal memo 84–25, (1984).

6. R. Verdier, J. S. Whitaker, "Muon Tracking Package for E594 Offline Analysis, Version 3" E594 internal memo 83–3, (1983).

7. J. Bofill, "Upper Limit for ν_μ Oscillation into ν_τ in a Dichromatic Beam," Ph.D. thesis, Massachusetts Institute of Technology, (unpublished), (1984), p. 56.

8. *Ibid.*, p. 34.

LIST OF REFERENCES–Chapter 5

1. J. Maalampi, *et al.*, "Study of the V, A Structure of the Charged Leptonic Current," **Nucl. Phys. B** *207* (1982), 233–250.

2. T. Eldridge, private communication.

3. W. T. Eadie *et al.*, **Statistical Methods in Experimental Physics**, (London: North-Holland, 1971), 257–262.

4. J. Bofill, Ph.D. thesis, Massachusetts Institute of Technology, 1984, (unpublished).

5. J. Orear, "Notes on Statistics for Physicists, Revised," Cornell University preprint CLNS 82/511, July 1982.

6. F. Bergsma *et al.*, "Experimental Study of the Reaction $\nu_\mu e^- \rightarrow \mu^- \nu_e$," *Phys. Lett.* **122B** (1983), 465–470.

7. R. Pitt, "Current State of E-594 Narrow Band Flux Analysis," E594 internal memo 84–24, (1984).

8. F. E. Taylor, "The Weight of the Calorimeter," E594 internal memo 83–8 (1983).

LIST OF REFERENCES–Chapter 6

1. N. Armenise *et al.*, "Experimental Study of the Reaction $\nu_\mu + e^- \rightarrow \mu^- + \nu_e$," *Phys. Lett.* **84B** (1979), 137–142.

2. M. Jonker *et al.*, "Experimental Study of Inverse Muon Decay," *Phys. Lett.* **93B** (1980), 203–209.

F. Bergsma *et al.*, "Experimental Study of the Reaction $\nu_\mu e^- \rightarrow \mu^- \nu_e$," *Phys. Lett.* **122B** (1983), 465–470.

3. J. Maalampi *et al.*,"Study of the V, A Structure of the Charged Leptonic Current," *Nucl. Phys.* **B207** (1982), 233–250.

4. K. Mursula *et al.*,"The Lorentz Structure of Leptonic Charged Weak Interactions," *Nucl. Phys.* **B219** (1983), 321–340.

LIST OF REFERENCES–Appendix A

1. C. Jarlskog, "Tests of the V−A Theory in Neutrino-Lepton Interactions," *Lett. al Nuov. Cim.* **6**, (1970), 377-380.

2. N. Armenise *et al.*, "Experimental Study of the Reaction $\nu_\mu + e^- \rightarrow \mu^- + \nu_e$," *Phys. Lett.* **84B**, (1979), 137–142.

3. F. Bergsma *et al.*, "Experimental Study of the Reaction $\nu_\mu + e^- \rightarrow \mu^- + \nu_e$," *Phys. Lett.* **122B**, (1983), 465–470.

4. F. Scheck, **Leptons, Hadrons, and Nuclei**. Amsterdam: North-Holland, 1983.

5. E. D. Commins, P. H. Bucksbaum, **Weak Interactions of Leptons and Quarks**, Cambridge: Cambridge University Press, 1983, p. 95.

LIST OF REFERENCES–Appendix B

1. J. Maalampi *et al.*,"Study of the V, A Structure of the Charged Leptonic Current," *Nucl. Phys.* **B207** (1982), 233–250.

2. K. Mursula *et al.*,"The Lorentz Structure of Leptonic Charged Weak Interactions," *Nucl. Phys.* **B219** (1983), 321–340.

LIST OF REFERENCES–Appendix C

1. M. G. Forrester, B.S. thesis, Massachusetts Institute of Technology, June 1981 (unpublished).

J. L. Alberi, V. Radeka, "Position Sensing by Charge Division," *IEEE Trans. on Nucl. Sci.*, Vol. NS-23, 1976.

V. Radeka, P. Rehak, "Charge Dividing Mechanism on Resistive Electrode in Position-sensitive Detectors," *IEEE Trans. on Nucl. Sci.*, Vol. NS-26, 1979.

ACKNOWLEGMENTS

I would like to take this opportunity to thank the many individuals who made my work possible. To the senior members of the Counter Spark Chamber Group at MIT I owe a great deal more than just my livelihood these last five years; if I have learned anything about how to run a large scale experiment, I have learned it from Wit Busza, Larry Rosenson, Lou Osborne, Scott Whittaker, Jerry Friedman, and, especially, from my adviser, Henry Kendall. I extend to them my gratitude. A list of credits would be incomplete without mention of the special contributions, technical and non-technical, of the redoubtable Tommy Lyons. Without his ideas, this experiment would have been somewhat impoverished.

Day in and day out, my fellow graduate students provided both the best possible way to learn physics (and a lot besides physics, I should add) and a great bunch of friends in a living and working situation that only those who have experienced it can know about. I would like to list all the ways they contributed to the experiment and to me personally, but I do not have the space here. Many thanks to Juan Bofill, Andy Cohen, Terry Eldridge, Tom Mattison, Aseet Mukherjee, Mike Tartaglia, John Slate, and Gong Ping Yeh.

I would like to thank the other members of the E594 experiment for their assistance and hard work: from Michigan State University, Maris Abolins, Dan Owens, Chip Brock, and Harry Weerts; from Fermilab, Linda Stutte, Dixon Bogert, Jorge Morfín, and Jimmy Walker; and from MIT, Robin Verdier, Stu Fuess, Maury Goodman, and Randy Pitt. In particular, I greatly appreciate the encouragement and advice from Frank Taylor relating to this thesis. To the staffs of the Users' and Housing Offices at Fermilab and of the Laboratory of Nuclear Science at MIT, many thanks. I am deeply indebted to the super administrative assistants who kept things running at MIT, Sally Anand and Sandy Spry, for service in ways too numerous to list.

Without the support of my extended family I would never have been able to complete this work. My steadfast friends at the Tech Catholic Community

taught me by example how even a big university can excel in humanity; to Christian, Luz, Mary Jean, Sue, and to so many others, I give my heartfelt thanks. The parish of St. John Neumann in St. Charles was a lifeline for me, as well as an inspiration. Through all the trials of my graduate career, my pastors, Bob Moran, Dan Hermes, and Bob O'Donnell have led me safely and I give them my thanks. I am deeply grateful to Virginia S. Finn for the many ways she has been present to me, as friend, counselor, and family. To my own family I owe the greatest debt of thanks: to my mother, Mariquita, to my father, Carlos, for always encouraging me in whatever vocation I should choose, to my sister, Cheryl, for her constant concern and thoughtfullness, and, most of all, to my bride-to-be, Pam, for giving of herself in every way, I give my love and gratitude.